Experimental Investigation of Pixelated Semiconductor Photodetectors with CdTe Sensor Material for the Search for the Neutrinoless Double Beta Decay

Master Thesis

for the attainment of the academic degree
Master of Science (M. Sc.)

performed at
the Erlangen Centre for Astroparticle Physics
Friedrich-Alexander-University Erlangen-Nuremberg
under the supervision of Dr. Thilo Michel & Prof. Dr. Gisela Anton

ERLANGEN CENTRE
FOR ASTROPARTICLE
PHYSICS

submitted by

Mykhaylo Filipenko

November 2011

Universität Regensburg

Friedrich-Alexander-Universität
Erlangen-Nürnberg

Contents

I Introduction 1

II Motivation and Theoretical Background 3
II.1 About the neutrinoless double beta decay . . . 4
II.2 Consequences for theoretical physics . . . 9
II.2.1 Neutrino mass and mass hierarchy . . . 9
II.2.2 Majorana particles and physics beyond the standard model . . . 9
II.3 The experimental methods . . . 12
II.3.1 The energy spectrum of the decay electrons in the double beta decay 12
II.3.2 Tracking . . . 14
II.4 The Timepix detector . . . 17
II.4.1 The structure and functionality of the Timepix detector . . . 18
II.4.2 The time-over-threshold mode . . . 20
II.4.3 Some important expressions concerning the Timepix . . . 22

III Calibration Procedure and Energy Resolution for Single Hits 25
III.1 Threshold equalization . . . 27
III.2 THL calibration . . . 29
III.3 TOT calibration . . . 36
III.3.1 Global calibration . . . 36
III.3.2 Pixel-by-pixel calibration . . . 49
III.3.3 Calibration curve reliability . . . 57
III.4 Energy resolution for single pixel hits . . . 61
III.4.1 Differences between global and pixel-by-pixel calibration . . . 63
III.4.2 Dependence of the energy resolution on working parameters . . . 65
III.5 Summary . . . 71

IV Background Identification and Energy Resolution for Tracks 73
IV.1 Clustering, α-particle and muon identification . . . 75
IV.1.1 Identification of α-particles . . . 77
IV.1.2 Identification of muons . . . 79
IV.2 Discrimination of one and two electron tracks . . . 82
IV.2.1 Artificial neural networks . . . 84
IV.2.2 The pair production experiment . . . 86
IV.3 Energy resolution for tracks . . . 101
IV.3.1 The energy resolution for tracks at 661.5 keV . . . 101

IV.3.2 The energy resolution for pair production events at 1588.53 keV . 101
IV.4 Summary 104

V Conclusions and Outlook 107

A Spectra and Tables 111

B Software and Code 121

List of Figures 133

List of Tables 139

Bibliography 141

Acknowledgments 145

I Introduction

The measurement of neutrino mass constraints, the question whether the neutrino is its own anti-particle and the search for physics beyond the standard model - all these fundamental issues of modern physics are related to one very challenging experiment: The search for the neutrinoless double beta decay. This very rare process goes back to the last publication by the Italian physicist Ettore Majorana in 1937 [1]: He introduced his own mathematical method to describe neutrinos. Later in the early 40s, physicists discovered that his point of view would imply various, interesting consequences for the fundamental properties of elementary particles - of course only if it is true.

Therefore it quickly raised the question: How to find experimental evidence for Majorana's theory? Fortunately, it was possible to find a process which can only be predicted by Majorana's theory; however, not within the framework of regular Quantum Electro Dynamics. Hence, this process is of particular interest as it can be used to distinguish exactly, whether Majorana's ideas are realized in nature or not. This process is, as you can certainly imagine, the neutrinoless double beta decay and since it was predicted in 1941 lots of efforts were made to find it.

Nevertheless it has remained an uncompleted task until now. Although it is a well-defined physical process that has to be observed, the experimentalist has to face many difficulties: Very low event rates, the necessity of very good energy resolution for the measurement and the high background (in relation to the event rate) were and are some of the main reasons, which render this aim hardly possible. Thus, a lot of different experiments, or rather, experimental techniques are in development to solve these problems and unveil the truth about the nature of the neutrino.

The experimental approach discussed in this work is the usage of Timepix detector systems. The Timepix is a semiconductor X-ray imaging detector which can produce not only the images of an incoming intensity distribution or passing particles but measure their energy at the same time as well. The imaging property can be used to remove undesirable background events and the calorimetric property to detect the particular energy signature of the neutrinoless double beta decay; but this is to be discussed detailed in the first chapter.

Before such detectors can be used in a large scale experiment their intrinsic properties, imaging quality and energy resolution must be understood. This work covers these three points: First of all, we studied the energy-calibration of the detector in detail since due to the complex functionality of the detector it is a non-trivial process. This is discussed in

chapter III. Secondly, we investigated the energy-resolution quality of the detector with various detector settings. At last, we applied artificial neural networks and other pattern recognizing techniques to distinguish between the characteristic pattern of different sort of background; which is presented in chapter IV.

A little note on this work: If you are new to the topic of the neutrinoless double beta decay and Timepix detector systems, it is useful to read the first chapter and the technical details on the measurement process and experimental setups but if you are familiar with these things, feel free to skip the motivation chapter and the "technical" parts of the sections. The important data and the quantitative results will usually be provided in figures and tables. (Check out the list of figures and tables at the end to find the desired details on the experiments and results quickly.)

II Motivation and Theoretical Background

Contents

II.1 About the neutrinoless double beta decay 4
II.2 Consequences for theoretical physics 9
II.2.1 Neutrino mass and mass hierarchy 9
II.2.2 Majorana particles and physics beyond the standard model 9
II.3 The experimental methods 12
II.3.1 The energy spectrum of the decay electrons in the double beta decay 12
II.3.2 Tracking 14
II.4 The Timepix detector 17
II.4.1 The structure and functionality of the Timepix detector 18
II.4.2 The time-over-threshold mode 20
II.4.3 Some important expressions concerning the Timepix 22

In this section the reader is given some basic background knowledge about the neutrinoless double beta decay. The first section gives an introduction to the nature of the decay itself, the second explains its importance in the global framework of particle physics and the third gives an insight to the experimental approach, on which this work is grounded. If you are only interested in the properties of the Timepix detector, which were investigated in the context of this thesis, feel free to skip this chapter and go forward to chapter III.

II.1 About the neutrinoless double beta decay

At first, let's have a look at a very well known decay process: The regular beta decay. A neutron transforms into a proton, an electron and an electron anti-neutrino:

$$n \rightarrow p + e^- + \bar{\nu}_e \tag{II.1}$$

or if the neutron is embedded into the nucleus with mass number A and proton number Z, which decays to the nucleus Y:

$${}^{A}_{Z}X \rightarrow {}^{A}_{Z+1}Y + e^- + \bar{\nu}_e \tag{II.2}$$

The energy diagram for elements, which can undergo this decay, has a structure as shown on figure II.1 (a). Here ${}^{3}_{1}$H (Tritium) is taken as an example. It decays to ${}^{3}_{2}$He with a Q-value of 19 keV (The Q-value of a process is the difference in energy between the initial and final state.) with a half-life of $T_{\frac{1}{2}} = 12.33$ a. The half-life $T_{\frac{1}{2}}$ of such processes is usually between several days and up to 10^6 years. It can be calculated in perturbation theory with Fermi's Golden Rule [2]

$$(T_{\frac{1}{2}})^{-1}_{1\nu} = \frac{2\pi}{\hbar} |H_{fi}|^2 G(E_f). \tag{II.3}$$

G(E_f) is the phase space volume of the final state and H_{fi} is the matrix element describing the dynamics of the transition between the initial and the final state (the

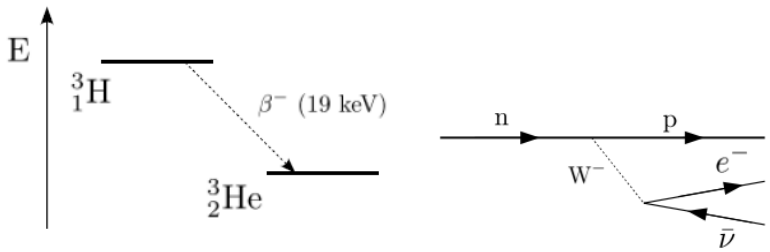

(a) Energy scheme **(b)** Feynmann-diagram

Figure II.1: The energy scheme (a) and the Feynmann-diagram (b) for the regular beta decay.

equilibrium states of ^{3}H and ^{3}He in our example)

$$H_{fi} = \langle f | \hat{H}_{weak} | i \rangle . \tag{II.4}$$

The form of the operator $\hat{H}_{weak}$ can be derived from the Lagrangian of the weak interaction (Glashow-Weinberg-Salam Lagrangian, see [3]). The coupling α of a particular interaction declines with the mass of its bosons. This is the reason why the decay rates of β-decays are much lower than the decay rates of electro-magnetic transitions ($\alpha_W \ll \alpha_{EM}$). Photons have no rest mass whereas W^+, W^- bosons have masses on the scale of 10 GeV. The transition probabilities are therefore much smaller.

The Feynmann diagram of the regular beta decay is illustrated on II.1 (b). We can add another W^- to the diagram in such a way as illustrated on figure II.2. Such processes are known as double beta decays. Decay rates for this process are even smaller since the number of vertices is increased to four[1].

On figure II.2 (a) the double beta decay (which will be called $2\nu\beta\beta$ in this work) is shown and on picture II.2 (b) the neutrinoless double beta decay (which will be referred to as $0\nu\beta\beta$). In both cases you start with two neutrons (or a nucleus containing at least two neutrons). For the $2\nu\beta\beta$ you get two protons, two electrons and two electron anti-neutrinos after the decay:

$$2n \rightarrow 2p + 2e^- + 2\bar{\nu_e} \tag{II.5}$$

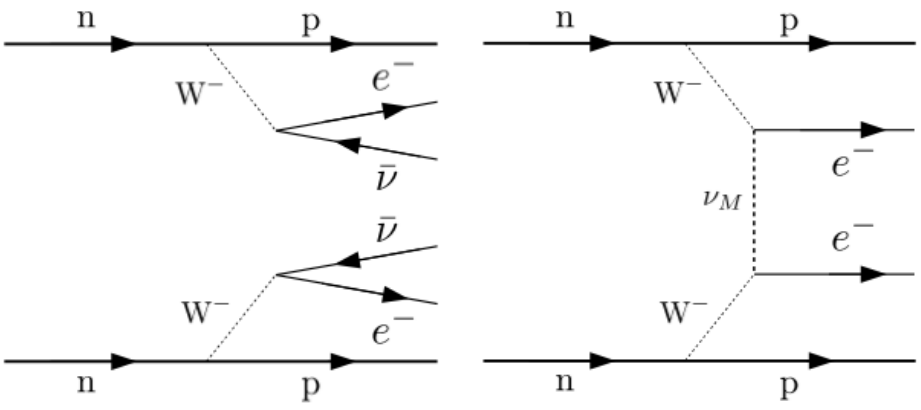

(a) $2\nu\beta\beta$ decay **(b)** $0\nu\beta\beta$ decay

Figure II.2: The Feynman diagram for the double beta decay - $2\nu\beta\beta$ (a) and the neutrinoless double beta decay - $0\nu\beta\beta$ (b).

1 For every vertex in the diagram the amplitude is suppressed by a factor of $\sqrt{\alpha}$.

but in the case of the $0\nu\beta\beta$ the process takes place without the two anti-neutrinos:

$$2n \rightarrow 2p + 2e^- \tag{II.6}$$

The $2\nu\beta\beta$ could already be observed in several experiments [4], the first time in 1987. The half-life for such processes is much higher than for the regular beta decay and is in the order of magnitude of $(T_{\frac{1}{2}})_{2\nu\beta\beta} \approx 10^{20} - 10^{21}$ a.

Now back to the $0\nu\beta\beta$: The anti-neutrino, which is created in the first part of the process, is absorbed as a neutrino by the second neutron. This can be understood descriptive like bringing the anti-neutrino from the right to the left side in formula II.1. The anti-neutrino now has "become" its anti-particle (this will be discussed in the next section):

$$\begin{aligned} n &\rightarrow p + e^- + \bar{\nu_e} \\ \Rightarrow n + \nu_e &\rightarrow p + e^- \end{aligned} \tag{II.7}$$

This process is called the neutrinoless double beta decay. The half-life for isotopes undergoing this decay can be calculated by the formula [5]

$$(T_{\frac{1}{2}})^{-1}_{0\nu\beta\beta} = G_{0\nu}(Q_{\beta\beta},Z) \left|M_{0\nu}\right|^2 \langle m_\nu \rangle^2 . \tag{II.8}$$

$G_{0\nu}$ is the phase space factor of the decay. It is one of the reasons why the half-life of the $0\nu\beta\beta$ is much larger compared to the half-life of the $2\nu\beta\beta$. There are much less possibilities to distribute the energy and the momentum between two particles than amoung four. The matrix elements $M_{0\nu}$ describes the transition dynamics of the nuclei states and can roughly be written as [6]

$$M_{fi} \propto \sum_s \frac{\langle i| \hat{T}_1 |s\rangle \langle s| \hat{T}_2 |f\rangle}{E_f - E_i}. \tag{II.9}$$

Here the sum is taken over all virtual intermediate states $|s\rangle$ (see figure II.3) and $\hat{T}_1$, $\hat{T}_2$ are the transition operators. In fact, calculating these quantities is a rather non-trivial task and is usually done by the QRPA, IBM or SM approach (see [6]). The term $\langle m_\nu \rangle$ in formula II.8 is the effective Majorana neutrino mass. Due to neutrino oscillation experiments we know that neutrinos propagate as a mixture of mass eigenstates but have to be considered as flavour eigenstates in weak interaction processes. The electron neutrino ν_e is a mixture of the three neutrino mass eigenstates ν_1, ν_2, ν_3 and therefore the

effective neutrino mass $\langle m_\nu \rangle$ [5] has to be used (instead of using the mass of the electron neutrino only) :

$$\langle m_\nu \rangle = \sum_i |U_{ei}|^2 \, m_i \tag{II.10}$$

U_{ei} are the entries of the mixing matrix and m_i the masses for the mass eigenstates ν_i. Details about neutrino oscillations and the effective mass can be found in [7].

Generally the half-life of nuclides, which are capable of this decay, is in more than 10^{25} a.[1] Therefore this process, if it exists, is really rare and have not been measured until now. If we want to observe this process, first we have to know which nuclides could theoretically be used for an experimental setup.

Let's consider an nucleus X with proton number Z and neutron number N at the energy level E_i. If the nucleus T (with proton number Z+1) and the nucleus Y (with proton number Z+2) have energies E_t and E_f such that the relations

$$\begin{aligned} E_t - E_i &> 0 \\ E_t - E_f &> 0 \\ E_i - E_f &> 0 \end{aligned} \tag{II.11}$$

(II.12)

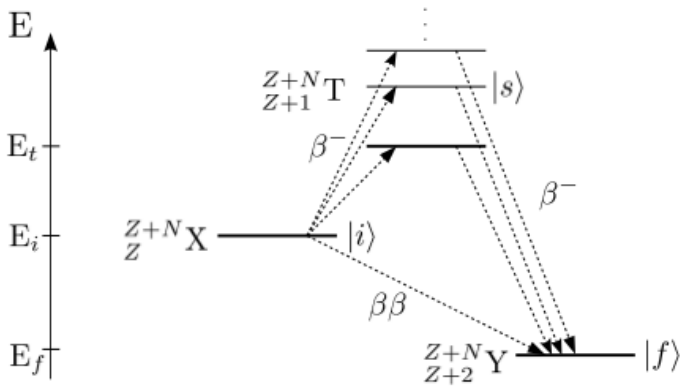

Figure II.3: The energy scheme for isotopes capable of the double beta decay.

1 This value is calculated with an effective neutrino mass of 0.3 eV. This value was set by Klapdor-Kleingrothaus [8] in 2006 who reported the observation of a $0\nu\beta\beta$ event with a 6σ significance. This result is highly debatable.

are satisfied, then nucleus X is capable of the double beta decay[1]. This scenario is drawn on figure II.3. So basically the single beta decay is energetically forbidden but the double beta decay is possible as a "tunneling process" through the virtual energy states $|s\rangle$[2]. This is another possible point of view to understand the reason for the high half-life of double beta decaying nuclides. The described condition is satisfied for 33 elements. Some of the most interesting isotopes for experiments are shown in table II.1.

Isotope	$Q_{\beta\beta}$ [keV]	$M_{0\nu}$	Natural Abundance [%]
^{76}Ge	2039	4.6	7.44
^{130}Te	2528	3.5	33.799
^{116}Cd	2814	2.7	7.49
^{136}Xe	2458	2.2	8.9
^{48}Ca	4272	0.6	0.187
^{100}Mo	3034	3.0	9.63
^{82}Se	2995	4.1	8.73
^{150}Nd	3367	3.1	5.64

Table II.1: A list of important isotopes capable of the double beta decay with some of a their properties. Values taken from [9], [10], [11] and [12].

1 Basically, every nuclide which can undergo the $0\nu\beta\beta$ can undergo the $2\nu\beta\beta$ with a much higher probability as well

2 Not only the ground state of the nuclide T but the exited states have to be taken into account as well.

II.2 Consequences for theoretical physics

Right now there exist about 20 different experiments trying to prove the existence of the neutrinoless double beta decay. But what is so interesting about this very rare process? Let us answer this question in this section.

II.2.1 Neutrino mass and mass hierarchy

The first reason to search for the $0\nu\beta\beta$ decay is, that one can extract the effective neutrino mass from it. If we remember the formula for the half-life II.8, we can calculate the effective neutrino mass $\langle m_\nu \rangle$ if we are able to determine the half-life in an experiment. The phase space volume $G_{0\nu}$ of the process can be computed from its kinematics and the matrix elements $M_{0\nu}$ for different nuclides can be computed by various theoretical approaches[6] with a relatively high precision.

With neutrino oscillation experiments like the DoubleChooz or the Kamiokande experiment (see [2]) one is only able to measure the differences in the squared mass of the three neutrino mass eigenstates (Δm^2_{12}, Δm^2_{13}, Δm^2_{23} with $\Delta m^2_{ij} = m^2_i - m^2_j$). They are in the order of magnitude of $10^{-3} - 10^{-5}$ eV^2. The knowledge of these differences does not fully define the neutrino mass scale and allows three possible so called "mass-hierarchies" . This is illustrate schematically on figure II.4. The following three different hierarchy scenarios could be realized in nature [7]:

- The normal hierarchy where one has $\Delta m^2_{31} > 0$ and $\Delta m^2_{21} > 0$.
- The inverted hierarchy with $\Delta m^2_{31} < 0$ and $\Delta m^2_{21} > 0$.
- The quasi-degenerate hierarchy with $m_1 \approx m_2 \approx m_3$.

The measurement of the effective neutrino mass would give an additional constraint to this problem and identify the hierarchy chosen by nature.

II.2.2 Majorana particles and physics beyond the standard model

If you remember equation II.6, maybe you already realized that the lepton number is not conserved in this equation and therefore the $0\nu\beta\beta$ decay is theoretically forbidden in the standard model. However, there are lots of model extensions to the standard model like SU(5), SO(10) gauge-group theories or theories involving super-symmetry (see [13]) that would allow a $0\nu\beta\beta$. The most promising approach is to describe neutrinos as massive Majorana-particles instead of massless Dirac-particles. The concept of Majorana-particles implies that the neutrino is its own anti-particle. This is necessary since the

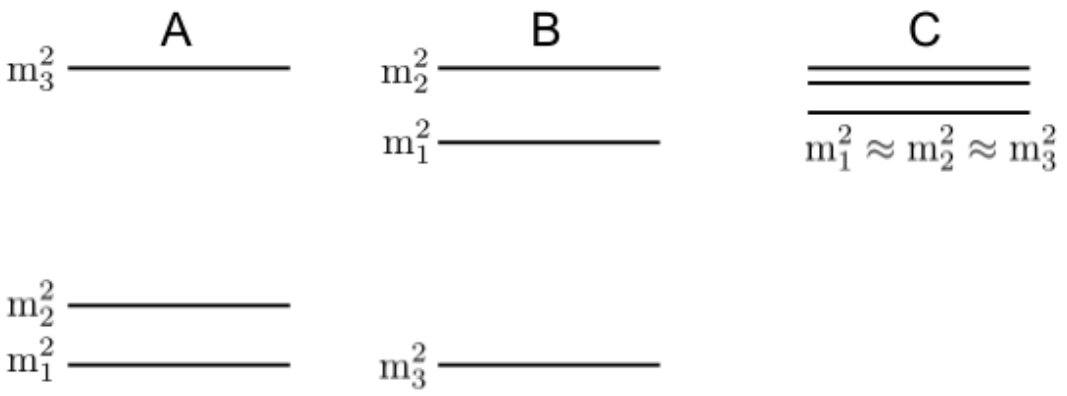

Figure II.4: The possible mass hierarchies for neutrinos: (A) normal hierarchy, (B) inverted hierarchy and (C) quasi-degenerate hierarchy.

weak interaction is parity violating. Only left-handed[1] neutrinos and right-handed anti-neutrinos can interact weakly (see [3]). If a massive anti-neutrino is emitted from the first neutron, it is right-handed and has to be

1. massive because then the helicity can be changed by a Lorentz-Transformation which cannot be done for massless particles as they move with the speed of light. If a particle propagates in the positive x direction with the speed v_1 you can pass it with a speed $v_2 > v_1$ (i.e. go to another inertial system of coordinates) and then the sign of the velocity and hence of the momentum and the helicity will be reversed in your system.
2. its own anti-particle since a neutrino is required at the second neutron for the process to occur.

These two properties are fulfilled only by a Majorana-neutrino but not by a Dirac-neutrino. Therefore an experimental proof of the $0\nu\beta\beta$ decay would confirm the concept of the Majorana-neutrino. A theorem proven by Schechter and Valle in 1982 [14] says that the statement $\nu = \bar{\nu}$ holds if the $0\nu\beta\beta$ is observed; no matter what kind of mechanism (super-symmtery, Majoron emission, etc.) is the reason from the $0\nu\beta\beta$ to occur.

Now, let's go back to the standard model extensions. The violation of the lepton number is not the only thing beyond the framework of the standard model that a $0\nu\beta\beta$ measurement could provide us - what more? Let's assume that the standard model is incomplete but we do not observe effect beyond because we perform our experiments on a very low energy scale only. The deviations from the standard model are negligible (or at least not measurable because we are limited by the precision of our measuring instruments) and become dominant only at very high energies. In this case it is reasonable to write the

1 Particles are called left-handed if their helicity is $h > 0$ and right-handed if $h < 0$. The helicity is defined as the sign of the projection of the spin $\vec{s}$ onto the momentum vector $\vec{p}$: $h = \frac{\vec{s}\cdot\vec{p}}{|\vec{p}||\vec{s}|}$

Lagrangian for the complete theory $\mathfrak{L}_{com}$ (standard model $\mathfrak{L}_{SM}$ and non standard model terms $\mathfrak{L}_i$) in an asymptotic series the following way:

$$\mathfrak{L}_{com} = \mathfrak{L}_{SM} + \frac{1}{\Lambda}\mathfrak{L}_5 + \frac{1}{\Lambda^2}\mathfrak{L}_6 + ... \tag{II.13}$$

Λ defines here the energy scale. The standard model Lagrangian $\mathfrak{L}_{SM}$ includes the electro-magnetic, the weak and the strong interaction. If the energy scale is really high, only the first term of the Lagrangian contributes (the standard model term) to the complete theory and the others are not of importance. From this starting point one can perform lots of transformations on the $\mathfrak{L}_5$ part of the Lagrangian and (for details see [13]) end up with the relation

$$\mathfrak{L}_5 = m_\nu \nu\nu + h.c. + .., \tag{II.14}$$

which shows that the Majorana mass term occurs as a part of the Lagrangian beyond the standard model. Thus the Majorana neutrino mass gives you direct insight to the order of magnitude of the first non-standard model term $\mathfrak{L}_5$.

II.3 The experimental methods

II.3.1 The energy spectrum of the decay electrons in the double beta decay

Ok, so now we know the problem and there is more than one good reason to solve it but how to do it? The main signature of the $0\nu\beta\beta$ is the sum energy distribution of the two out-coming electrons. Have a look at figure II.5. It shows a scheme of the theoretical calculations for this distribution. The sum energy of the two electrons relative to the Q-value is assigned to the x-axis. The y-axis is usually the number of events per kg, year and keV. The large blue part of the distribution is produced by the $2\nu\beta\beta$. It never reaches the Q-value because a part of the energy (at least the neutrino rest mass) is always transferred to the anti-neutrinos. The sharp red line belongs to the $0\nu\beta\beta$ and is positioned exactly at the Q-value because due to the absence of the anti-neutrinos the whole energy is distributed between the two electrons.

For this reason all of the experiments are aiming to measure the energy spectrum of double beta decay capable nuclides as precisely as possible. Although this has already been performed for the $2\nu\beta\beta$ and is in good agreement with the theory, at the same time the $2\nu\beta\beta$ events are a challenging background when you have to measure the $0\nu\beta\beta$ spectrum. In fact, the ratio between the red and the blue area is in the order of $\frac{1}{10^6}$, depending on $\langle m_\nu \rangle$; thus in average for every $0\nu\beta\beta$ event you get 10^6 of $2\nu\beta\beta$ background events which you cannot get rid off since every nucleus capable of performing the $0\nu\beta\beta$ is capable of performing the $2\nu\beta\beta$. During the last years lots of experiments have been

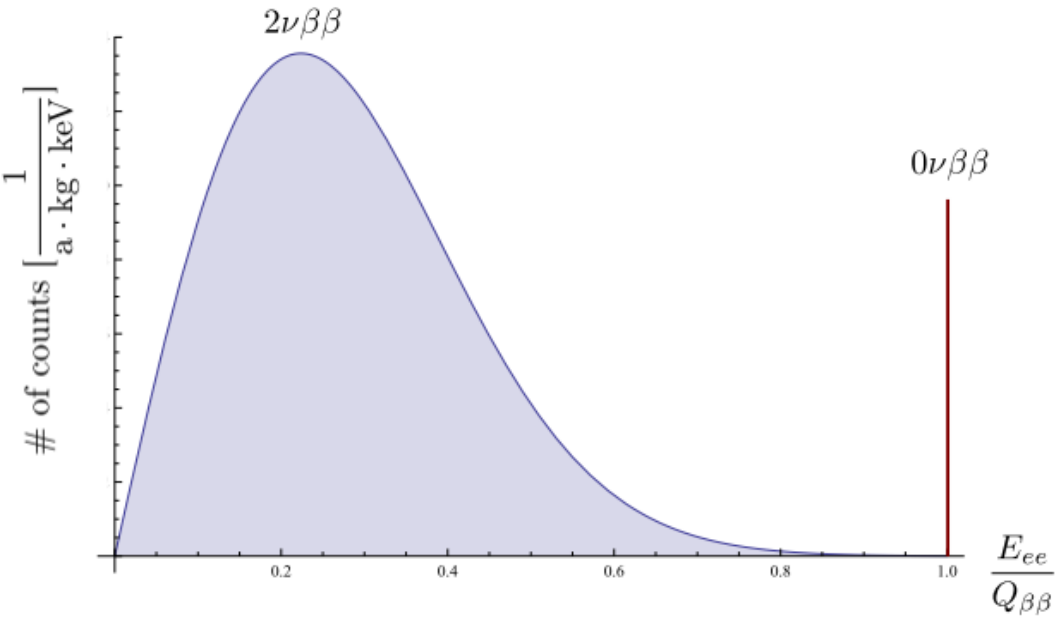

Figure II.5: A scheme of the sum energy distribution for the two electrons in the double beta decay. The blue area corresponds to the $2\nu\beta\beta$ and the red peak is the $0\nu\beta\beta$.

developed which are trying to measure the small peak at the Q-value - in simple terms: They try to built a highly precise calorimeter which measures the energy of the two electrons. In general every detector consists of the following parts:

- The decaying material is the part of the experimental setup to provide the decay we are actually searching for. For most setups the mass of this part is planned to be about 100 - 1000 kg of the enriched isotope.
- The sensor material is the part of the experimental setup to detect the decay and to provide the energy (or even the track) information.
- The electronics provide the readout to extract the signal out of the sensor material. The signal is usually electrical (charge is induced by the propagating particles), optical (scintillation light from excited atom states) or thermal (slight changes in temperature by thermal excitations caused by the propagating particles).
- A background veto is needed to reduce undesirable background from the outside to a minimal level. It can be active (recognition of undesirable events) or passive (absorption of undesirable events).

Some prominent experiments are GERDA with the isotope ^{76}Ge [15], NEXT [16] and EXO [11], which are gas detector experiments investigating ^{136}Xe and MOON [17] with the isotope ^{100}Mo. To compare such experiments we need to introduce several quantities:

- The energy resolution $\Delta E/E$ of the measurement apparatus at the region of interest: If you measure a monochromatic energy line at a particular energy (its distribution is $P(E) = \delta(E - E_0)$) the response of the calorimeter is in general a Gaussian distribution around this line due to various effects in the calorimeter:

$$P(E,E_0,\Delta E) = \frac{1}{\sqrt{2 \cdot \pi \cdot \Delta E}} \exp\left(\frac{(E - E_0)^2}{2(\Delta E)^2}\right) \tag{II.15}$$

  This process is called Gaussian broadening and it limits the quality of a measurement instrument. The narrower the distribution is, the better is the measurement device. The resolution of a measurement device is therefore defined as the width of this Gaussian (ΔE), divided by the energy E_0 of the line:

$$Res(E_0) = \frac{\Delta E}{E_0} \tag{II.16}$$

  Some of the effects are systematic, can be understood and eliminated (mostly just partially) to increase the resolution. Some effects are caused by random fluctuations in the device and are the natural limit for the resolution quality of the measurement device. The energy resolution of a detector is an important quantity because if the resolution is too bad two neighboured lines cannot be separated since they overlap.

- The specific background coefficient b [18]

$$b = \frac{\#\text{ of background events}}{keV \cdot kg \cdot a}, \tag{II.17}$$

  which provides the information how many background is expected in the region of interest (ROI) during a particular period of time with a particular mass of decaying material.

- The sensitivity to the half-life $(T_{\frac{1}{2}})_{0\nu\beta\beta}$ of the $0\nu\beta\beta$. This quantity tells us the limit of $(T_{\frac{1}{2}})_{0\nu\beta\beta}$ that can be achieved in experiment of mass M during a period of time t [19]:

$$(T_{\frac{1}{2}})_{0\nu\beta\beta} \propto \frac{a}{W n_\sigma}\sqrt{\frac{M \cdot t}{b \cdot \mathrm{Res(Q)}}}. \tag{II.18}$$

  a is the isotopic abundance and W is the molecular mass of the target material. n_Q is the number of standard deviations above background. b is the specific background coefficient and Res(Q) the resolution of the detector at the Q-value.

Table II.2 compares different experiments in their recent status. All of them are keen to achieve the best energy resolution and to reduce the background rate as much as possible.

II.3.2 Tracking

As the background reduction is the main problem for $0\nu\beta\beta$ experiments, it is reasonable to improve the methods for accomplishing this task. To do so the kinematic signature of the decay can be taken into account: When a particle propagates through the sensor material the scattering probability with the sensor material and the scattering angle depend on the energy, the charge and the mass of the particle. For instance muons pass the sensor

Experiment	**Isotope**	**Target mass** [kg]	**Res(Q)** [% FWHM]
GERDA	^{76}Ge	1000	0.16
CUORE	^{130}Te	200	0.25
CANDLES	^{48}Ca	300	3.4
EXO	^{136}Xe	1000	3.3
NEXT	^{136}Xe	100	1
COBRA	^{116}Cd	400	1.9
MOON	^{100}Mo	1000	6.8
DCBA	^{150}Nd	330	6

Table II.2: An overview about some recent $0\nu\beta\beta$ experiments. Information taken from [18].

material on very long, straight paths whereas electrons from beta decays produce shorter, curved tracks (figure II.6 (a) and (c), respectively).

The detection of such paths is called tracking. If we want to detect tracks within the sensor material, we have to divide the sensor material into pixels. There are different methods to perform this task which depend primary on the sort of sensor material you use - a gaseous, a liquid or a solid material. The pixelation procedure for the detector used in this work is described with more details in the next section.

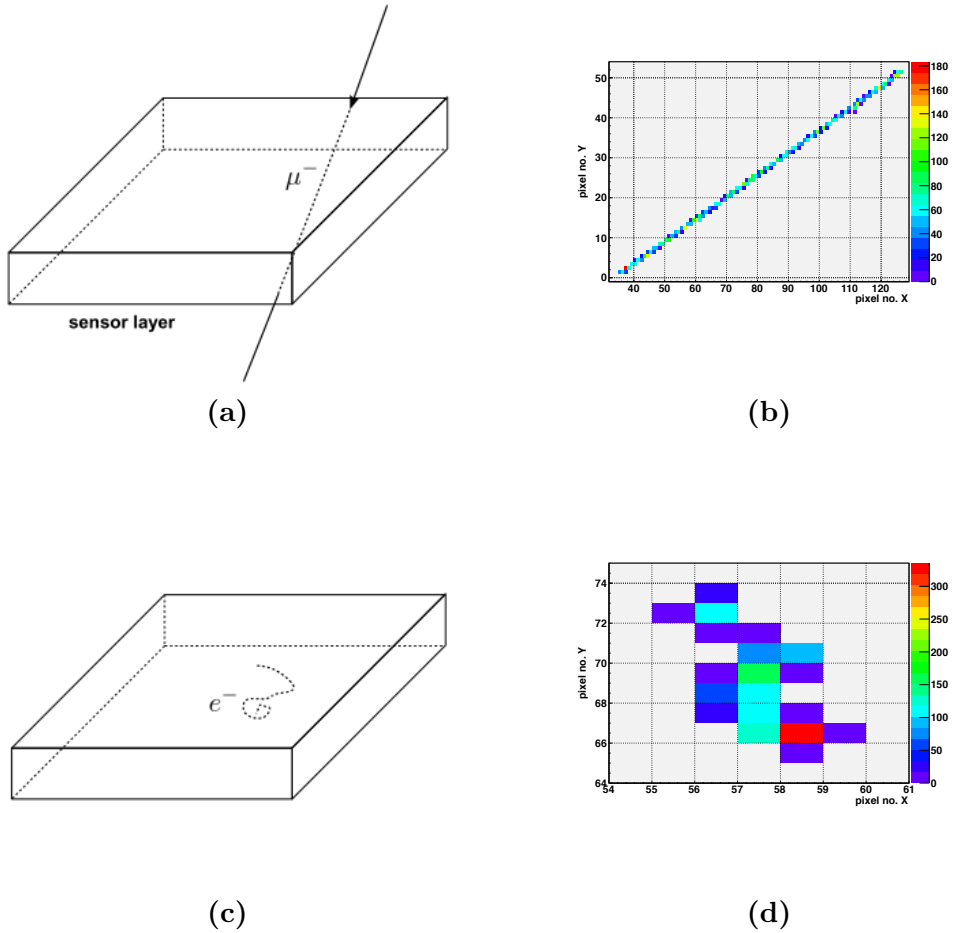

(a) **(b)**

(c) **(d)**

Figure II.6: On the left hand side: The scheme of a typical track for a muon (a) and an electron (c) through the sensor layer. On the right hand side: The same sort of track detected with a Timepix detector. The color of the pixels indicates the energy deposition in keV.

If a detector is pixelated, each of its pixels works as a small, elementary calorimeter detection cell. On its way through the sensor material a particle deposits a certain amount of its energy in each cell which is measured for each cell individually. The result of such a measurement is illustrated on figure II.6 for a muon (b) and an electron (d). The x- and y-axis are the discrete coordinates of the pixels and the color indicates the energy deposition in each pixel. The sum of the energy deposition in all pixels together provides the information for the energy a particle deposited within the detector on its way through (like in the pure calorimeter without pixels) but due to the tracking we also obtain the following additional information (compared to the pure calorimeter without pixels):

- A 2D projection of the particle track through the sensor material.
- The energy deposition per pixel of the track which depends highly on the sort of particle as well.

The reason why this information is really useful becomes clear if you take a look at figures II.6 and II.7. They illustrate the measurement of II.7 (a) an α-particle, II.7 (b) a simulated $0\nu\beta\beta$ event, II.6(b) a muon and II.6(d) an electron. Due to the propagation and the energy deposition pattern the different events can be distinguished very well. On the one hand this can be used to discriminate undesirable background events and on the other hand it gives you additional security on the $0\nu\beta\beta$ events you have measured. If you measure an event at the Q-value but its topological signature is in contradiction to the predictions (for instance evaluated by simulations), you can sort this event out. If the signature is in agreement with the predictions, the detected event is much more reliable.

The spatial resolution of the detector is given by its pixel pitch. The smallest pixel pitch available is limited by the technology of fabrication and miniaturization. The price you have to pay is a decline in energy resolution. Another disadvantage is the large number of channels which have to be calibrated and evaluated.

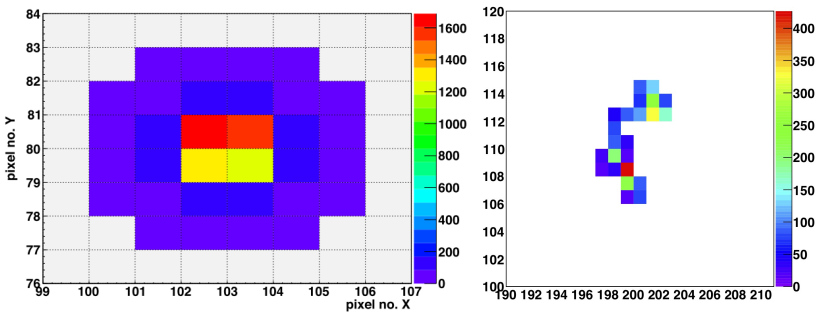

(a) α-particle **(b)** $0\nu\beta\beta$ event

Figure II.7: The response of a Timepix detector to an α-particle (a) and a simulated $0\nu\beta\beta$ event (b). The color of the pixels indicates the energy deposition in keV.

II.4 The Timepix detector

The Timepix detector is a semiconductor pixelated X-ray imaging detector [20]. It was developed by the Medipix-Collaboration together with CERN and EUDET. Its predecessor was the Medipix2-Detector whose original purpose was X-ray imaging; however, it was quickly apparent that it can be used not only for X-ray imaging but for particle detection as well. But in connection with particle detection it is highly desirable to measure not the particle track only but both the track and the energy. Hence, the Medipix2 was enhanced and the Timepix was developed which included an energy measurement feature and consequently it can be used to measure the particle track and particle energy simultaneously.

Concerning the search for the neutrinoless double beta decay the Timepix has some advantages:

- The detector development is already finished and as opposed to many other experiments no new detector-prototype must be developed at the first step. There is a sufficient amount of detectors which can be used to study their properties for a large scale $0\nu\beta\beta$ experiment.
- Although the detector was originally developed and produced with silicon as sensor material, nowadays chips with Cadmium-Telluride sensors are available. This is particularly interesting because both Cadmium-116 and Tellurium-130 are $0\nu\beta\beta$ candidates and thus the sensor material can be the decaying (source) material at the same time. The decay happens directly in the sensor and both electrons can immediately be detected. No extra decaying material layer is necessary additionally to the detector itself.

  In the final large scale experiment only the decay of Cadmium-116 is to be detected. The reason is the Q-value of Cadmium; it is at about 2.8 MeV, thus larger than that of Tellurium-130 which is at about 2.5 MeV. At higher energies the energy resolution of the detector is better and therefore the required measurement quality can be achieved easier. Another main reason for the usage of Cadmium at 2.8 MeV is that the Q-value is higher than any high-energy γ-line in the natural decay chain (^{208}Tl at 2.614 MeV). High-energetic photons lead to electron-positron pair production in the sensor material but as the Cadmium-116 $0\nu\beta\beta$ decay Q-value is high enough, such events are most unlikely to be confused with $0\nu\beta\beta$ events due to the energy measurement.
- The Timepix is a priori an imaging device; this property can be used to measure particle tracks through the sensor and eliminate undesirable background events. Picture II.7 (a) shows an α-particle measured with the Timepix. It can be clearly recognized and distinguished from an electron which is shown on picture II.6 (d).

The next two subsections deal with the structure of the detector and its functionality in the time-over-threshold mode.

II.4.1 The structure and functionality of the Timepix detector

The Timepix with a USB-readout [21] is shown on figure II.8 (a). One can see two of the three main parts of which a Timepix assembly always consists of: The sensor layer (A) and the Timepix ASIC (C). The readout (D) is necessary to extract the data from the ASIC but is not part of the detector. Let's have a closer look on the three constituents:

The sensor layer is the part of the detector where the physics we want to observe takes place. The material which the sensor layer is made of is a semiconductor - either silicon (Si) or Cadmium-Tellurium (CdTe). As in this work only Timepix detectors with CdTe were used, we will deal only with CdTe as the sensor material. The size of the sensor material is usually about 1.4 cm x 1.4 cm and it is 0.3 mm - 2 mm thick. A 1 mm thick sensor layer was used for this work. The sensor material is the "fiducial-volume", or rather, "the screen" of the detector. Particles which are passing the sensor material are scattered and deposit their energy within the sensor layer. By extracting this energy from the sensor we can make the particle tracks "visible".

The ASIC has two main purposes: On the one hand it is needed to extract the deposited energy information out of the sensor and on the other hand together with the electrodes on the sensor backside it provides the pixelation of the sensor layer. The pixel grid on the ASIC is connected to the sensor layer by the bump-bonds. One pixel on the ASIC is quadratic and has a side length of 55 μm. The distance of the electrodes defines the size of the pixels, called pixel pitch. If every pixel on the grid is connected to the sensor layer the pixel pitch is 55 μm, but chips with 110 μm and 220 μm pixel pitch are available as well. In the last two cases only every second or fourth ASIC grid pixel is connected to the sensor. The number of pixels is 256 x 256, 128 x 128 or 64 x 64, respectively.

The chipboard with the electronics is responsible for the ASIC power supply, supply voltage generation and the data connection from and to the ASIC. The details of its design and functionality are fairly complicated. They are discussed in [20]. We will give only a descriptive insight of the processes important for the understanding of this work.

The two important parts of the electronics as far as this work is concerned are the integrator and the DAC. In the integrator the analogue signal, which is related to the energy deposited in the sensor, is transformed into a digital data packet. This procedure is discussed in the next subsection. The other part is the digital analog converter (DAC). It converts the working parameters of the detector, which can be set and adjusted by the user, from its digital values coming from the computer to analogue values which the electronics can deal with. Therefore the working parameters of the ASIC are named DAC-values, or rather, DAC-settings. Several parameters do not have a big effect on the functionality of the detector and thus will not be discussed. The interesting parameters will be explained on the spot of their first appearance.

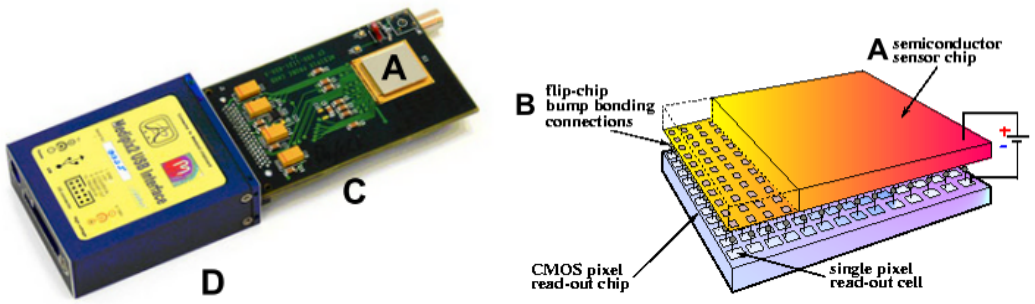

(a) **(b)**

Figure II.8: (a) The Timepix detector E04W0083 with a USB-readout. (b) The structure scheme of a Timepix detector: A - the sensor layer; B - the ASIC with bump-bonds; C - the chipboard with electronics; D - the USB-readout.

As next we will have a look at the detection process. It is illustrated on figure II.9. When a particle (on our illustration a muon) passes the sensor layer, it is scattered and deposits its energy by producing (as CdTe is a semiconductor) electron-hole pairs within the sensor material (1)[1]. The number of pairs is proportional to the energy of the particle. By counting their number, or rather, the resulting amount of charge, we can obtain information about the particle energy.

The electrons, which have been transferred from the valence to the conduction band after being hit by the propagating particle, are available as free charge carriers. While they are drifted through the sensor layer by an electrical drift field $\vec{E}$[2] they induce charge near to the pixel electrodes[3]. This charge is collected at the electrodes above which the particle has passed (3), integrated and shaped to a voltage pulse as shown on picture II.10.

The height of the pulse is proportional to the charge collected in the pixel. The blue line indicates the threshold level (THL), which is a DAC-value. The threshold is necessary as there is always a leakage current due to the bias voltage generating noise in the electronics which is undesirable and have to be suppressed. This signal (red) can be used in different ways. The Timepix detector has three different working modes:

- The Medipix mode: In the Medipix mode the detector counts how many times during the measurement period, called the acquisition time, the pulse height was

1 In the case of a photon, its energy is transferred to a photo-electron and then the energy of this electron is measured.

2 The drift field density for CdTe sensors is usually about 500 V/mm. The bottom of the sensor layer, which is connected by the bump-bonds to the ASIC, is grounded; the upper side is at a potential of -500 V.

3 The charge can be calculated with a so-called weighting potential. Details are described in [22].

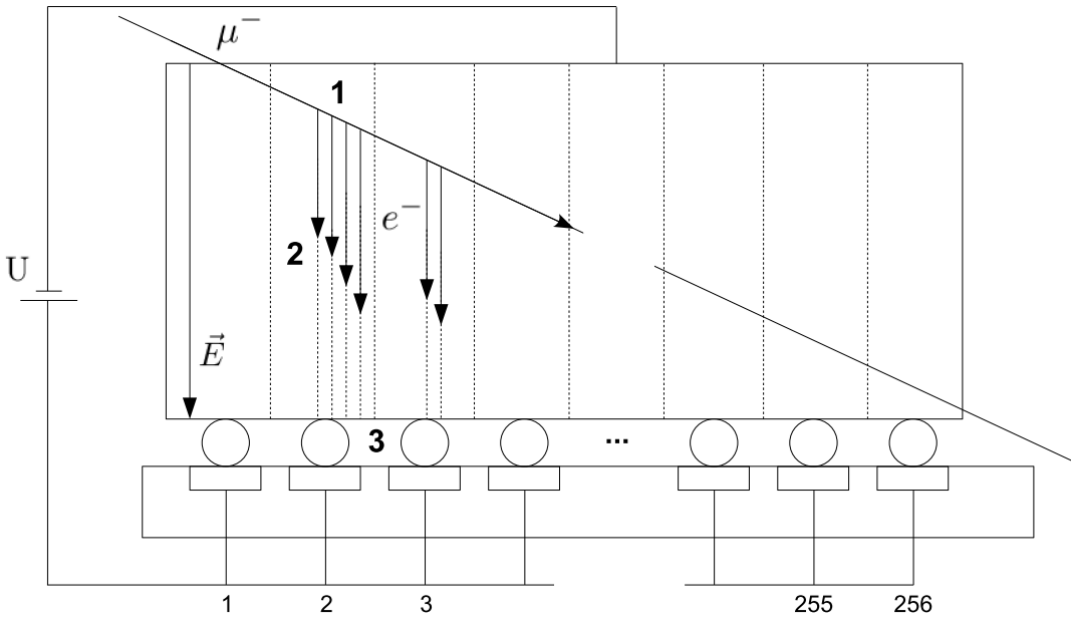

Figure II.9: The detection process in a Timepix detector.

higher than the THL. This number is recorded for each pixel and directed to the detector output.

- The time-of-arrival mode: In this mode the detector counts the time (in digital units) from the first time the pulse is above the threshold level until the end of the acquisition time.
- The time-over-threshold (TOT) mode: In this mode the length of the pulse above the THL is measured to provide information about the energy deposited in a pixel.

As mostly the detector was used only in the TOT mode for this work, we will omit the details about the Medipix and the time-of-arrival mode but explain the TOT mode in detail.

For the interaction between the detector and the user the "PixelMan"-Software is used. It provides all features that are necessary to communicate and work with the detector. The details on particular parts of the software will be given at the point they are needed. Throughout the whole work PixelMan Version 2.01.03, Built date 04 August 2010 was used. A full documentation on the software can be found in [21].

II.4.2 The time-over-threshold mode

As stated above this mode is used if the collected energy deposition for each pixel is of interest. The height of the pulse is related to the charge and consequently to the energy deposition. The pulse form can be adjusted by the DAC-values. The biggest effect have

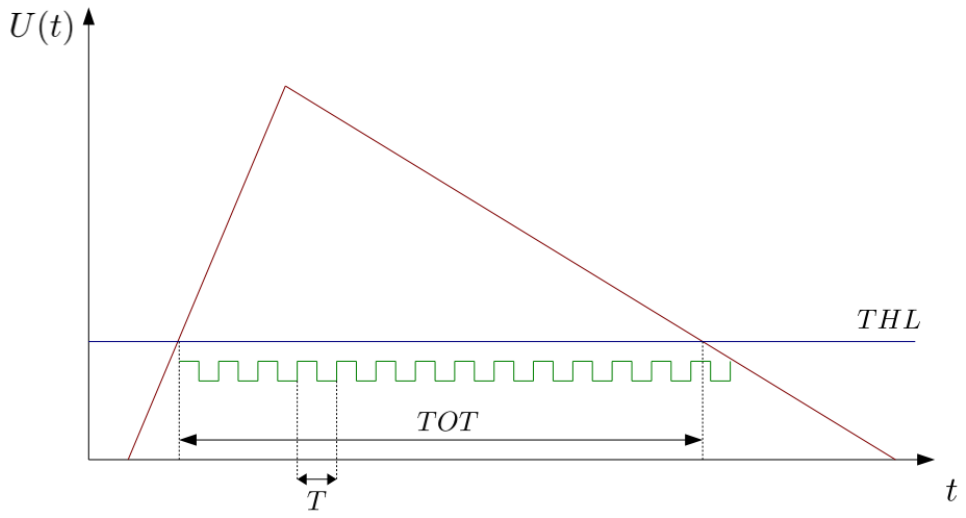

Figure II.10: The voltage pulse (red) after integration. The blue line is the threshold level.

the so-called "PreAmp", which regulates the gain of the preamplifier, and the "IKrum". If you imagine the integrator basically (neglecting the details of the electronics) as a capacitor, which is charged and discharged during the measurement process, the pulse is the voltage measured over the capacitor and IKrum is the intensity of the discharging current. Therefore you can regulate the height of the pulse form by the PreAmp and the pulse length by the IKrum. Higher PreAmp and IKrum values make the pulse higher and shorter, respectively, and vice versa (see figure II.11). Details an this can be found in [20].

If we fix the DAC-values the pulse form will be approximately the same regardless the height of the pulse and therefore the pulse length will be related to the pulse height and thus the energy position. In the TOT mode the part of the pulse is taken into account which is over the threshold (THL line). This is necessary to avoid measurement errors caused by noise. The time between the points, where the pulse rises above and falls below the threshold level, is called time-over-threshold or abbreviated TOT. This is actually the quantity that is measured and that contains the information about the energy deposition.

When the pulse rises above the discrimination threshold a counter starts and stops after the pulse falls below it. It counts the number of quantized clock pulses created by a frequency generator of frequency f. The distance between the clock pulses is

$$\Delta T = \frac{1}{f} \tag{II.19}$$

and f can be chosen as 10 MHz, 20 MHz, 40 MHz or 80 MHz. The relation between the TOT and the energy deposition E can be approximated by

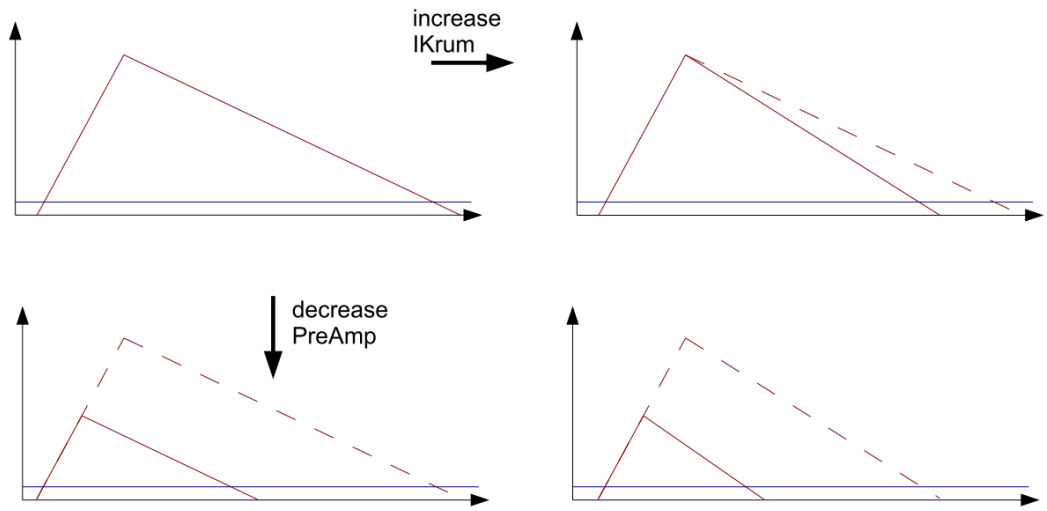

Figure II.11: The dependence of the pulse shape on the DAC-values "PreAmp" and "IKrum".

$$TOT(E) = a \cdot E + b + \frac{c}{E - t}, \tag{II.20}$$

or inverted

$$E(TOT) = \frac{at + TOT - b + \sqrt{(b + at - TOT)^2 + 4ac}}{2a} \tag{II.21}$$

This formula is empiric and was introduced in [23]. Due to fabrication tolerances the parameters a, b, c and t vary among all pixels and have to be determined before a detector can be used in the TOT mode. This procedure is called pixel-by-pixel calibration. It will be discussed in detail in chapter III.

II.4.3 Some important expressions concerning the Timepix

In this subsection we want to introduce some particular expressions which will appear often in this work in connection with the Timepix.

Charge sharing After charge is induced in the sensor layer, it needs about 20 ns to arrive at the cathode. During this time the diameter of the charge cloud is increased by diffusion and repulsion of the charge carriers (see figure II.12). Therefore a part of the charge is

deposited not in the main pixel (in which the energy was actually deposited) but in the neighbour pixels as well. (On the scheme the blue part of the charge is detected correctly but the red is either detected in the wrong pixel or lost if it is below the threshold energy.) This effect is highly unfavorable as it distorts the energy deposition information and hence limits the energy resolution of the detector. A detailed discussion about this effect is given in [22].

Escape Peaks occur when a fluorescence photon leaves the primarily hit pixel. The remaining photo electron (escape electron) is detected in the hit pixel with the energy E_e

$$E_e = E_\gamma - W, \tag{II.22}$$

where E_γ is the energy of the incending photon and W the ionization energy of the electron in the particular shell. This effect leads to an additional peak at the energy E_e in the spectrum left to the full energy peak at the energy E_γ.

ROSI is a software written to simulate electro-magnetic interactions within the sensor layer and the ASIC. It can provide the response of the detector to various events which can be generated by decay0. Details on ROSI are given in [22].

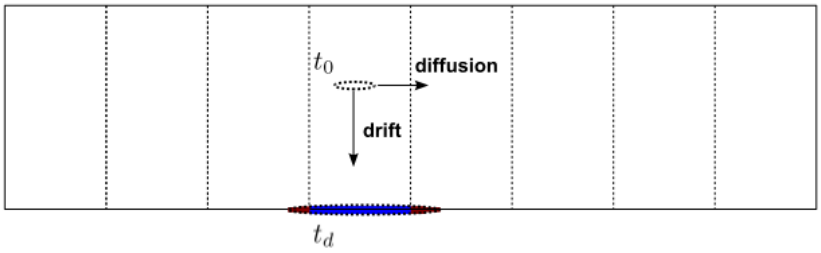

Figure II.12: The charge cloud at t_0 is drifted towards the pixelated side of the sensor. At the arrival time t_d it is broadened and a part of the charge (red) is collected in the wrong pixel.

III Calibration Procedure and Energy Resolution for Single Hits

Contents

III.1 Threshold equalization . . . 27
III.2 THL calibration . . . 29
III.3 TOT calibration . . . 36
III.3.1 Global calibration . . . 36
III.3.2 Pixel-by-pixel calibration . . . 49
III.3.3 Calibration curve reliability . . . 57
III.4 Energy resolution for single pixel hits . . . 61
III.4.1 Differences between global and pixel-by-pixel calibration . . . 63
III.4.2 Dependence of the energy resolution on working parameters . . . 65
III.5 Summary . . . 71

This chapter deals with the calibration procedure of Timepix detectors with CdTe-sensors in the TOT-mode. Although the idea of calibration is straight-forward and the calibration of Si-based Timepix detectors has already been performed successfully (see [24]), the specific properties of CdTe call for a testing of the calibration procedure and the functionality of Timepix detectors with CdTe. This will be discussed in this chapter. In the last section we will discuss the energy resolution quality of our detector.

In this work we used the detector E04W0083. Its sensor layer's dimensions are 1.4 x 1.4 x 0.1 cm and its weight is about 1.31 g as the mass density of the CdTe on the ASIC is about $\rho_{CdTe} = 5.85 \frac{g}{cm^3}$. It is lower than the density for a perfect CdTe crystal (6.20 $\frac{g}{cm^3}$) because of impurities in the lattice. The detector is a class A detector, which means it is a high quality detector with only very few defect pixels (sometimes called "bad pixels").

For all our measurements the detector was connected to the computer by a USB-readout. Its frame rate is 3 Hz. Therefore a complete detection frame can be transmitted from the ASIC to the computer approximately every 0.33 s, even if the real observation frame time is shorter. The USB readout has its own power supply[1]. The computer in use

1 Please note, that sometimes a **reversed polarity power supply** has to be used for the USB readout and a normal power supply will damage the device.

was a Fujitsu-Siemens desktop PC with an Intel Core 2 Duo CPU at 3.00 GHz, 2 GB RAM and a USB 2.0 connection.

The sensor voltage supply was an iseg SHQ-122M which has to be set to negative polarity for CdTe detectors. The bias voltage we applied was 500 V and the usual leakage current was about ~3-4 μA. The current in the sensor layer corresponds to changes in the bias voltage in a sensitive, non-linear way: If the bias voltage is increased, the current increases exponentially but then drops down to a particular level asymptotically if the bias voltage is kept at fixed value. As it is recommended to avoid currents higher than 40 μA, the voltage cannot be increased from 0 to 500 V in one run (because then the current would exceed 40 μA) but has to ramped: First you increase the voltage until the current reaches about 20 μA and then wait for a certain time (about 5 - 12 minutes) until it drops back to a constant level. Both steps are repeated until the voltage reaches 500 V.

The general measurement setup (detector, USB-readout, voltage supply, computer and cables) is shown on figure III.1.

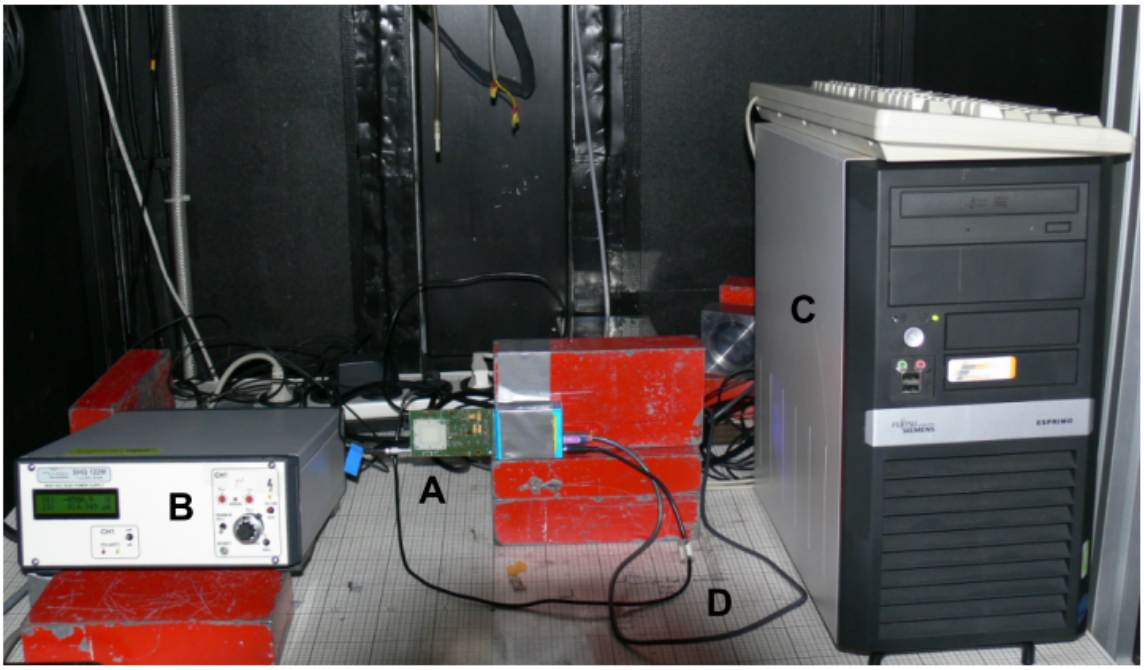

Figure III.1: The basic necessary equipment used for measurements with the Timepix detector: (A) the Timepix with USB-readout, (B) bias voltage supply, (C) computer and (D) cables.

III.1 Threshold equalization

Before a Timepix detector can be used properly, the analogue threshold equalization has to be performed. This is necessary because all the pixels are not really identical but have slight differences in their electrical properties due to fabrication. Therefore every pixel has a different noise level. If only one fixed THL value is used for all pixels, the threshold energy will vary among all pixels (see figure III.2 (a)) and they will all get noisy at different THL. Hence the threshold energy has to be adjusted for each pixel individually. For every pixel the threshold energy can be shifted up or down within a small interval around the threshold energy given by the THL and after this is done for every pixel the threshold energy is at the almost same level for all pixels (figure III.2 (b)).

The adjusting process is called threshold equalization and can be performed automatically by the PixelMan Software[1]. In the threshold equalization window[2] you can start this process. Several parameters can be set which have an influence on the quality and the duration of the process:

- Spacing: If all pixels are equalized at the same time, they can affect each other and degrade the quality of the equalization. To avoid this problem the equalization can be done for a set of pixels which have at least a particular distance which can be set by the spacing parameter. If, for instance, the spacing is set to 2, only one pixel and its second neighbours (see figure III.3) will be equalized at the same time (then the next set of neighbours and so on); for spacing 3 the third next neighbour etc. Of

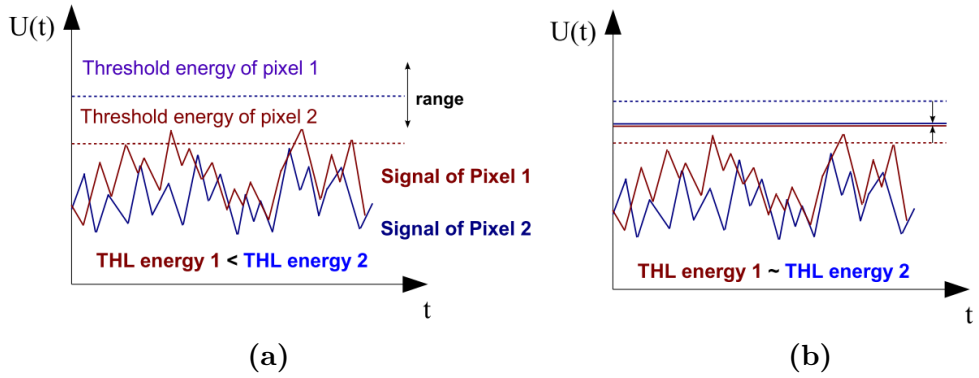

Figure III.2: The reason for the threshold equalization: The threshold energy vary among all pixels (a). After the threshold equalization, the threshold energy is at the same level for every pixel (b).

1 Before performing the THL calibration, make sure that the polarity is set to negative (Medipix Control → Options → Device Settings... → Polarity).

2 Medipix Control → Tools → Threshold Equalization

course, the time which is required for the equalization process rises with the spacing quadratically.

- Interpolate: If this parameter is set, the software will interpolate between various measurement points. For a good equalization the interpolation should be turned off.
- Acquisition count and time: The time and number of repetitions for one particular measurement run.
- THL/THH Range automatic: If this is set true, the software will adjust the THL automatically to an optimal level in the given range. This process increases the time for the equalization linear (depending on the step and the range).
- Optimize THS: If this is set true, the software will adjust the THS automatically to an optimal level by the step size which is set. The time for the equalization will depend on the step size set (diminishing with increasing step size). For a good equalization the THS should be optimized.

After the procedure, the resulting settings for the pixel grid are called an adjustment mask. Masks can be saved and loaded when they are needed for a measurement process. Creating a good mask is a business on its own and was explained explicitly in [25]. A mask can be considered as good, or rather, useful to work with if the distance between the actual distance σ and the, so-called, optimal distance σ_{opt} is not greatly bigger than $\Delta\sigma = \sigma - \sigma_{opt} < 0.1$.

At this point it is not important define the distance explicitly; it can be considered as a quantity to check the mask quality. Details are given in [25]. For the detector that was used in this work the threshold equalization settings, the process duration and the mask quality are listed in table III.1. We could not achieve a better distance than $\Delta\sigma = 0.21$ with the time we had to be spent on the threshold equalization.

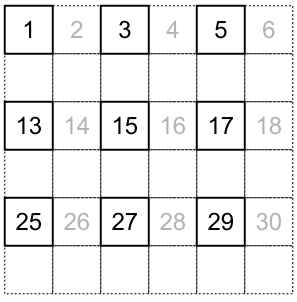

Figure III.3: Spacing 2: Only pixels 1, 3, 5, 13, 15, 17, 25, 27 and 29 are adjusted at the same time.

Chip	Settings	Duration	Quality
E04W0083	interpolate = false Acq. count 2 acq. time 0.2, spacing 4 THL Range 1 - 500, Step 2 TH count 3	3874.1 s	$\Delta\sigma = 0.21$

Table III.1: The threshold equalization settings and results.

III.2 THL calibration

The next step after a good mask was created is the THL calibration. The THL DAC-value, that can be set by the user, is a digital value, but not a physical quantity. Actually, what we are interested in is the lowest amount of energy which has to be deposited in one pixel that can still be measured if a particular THL value was chosen. We need to determine an interdependence between the THL DAC-value and the threshold energy measured in keV; this is what is done during the THL calibration process. It is possible to perform the THL calibration for a whole pixel matrix or for each pixel individually, which is of course a much more valuable information. For details on the THL calibration of CdTe Timepix detectors consult reference [26].

How to perform this task? First you set a THL value high enough above the noise level, i.e. you choose a THL value high enough that every "good behaving" pixel is not counting. Good behaving means that a pixel is not defect and therefore permanently counting. Now you take a source with a well known γ-radiation spectrum and place it in front of the detector. The distance d between the source and the detector (see figure III.4) and the acquisition time T_f of a frame have to be adjusted properly to fulfill two requirements: On the one hand you want as many counts in a pixel as possible, but not more than the counting limit per frame, which is 11280 counts per frame, and on the other hand you want to have a homogeneous intensity distribution all over the sensor. Both requirements are important to get a good counting statistic in every pixel.

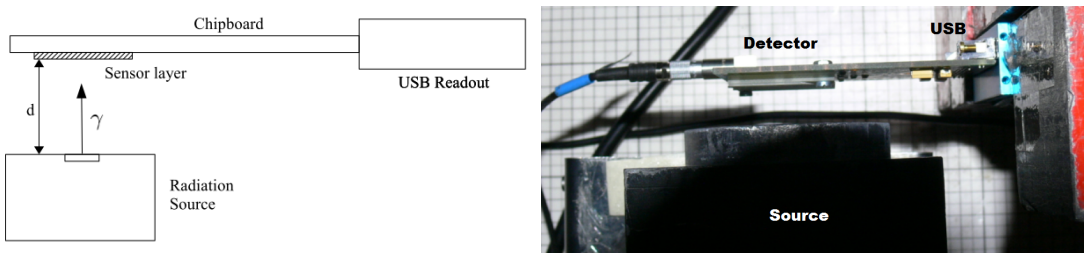

(a) scheme **(b)** setup

Figure III.4: The schematic setup for the THL calibration and a photography for the real setup. The distance d was 1 cm in the real setup.

Normally the illumination is good enough if you have a distribution of hits per pixel as shown on figure III.5 (a). It is a Gaussian distribution around 5000 hits, which is not broader than the counting limit of 11280 hits[1]. On figure III.5 (b) a distribution is shown on which the Gaussian is two far right; too many pixel are at the counting limit. To check the accuracy of the radiation source positioning you can take a long duration (between 2 seconds and 6 seconds, depending on the distance d) frame and have a look at the real time hit results[2]. Figure III.6 (a) shows a good positioning - the sensor is illuminated almost homogeneously. As opposed to this on picture III.6 (b) the source was positioned too far right[3].

Now, after the experimental setup was prepared, you start to take data at a THL value at which most of the pixels are noisy. After each frame the THL value is raised and the amount of hits for each pixel is measured. After the THL level goes over the energy of a particular γ-line of the radiation source, the amount of hits drops abruptly. Therefore, if you plot the derivative of the recorded data, you will see peaks at the points at which the amount of hits dropped. As the spectrum of the radiation source is known, the peaks at a particular THL level can be related to the γ-line energies of the source.

Our experimental setup is shown on figure III.4 (b). We performed only the global THL calibration for our detector. The source-detector distance d was 0.9 cm, the acquisition time $T_f = 3.5$ s and the number of frames was 20. We took only measurement points with odd THL values and skipped the even to save on measurement time. Nevertheless, as the THL scan range goes from about 150 to 650, the measurement results are not affected

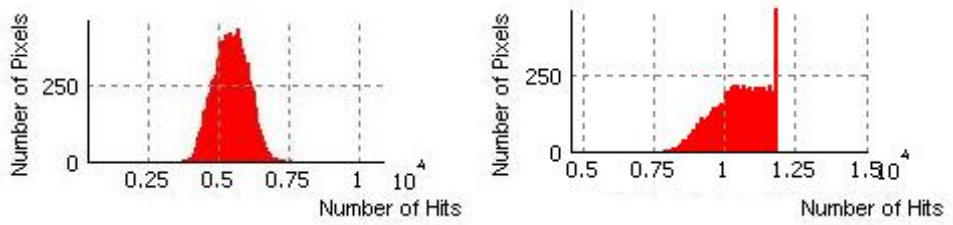

(a) good **(b)** bad

Figure III.5: The hits per frame distribution for a 110 μm pixel pitch Timepix. On (a) a good distribution is shown whereas on (b) the distribution is too far right and several pixels are saturated.

1 Actually, a very thin Gaussian distribution around 10000 hits would be desirable, but cannot be achieved practically in the usual case.

2 Open the Preview for "Medipix Control" window and set the "Auto update preview" check box true. The Min level and Max level should be set to values which are approximately the left and right endings of the pixel hit distribution.

3 If you have enough measurement time, it is always better to have a larger distance d between the source and the detector to have a homogeneous illumination; however, increasing the distance will rapidly increase the required measurement time to get the same hit statistics per pixel.

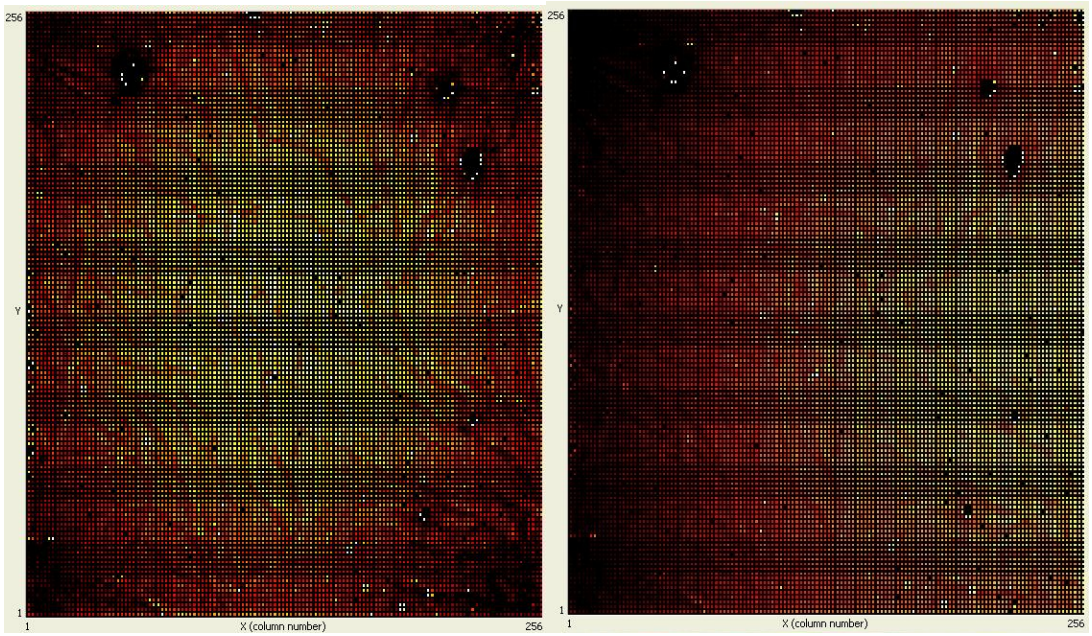

(a) good **(b)** bad

Figure III.6: The illumination of a Timepix sensor layer. On (a) a good, centered positioning is shown whereas on (b) the positioning has to be readjusted.

badly by this. We used an Americium-241 (^{241}Am) source with an activity of 1.1 GBq. Its main γ-line is at 59.54 keV.

The data recording process is done automatically by the PixelMan Software. On figure III.7 the threshold calibration window is shown[1]. Here you have to choose that the THL has to be increased step by step and the step size. For reasons of data storage it is convenient to set the output to single ASCII file. The measurement lasted about 5 hours.

The data we have after the measurement are ASCII files containing 256 x 256 matrices. The entries are separated by a whitespace and they contain the number of hits a pixel counted during the frame measurement time T_f[2]. At the end of the filename the THL value and the repetition number for the particular THL is stated:

$$\underbrace{\text{20101020\_E04W0083\_Am241\_THLcal}}_{\text{Measurement name}}\_\ \underbrace{\text{170}}_{\text{THL value}}\ \_\ \underbrace{\text{r00001}}_{\text{Repetition number}}$$

This data is evaluated with a self-written script which uses the ROOT package [27].

1 Medipix Control → Tools → DACs Scan

2 Although a detector with 110 μm pixel pitch has only 128 x 128 pixels, the matrix still contains 256 x 256 entries but every second row and column are filled with zeros

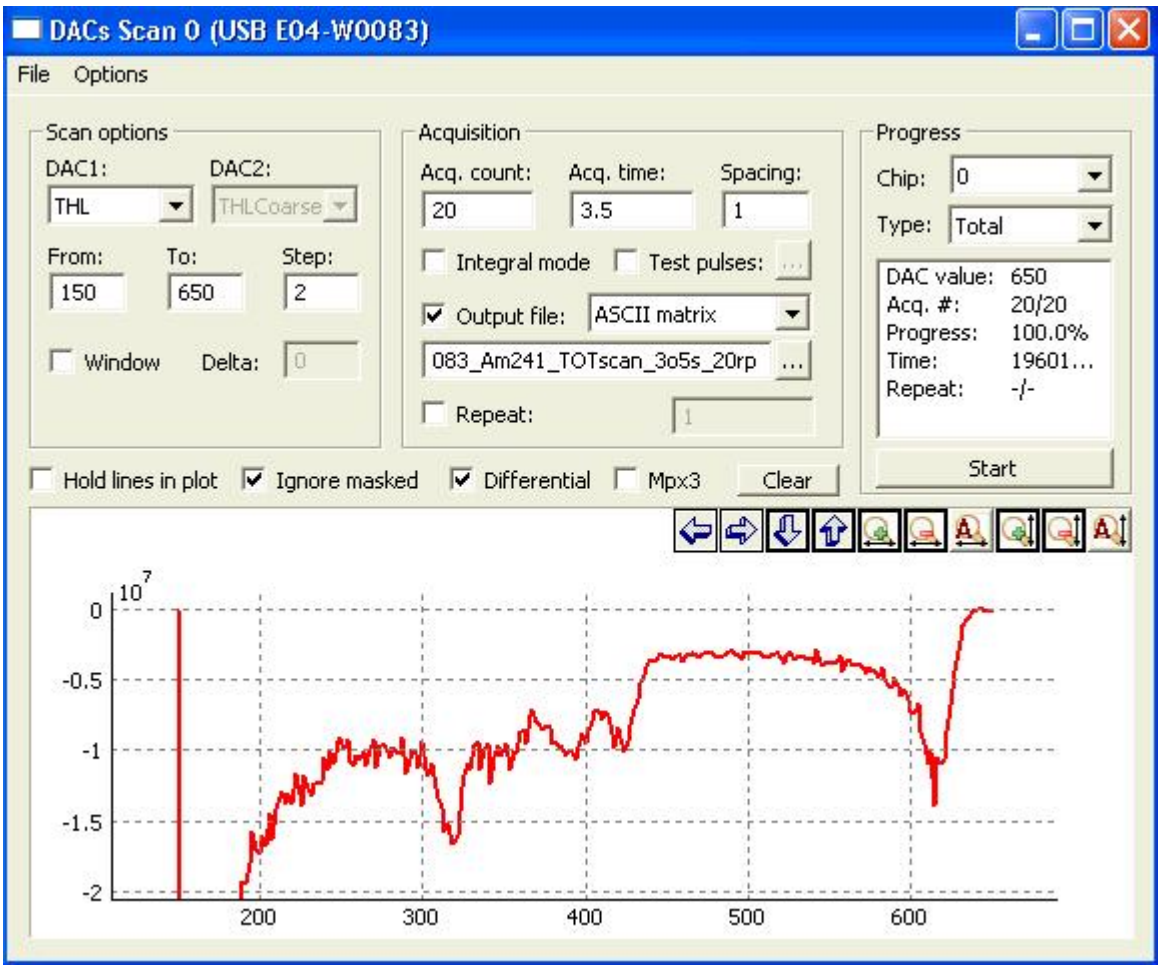

Figure III.7: The THL calibration window of PixelMan.

It sums up the hits of the matrix for all repetitions at a particular THL value and sorts it into a THL value versus hits histogram as it is shown on figure III.8 (a). The derivative of this distribution (which can be automatically calculated by a ROOT routine) is shown III.8 (b). Five peaks can be found. We can identify them and relate them to the following energies:

- The very right (fifth) peak corresponds to the main radiation energy of ^{241}Am at 59.54 keV.
- The first peak from the left is the K-fluorescence of Cadmium at 23.106 keV. It is actually a mixture of the K_α-lines and occurs when the shell of the Cadmium atom relaxes back into equilibrium after an electron in the K-shell was removed by the photons of the ^{241}Am radiation.
- The second peak from the left is an overlay of the Tellurium fluorescence peak (mixture of K_α-lines) at 27.377 keV and the Cadmium K-fluorescence peak (mixture of K_β-lines) at 26.091 keV.

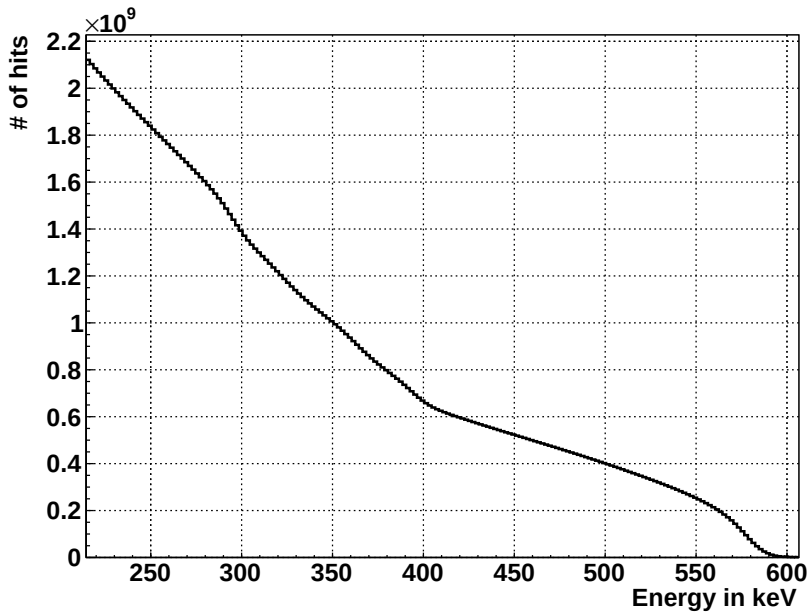

(a) measured

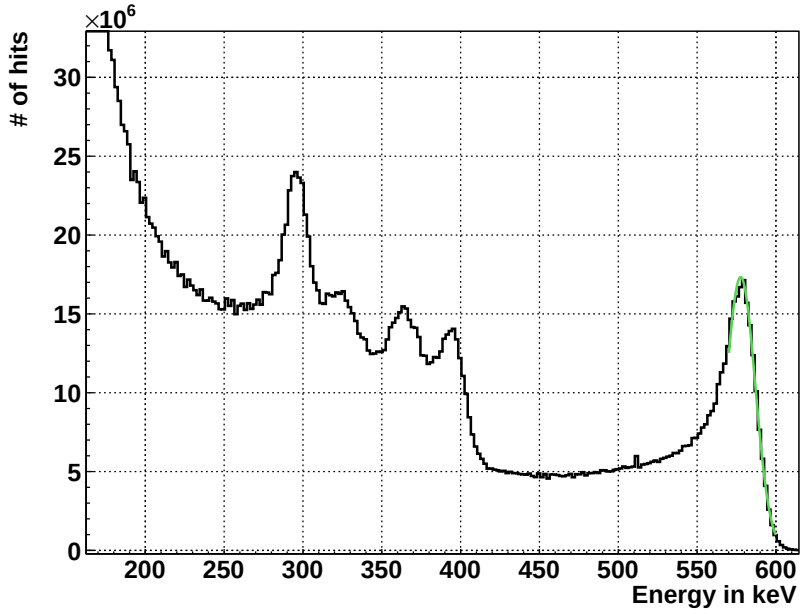

(b) differentiated

Figure III.8: The measured (a) and differentiated (b) THL scan spectrum of ^{241}Am. The green curve is the fit with a Gaussian.

- The third peak from the right is an overlay of the Tellurium fluorescence peak (mixture of K_β-lines) at 30.990 keV and its own escape peak at 28.55 keV.
- The fourth peak is the escape peak of Cadmium at 36.343 keV.

We fitted the peaks by a Gaussian distribution of the form

$$N(THL,\mu,\sigma,A) = A \cdot \exp\left(-\frac{(THL-\mu)^2}{2\sigma^2}\right) \tag{III.1}$$

(as shown for the last peak at 570 THL on figure III.8) and used the μ of the fit results to relate the THL value to the threshold energy in keV . Assuming that the THL value versus threshold energy interdependency is linear (which is a good first approximation [24]), we can interpolate between the five points that we derived from the peaks and obtain a calibration function

$$THL(E) = a \cdot E + b \tag{III.2}$$

as shown on figure III.9. We used the fit error of μ for the error bars.

The global calibration can be used if you don't have enough statistics or do not need to deal with each pixel individually. For our purposes a global calibration is enough as we only want to estimate the threshold energy. The global calibration results for the detector are listed in table III.2.

Now the real threshold energy can be estimated. We set the THL slightly above the noise level and calculated the threshold energy E from the inverted calibration curve $E(THL)$ obtained by inverting formula III.2. Again, this can be done for each pixel individually or an average value for the whole matrix can be calculated from the global calibration, which is the last column of table III.2.

Important note: We observed a discrepancy between the THL calibration and measurements in the TOT mode in the following way: We recorded the spectrum of Cooper and Gadolinium in the TOT mode and could clearly observe a peak at about 8 keV (K_α

a $[\frac{1}{keV}]$	b	THL_{noise}	E_{noise} [keV]
7.835 ± 0.532	115.095 ± 23.08	179 ± 21	8.23 ± 5.84

Table III.2: The results of the THL calibration.

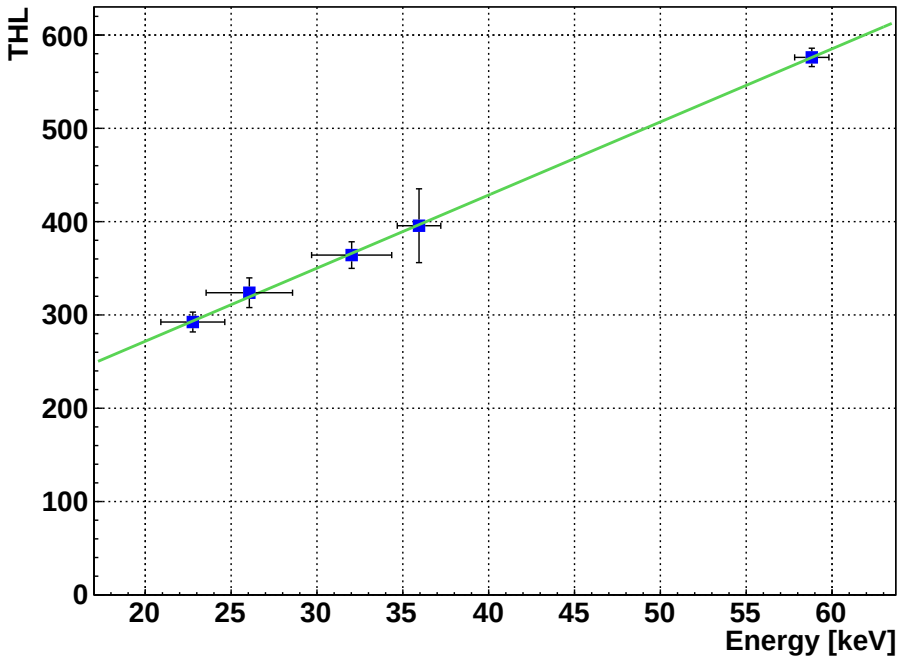

Figure III.9: The THL calibration line for the whole matrix of the 110 μm pixel pitch Timepix E04W0083 performed with ^{241}Am. The fit function is f(x) = a·x + b, with a = 7.835 ± 0.532 $\frac{1}{keV}$ and b = 115.09 ± 23.98.

fluorescence of Cu) and at about 6 keV (L_α fluorescence of Gd), respectively[1]. Later we will see, that these peaks are in good agreement with the calibration curve and therefore we think that they are not any kind of artifacts, but real peaks. From this point of view the threshold energy would be at about 5.5 keV. In contrast the THL value that we used for these measurements was 190, which corresponds to a threshold energy of about 8.2 keV.

1 The measured spectra can be found in Appendix A. You can compare the peaks to others at 17.41 keV, for instance, and will observe, that the peak form of the low energy peaks is not distorted, but does match pretty good.

III.3 TOT calibration

Since the time-over-threshold (TOT) is only a digital but not a real physical quantity, we need to provide a method of calculating the deposited energy in keV from the TOT which is actually measured: We want to establish an interdependency between the TOT and the deposited energy E - E(TOT). The procedure of obtaining the E(TOT) calibration curve is called TOT calibration. It can be done for each pixel individually or for the whole matrix. The TOT calibration procedure consists usually of the following steps:

1. Recording the TOT spectra of well-known γ-radiation sources.
2. Identifying the peaks in the TOT spectrum and relating them to the photon energies emitted by the radiation source.
3. Fitting the peaks and inserting them into a TOT versus energy diagram.
4. Fitting a calibration curve TOT(E) through these points and inverting the curve to get an E(TOT) interdependency.

In the following section we will discuss step by step the TOT calibration for the whole matrix (we will call this global calibration) and its specific features as far as CdTe Timepix detectors are concerned[1] .The second part deals with the details of calibrating the detector pixel-by-pixel.

III.3.1 Global calibration

Measuring and fitting of the TOT spectra

The first step in the calibration process is to record the TOT spectra of well-known radiation sources and identify their γ-lines in the recorded TOT spectra. We can use two kinds of radiation:

γ-lines after radioactive decays of materials which undergo spontaneous decays with a preferably high branching ratio[2]. A high branching ratio is desirable to have monochromatic radiation in a particular energy interval. The experimental setup to use this kind of radiation is pretty simple (schematically shown on figure III.4 (a)). In fact, it is the same as for the THL calibration and therefore shown on the figure above. The radioactive source has to be positioned at a fixed distance d from the detector. The distance d has to be chosen large enough to insure a homogeneous illumination of the sensor layer and at

1 The calibration of Si-based Timepix detectors is discussed in [24] in detail.
2 The branching ratio of a particular decay is its probability to undergo this particular decay compared to all decay channels possible.

the same time to optimize the photon flux intensity according to the source activity and acquisition time. A photo of the real setup is shown on figure III.4 (b).

X-ray fluorescences ,i.e. K_α- and L_α-fluorescence lines of particular materials. Now the experimental setup will be more complicated since to excite those transitions, electrons of the K- or L-shell have to be extracted out of the atom. Therefore an external X-ray source is necessary. The energy of the photons emitted by the source have to be higher than the ionization energy of the K-shell and it is convenient to be able to regulate the source's photons' energy and intensity. Additionally a stable photon flux over a time period is needed. Commercial continuous wave X-ray tubes can fulfill these requirements. We used an YXLON FXT-160.51 Ver. FXE X-ray tube for our experiments.

The geometry of the experimental setup is shown on figure III.10 (a): The exit window (1a) of the X-ray tube (1b), which is at a height of $h_s = 22.5$ cm, has to be surrounded by massive lead blocks (2a) as the radiation angle of the tube is almost 2π and we need to shield the detector from the main radiation of the X-ray tube, which provides undesirable background. Our lead blocks were 5.0 cm thick, the wall had a height of 35.9 cm and a length of 51.3 cm. The hole in the lead wall for the X-rays to penetrate was 1.0 cm wide and 6.0 cm high. To reduce the intensity of the background radiation even further, we put two collimators (3a, 3b) in front of the target material (4) in the way of the main beam. The collimators were 5.0 cm thick and had a hole radius of 0.7 cm (3a) and 1.2 cm (3b). We used a LASER system to adjust the geometry for the main beam properly before fixing the target in front of the collimators. The angle between the main beam and the center of the target material ϕ_1 was approximately 100° and the center of the sensor layer (5) was hit at an angle of $\phi_2 \approx 82°$. Behind the detector, additional lead (2b) provides the shielding of background radiation caused by the reflection of the main X-ray radiation from the walls of the lead chamber which the experiments are performed in. The USB-readout of the detector is taped to a lead block to fix the detector's position. A photo of our experimental setup is shown on figure III.10 (b). The distance between the exit window and the center of the target material was b = 18.0 cm, the distance between the center of the target material and the center of the sensor layer was d = 20.6 cm.

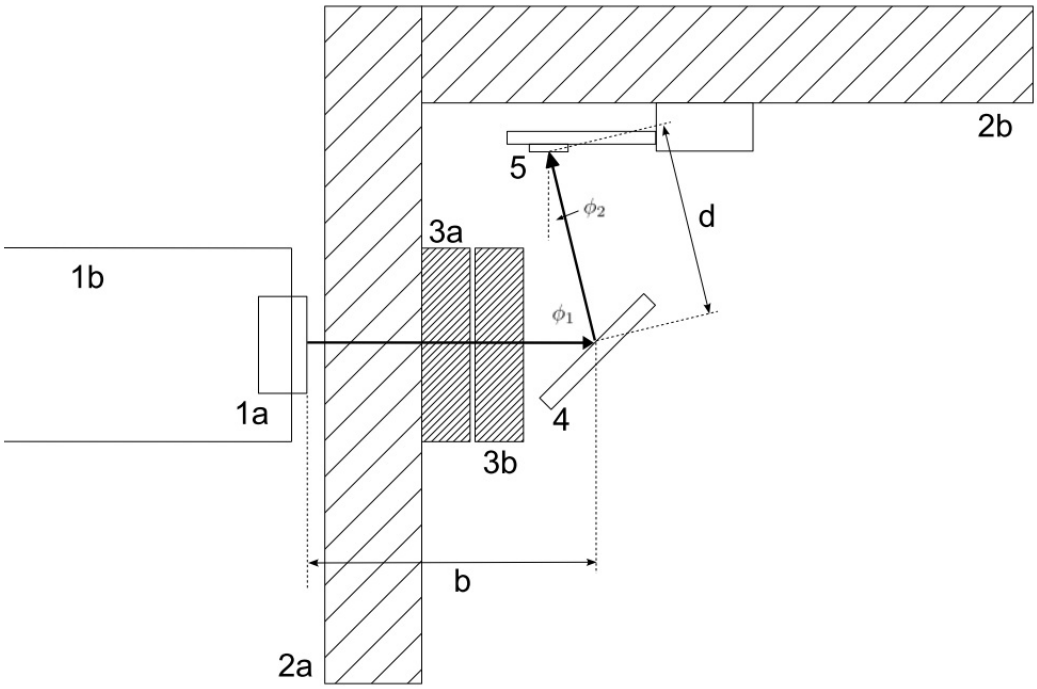

(a) sketch of the experimental setup

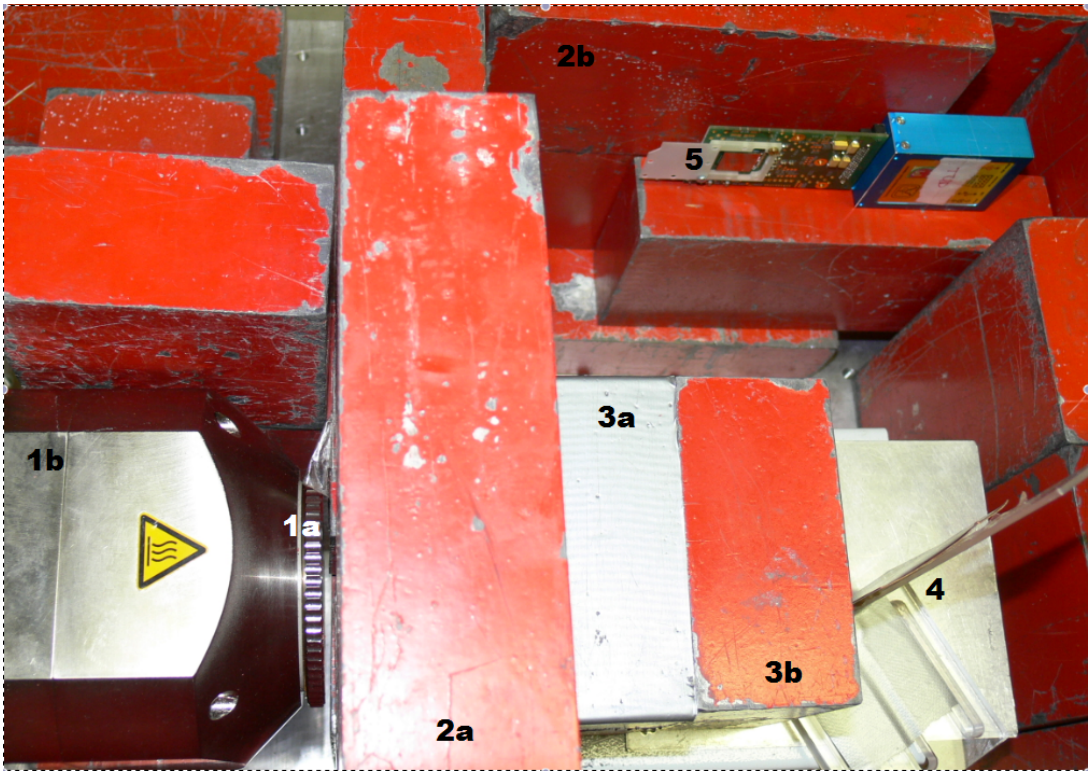

(b) real setup

Figure III.10: The experimental setup for calibration measurements with fluorescence radiation sources; the bold line is the way of the ray propagation. (a) sketch; (b) photography of the real setup.

For the recording of TOT data we used the PixelMan Software [21]. Before the measurement a mask has to be loaded[1], the polarity (negative) and the clock frequency have to be set[2]. For all our measurements we used a clock frequency of $f = 80$ Mhz[3]. Now the DAC settings have to be fixed in the "DAC Control Window"[4] because the measurement results (and therefore the calibration) depend highly on the particular DAC settings. We will discuss this dependency later to optimize the energy resolution of the detector. The DAC settings that we used for our detector to record the TOT spectra for the calibration can be extracted from table III.3. After setting the detection mode to TOT[5], the acquisition time (or frame time) T_f and the number of frames N_f, a measurement can be started and the results can be observed in real time in the "Preview for Medipix Control" window[6]. The frame time T_f and/or the distance from the radiation source to the detector have to be adjusted in such a way that,

- there are about 180-220 hits on the detector per frame[7] in the case of a 110 μm pixel pitch Timepix. For this counting rates a large percentage of the hits will be single hits, what means that a pixel is hit only once but not more often during the frame time. This is necessary to have a sharp peak and good statistics at the TOT values of the sources' main γ-lines.
- the detector is illuminated homogeneously. This can be tested by setting the mode back to the Medipix mode and taking frame with a long frames time (15 - 60 s). Then after adjusting the Min and Max level settings, the hits should be distributed approximately homogeneously over the pixel matrix. A good illumination[8] is shown back in section I.2 on figure III.6.

In connection with the frame time adjustment we want to mention that the measurement speed is always limited by the readout used. If it is a USB-readout, it can send the frame data to the computer only every 0.33 s (at a frequency of $f_r = 3$ Hz; if it is a MUROS-readout, then the data can be transferred at a frequency of $f_r = 20$ Hz.) Therefore in order not to enlarge the measurement time unnecessarily, a frame time $T_f < \frac{1}{f_r}$ should be used if it is reasonable and possible.

After these requirements are fulfilled, a measurement can be started. Concerning the global calibration we always recorded 11000 frames for a particular radiation source with

1 Medipix Control → File → Load Binary Pixels Cfg... . Make sure, that in Medipix Control → Options the "Load/Save DACs with Pix. Cfg." is on if you want to load your DAC settings with the mask.
2 Medipix Control→ Options → Device Settings... → Interface Specific Info → Timepix Clock
3 Make sure to check it before taking long measurements since it occurred that it was set back by the software automatically after restarting it.
4 Medipix Control → Tools → DAC Control Panel
5 Medipix Control → File → Set Mode → Time over Threshold
6 Make sure that the Auto update preview check box is on.
7 Discussed more detailed in [24].
8 Another possibility to check the illumination quality afterwards, is to plot the number of counts during the whole measurement time versus the number of pixels with this number of counts. Only a homogeneous illumination will produce a clear Poisson distribution.

DAC setting	Value
IKrum	10
Disc	127
Preamp	210
BuffAnalogA	127
BuffAnalogB	127
Hist	0
THL	190
THLCoarse	6
Vcas	130
FBK	100
GND	80
THS	66
BiasLVDS	128
RefLVDS	128
Ext DAC	0

Table III.3: The DAC settings used during the measurements.

such a frame time that at about 180-220 pixels were hit during one frame. First we will discuss the TOT spectra of the γ-lines of radioactive sources. We used ^{241}Am, ^{57}Co, ^{133}Ba and ^{137}Cs as radioactive sources. The source properties are given in Appendix A. The distance d (which was in the range between 0.3 cm and 40 cm) and frame time T_f were adjusted to the source's intensity for each measurement.

The measurement data is saved into one single ASCII file containing 11000 matrices of the size 256 x 256. The entries are separated by a whitespace and they contain the TOT which a pixel measured during the frame time T_f[1]. For every ASCII matrix file a ".dsc" file is created which contains additional measurement information such as the DAC settings or the clock frequency used during the measurement. This data is converted into a ROOT file by the MediROOTconverter [28] since this file format requires much less disc space and can be handled in an easier way during further evaluation.

If you fill the TOT entries of the matrix in a number of counts (i.e. how many times a particular TOT value was counted during the whole measurement time) versus TOT histogram[2], you get the TOT spectrum[3]. The TOT spectra of ^{241}Am and ^{57}Co are shown on figure III.11 (a) and III.11 (b), respectively. The statistical error bar for

1 Although a detector with 110μm pixel pitch has only 128 x 128 pixels, the matrix still contains 256 x 256 entries, but every second row and column is filled with zeros.

2 The bin edges are at 0.5 of every entry, i.e the first interval is [0.5;1.5], the second [1.5; 2.5] and so on. Thus the bin number is equal to the TOT value contained in it.

3 This is actually done by the MediROOTconverter already and the TOT-spectrum is the "MPX_countervalue" histogram in the sparse tree.

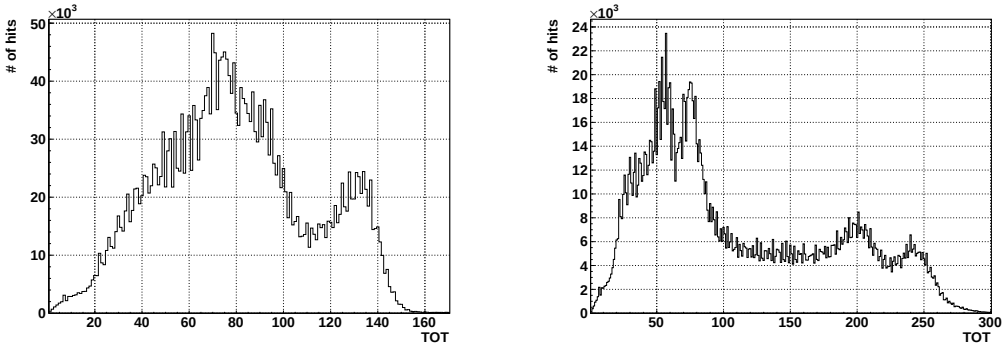

(a) ^{241}Am **(b)** ^{57}Co

Figure III.11: The TOT spectra of (a) ^{241}Am and (b) ^{57}Co without single clustering.

every individual bin is really small as the number of entries in every bin is about 10^4 and therefore cannot be seen at the plot. The abrupt jumps between the TOT values are due to a bug in the electronics which has been understood but not fixed by the time our experiments were carried out. Although it is already possible to recognize distinct peaks (two for ^{241}Am, four for ^{57}Co) in the spectrum, it is possible to increase the spectrum quality by a procedure called "single clustering".

Single Clustering The idea of singe clustering is to increase the spectrum quality by avoiding the effect of charge sharing[1]. If, for instance, two neighbour pixels are hit during one frame, it can happen that they exchange charge and the individual measured TOT is falsified. Another possible scenario, if two neighbour pixels are counting, is that one of them was hit near to its edge by a high-energy photon and a part of the charge was transferred to the other pixel by diffusion; again an error in the TOT measurement. We want to sort out such events and consider hits which are surrounded by non-counting pixels only (figure III.12).

The same spectrum as before (figure III.11 (b)) is shown on figure III.13 (b): The previous peaks be can distinguished clearly and two more peaks appear. The peaks can be identified as following:

- The first peak[2] is the 14.41 keV line of ^{57}Co as it is the source's γ-line with the lowest energy but still has branching ratio of 9.16 %. As the detection efficiency (the percentage of the total photon flux which is detected in the sensor) is almost 100 %, the line has to appear in the spectrum and be at the very left position.

1 For a detailed explanation of this effect see II.4.3.
2 What actually looks like the first peak is only a statistical artifact.

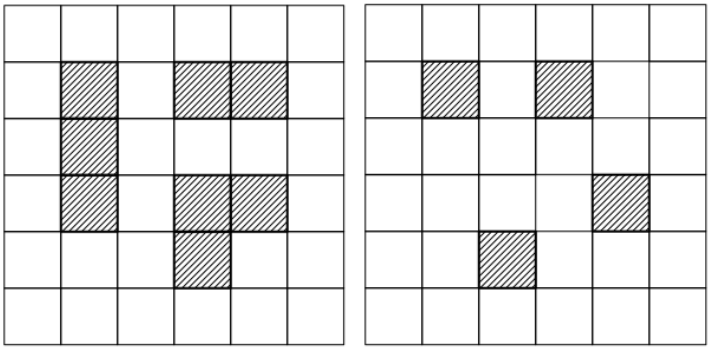

(a) **(b)**

Figure III.12: During the single clustering procedure only events as shown on picture (b) are considered and such events as shown on picture (a) are sorted out.

- The second peak is an overlay of the Cd and Te K_α- and K_β- fluorescence peaks, which are at 23.107 keV, 26.091 keV, 27.377 keV and 30.990 keV. They are too close to be resolved separately and form one peak altogether.
- The third peak is an overlay of eight Cd and Te escape peaks caused by 122.06 keV and 136.47 keV photons of ^{57}Co. Also in this case they cannot be resolved as the energy distances are too small.
- The fourth peak is mainly the 122.06 keV line of ^{57}Co. Although it has a branching ratio of 85.60 % the peak is even smaller than the 14.41 keV peak due to the lower detection efficiency at 122.06 keV (~38.3 %). Additionally, a significant part of the 122.06 keV photons is accumulated in the Cd and Te fluoresence peak and the escape peak. The 136.47 keV peak has a branching ratio of 10.68 % and a detection efficiency of 29.5 %. It is too small and merged with the broad 122.06 keV peak.

Actually, we identified the fourth and the first peak first since their position in the spectrum is very clear, and tested the possible assumptions for the second and the third peak by their correspondence with the calibration curve after obtaining it with other radiation sources.

Spectrum fitting The next step is to fit the spectrum to extract quantitative information out of it. As every peak is broadened with a Gaussian profile and therefore nearby peaks will affect each other, we did not fit every peak individually in a particular fit range but fitted the whole spectrum with a sum of Gaussian distributions of the form

$$N(TOT,\vec{\mu},\vec{\sigma},\vec{A}) = \sum_{i=1}^{n_p} A_i \exp\left(\frac{(TOT-\mu_i)^2}{2{\sigma_i}^2}\right), \tag{III.3}$$

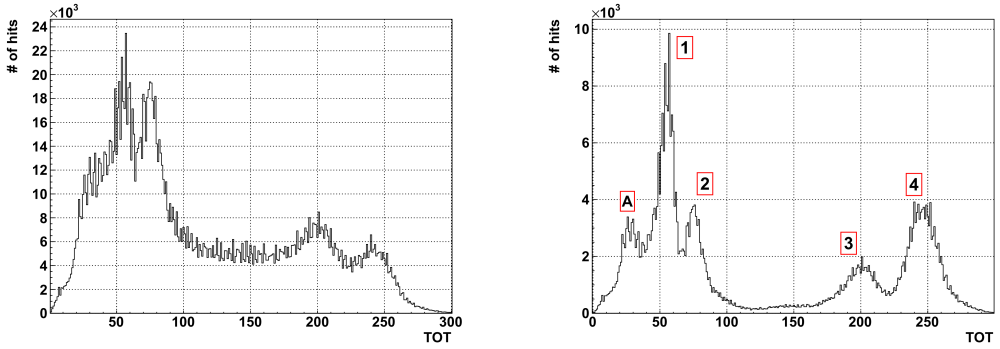

(a) before single clustering **(b)** after single clustering

Figure III.13: The TOT spectrum of ^{57}Co (a) before and (b) after single clustering: (A) statistical artifact; (1) 14.41 keV peak of ^{57}Co; (2) Cd and Te photo peaks; (3) Cd and Te escape peaks; (4) 122.06 keV and 136.47 keV peaks of ^{57}Co.

where N(TOT) is the number of hits for every TOT value and n_p the number of peaks in the spectrum. The initial values for the position and amplitude of each Gaussian are estimated by the following routine:

- Firstly, the TOT histogram is rebinned[1] with a factor between two and six, depending on the DAC settings and the distances between the individual peaks in the spectrum. The result and aim of this procedure can be seen on figure III.14: The big amount

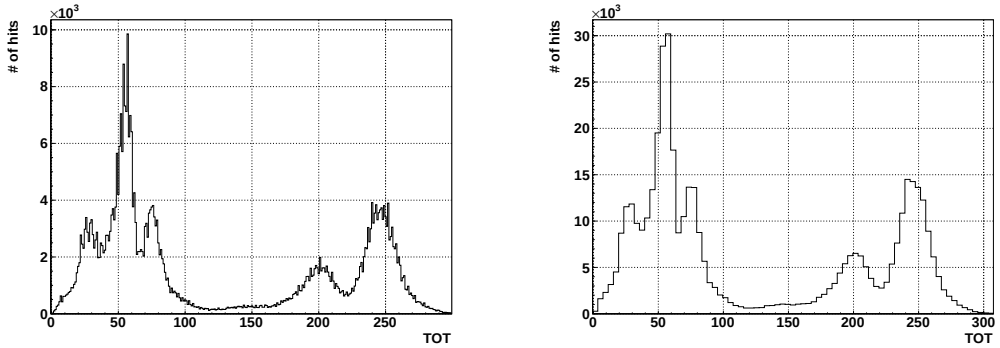

(a) before rebinning **(b)** after rebinning

Figure III.14: The single clustering TOT spectrum of ^{57}Co (a) before and (b) after rebinning.

1 Rebinning means, that the size of every histogram bin is increased by the rebinning factor. For instance, if the TOT histogram is rebinned by four, the bin size goes from one to four and all entries from the first four bins go into a common first bin, all entries from the fifth to the eighth bin go into a common second bin and so on.

of tiny peaks is eliminated and local maxima can be found by comparing the height of nearby bins.

- Now every bin is tested against N of its neighbours. We call N the test-distance and for proper results it has to be adjusted to the rebinning factor and the particular TOT spectrum. If a particular bin is the highest within the chosen test-distance it is nominated as a maximum.
- In the last step it is checked whether the height of the nominated bins exceeds a particular minimum value (threshold), which is normally a fraction of the height of the global maximum. Such a threshold has to be introduced to avoid artificial maxima which are not real maxima but can arise in regions of poor statistics.

The results of the fitting procedure are shown on figure III.15 (red). We could fit in a sum of five Gaussians into the TOT spectrum of ^{57}Co. If we compare it to the results of fitting each peak individually in a particular, reasonable range (blue), it can be noticed, that the differences of the means for the relevant peaks (the first and the last) are small and therefore the fitting of the sum is not stringently necessary. The numbers are given in table III.4. Note, that the whole procedure is done by a self-written program routine whose details are listed in the Appendix B. As for ^{241}Am and ^{57}Co the procedure is identical, we will refer to Appendix A at this point, where the results for all tested radiation and fluorescence sources are listed.

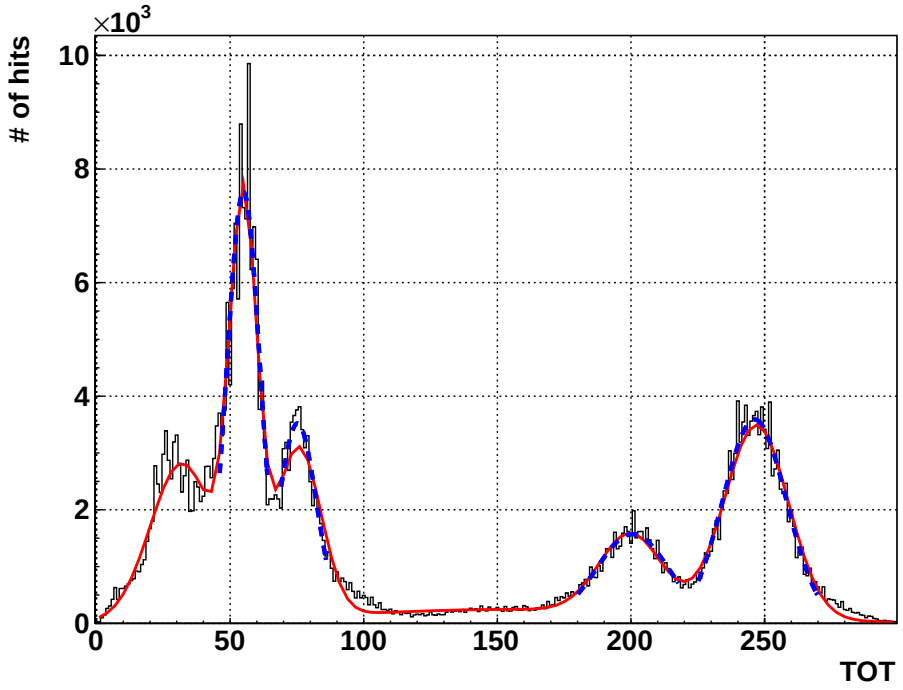

Figure III.15: The TOT spectrum of ^{57}Co fitted with a sum of five Gaussians (red) and single Gaussians, each in a particular region (blue).

Peak No.	μ red	σ red	μ blue	σ blue
1	55.142 ± 0.0338	3.613 ± 0.030	54.971 ± 0.025	6.118 ± 0.0319
2	75.602 ± 0.0672	8.382 ± 0.097	75.236 ± 0.059	7.053 ± 0.0747
3	210.998 ± 0.1680	35.168 ± 0.102	200.582 ± 0.091	13.673 ± 0.1245
4	248.057 ± 0.0455	9.737 ± 0.043	246.249 ± 0.043	11.865 ± 0.0496

Table III.4: The fit results for the TOT spectrum of ^{57}Co.

After ^{241}Am and ^{57}Co, we tested if the 661.5 keV Compton-backscattering peak of ^{137}Cs at 184.35 keV will be visible in a single clustering spectrum. Indeed, this is the case and this peak could be used for calibration. Since the detection efficiency at this energy is 13.7 %, a sufficiently long measurement run is required to gain enough statistics for calibration. Nevertheless it can be used to test the extrapolation reliablity of the calibration. This topic will be discussed later in this chapter. Our highest energy for calibration was 122.06 keV.

For the fluorescence lines we used the X-ray tube with different settings depending on the target material. The target properties can be found in Appendix A. After taking the data the evaluation procedure is the same as in the previous case of radioactive sources.

Sometimes there is only one peak in the spectrum (this is the case if the highest fluorescence energy of the target material is below the K-shell ionization energy of Cd or Te and the lower energy lines are below the THL) like in the spectrum of Mo (figure III.16 (a)). Therefore it belongs to on overlay of the K_α (E = 17.441 keV) and K_β (E = 19.605 keV) lines of Mo as these are too close to be resolved by the detector. If there are more peaks, these can be (additional to the K_α and K_β lines) fluorescence lines of Cd or Te, escape peaks or L_α and L_β lines of the target material like in the case of Pb (figure III.16 (b)). As stated above all measured TOT spectra and the identified peak positions can be found in Appendix A.

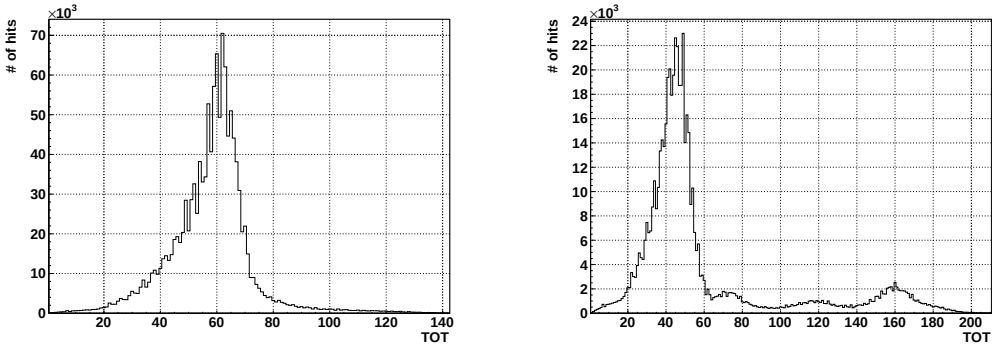

(a) Mo fluorescences **(b)** Pb fluorescences

Figure III.16: The single clustering TOT spectrum of (a) Mo and (b) Pb.

Fitting the calibration curve

The calibration curve is an interdependency between the TOT and the real energy measured in a pixel. Thus we want to insert the results of the identified peaks from all measured TOT spectra in a TOT versus energy graph and fit a curve to these points. We know the TOT value for the peak position as we obtained it from the measurement but we need to know the energy position as well. In a first approximation the weighted sum of all photon energies which contribute to one peak can be used although this is not the real deal. In fact, the quantity that is really measured is not the energy of the photons arriving at the detector but the energy deposited in one pixel. A part of the photon energy is always lost due to charge sharing, trapping [22] or various others effects. For every particular event it is impossible to take account of all possible effects that can occur in a calculation but we can estimate the deposited energy by using the ROSI simulation[1].

For all the radioactive and fluorescence materials we used for the measurements we simulated the experimental setup with ROSI. The result of the simulation is the energy response spectrum of the detector. On figure III.17 it is shown for ^{241}Am. We fitted the

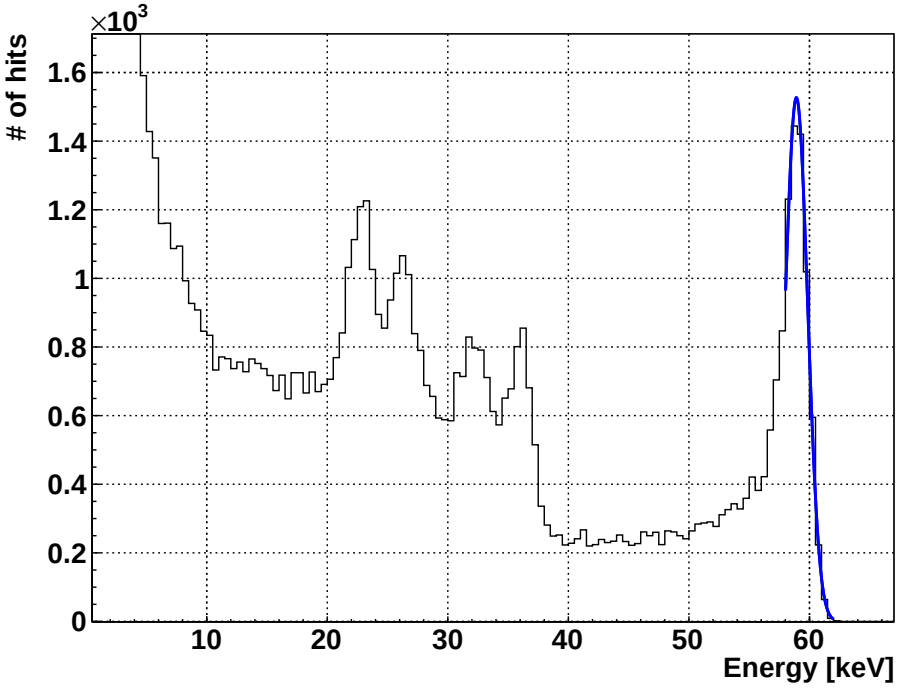

Figure III.17: The energy deposition spectrum that is measured by a Timepix detector simulated using ROSI.

1 See subsection 4.3 of the second chapter.

peaks in these spectra with Gaussian distributions of the form

$$N(E,\mu,\sigma,A_0) = A_0 \exp\left(\frac{(E-\mu)^2}{2\sigma^2}\right), \tag{III.4}$$

where N(E) is the number of hits for every energy value and used the mean of the fitting result for the energy position in the TOT versus E graph. The position of the presented peak is already shifted about 1 keV to the left compared to the photon energy and as for higher deposition energies more charge is usually lost within the sensor the shift increases with higher energies. The results for all radiation sources that we used in this work are given in Appendix A.

The results of the TOT and ROSI spectrum fitting are inserted in a TOT versus E graph and fitted by a function of the form [23]

$$TOT(E) = a \cdot E + b + \frac{c}{E-t}. \tag{III.5}$$

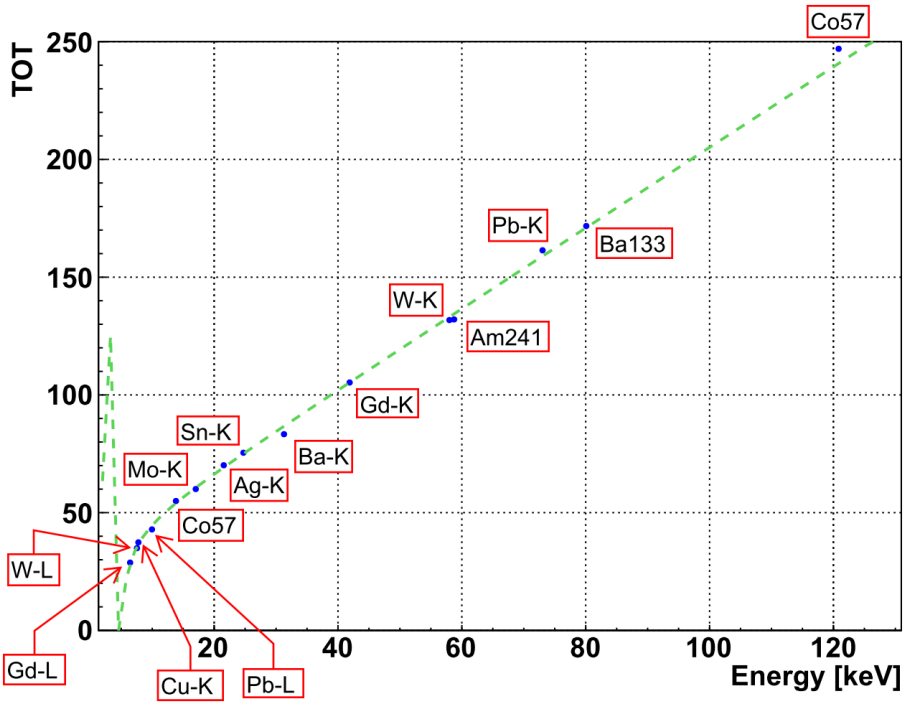

Figure III.18: The global calibration curve. The fit function is $TOT(E) = a \cdot E + b + \frac{c}{E-t}$ with a $= 1.70548 \pm 3.820 \cdot 10^{-4}$ $\frac{1}{keV}$, b $= 35.0445 \pm 2.1993 \cdot 10^{-2}$ keV, c $= 46.0468 \pm 0.2911$ keV, t $= 3.8117 \pm 1.8455 \cdot 10^{-2}$ keV.

The result for the global calibration is shown on figure III.18. We used Cu, Mo, Gd, Ag, Sn, Ba, W, ^{241}Am, Pb, ^{133}Ba and ^{57}Co for the global calibration. The error bars are the fitting errors for the means of the Gaussians of the spectrum fitting. For the fitting we fixed t in interval [3; 7]. This prevents fitting errors and effectively t is in this range in most cases (see [23]). The fitting results were with $a = 1.70548 \pm 3.820 \cdot 10^{-4}\ \frac{1}{keV}$, $b = 35.0445 \pm 2.1993 \cdot 10^{-2}$ keV, $c = 46.0468 \pm 0.2911$ keV, $t = 3.8117 \pm 1.8455 \cdot 10^{-2}$ keV. According to the calibration the energy limit for the detector is at 4.751 ± 0.021 keV.

This curve can be used to reconstruct the real energy spectrum, which is shown for ^{57}Co on figure III.19. The 14.41 keV and 122.06 keV peaks are reconstructed at the almost right positions, but slightly shifted. This behaviour can be observed for all peaks in all measured spectra. The reason for this are the differences between the pixels which are neglected in the global calibration. To correct this shift and improve the energy reconstruction quality the calibration process can be done for each pixel individually which is discussed in the next section.

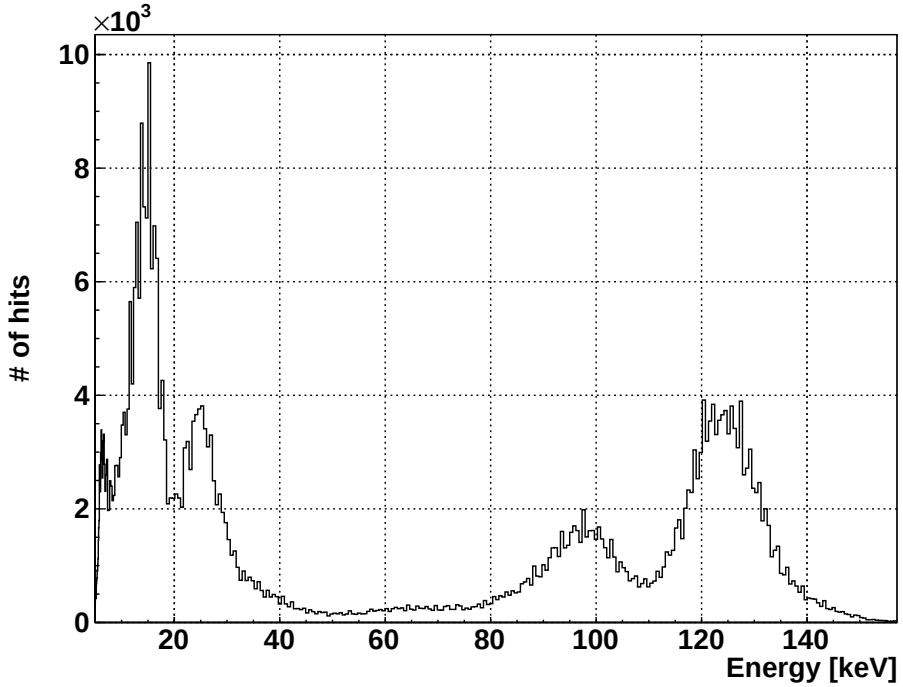

Figure III.19: The reconstructed energy spectrum of ^{57}Co with the global calibration. The peak at 122.6 keV is shifted by 4.01 keV to the right (compared to the position predicted by ROSI).

III.3.2 Pixel-by-pixel calibration

As all the pixels are not equal but have differences due to the fabrication, the parameters of the calibration curve have to be determined for every pixel to ensure an optimal energy reconstruction performance. Since the idea of the calibration procedure stays the same and is detailed described in the previous section, in this subsection we will mainly discuss the details of the calibration automatization (as the calibration has to be performed for every pixel).

Automatic spectrum fitting

For the pixel-by-pixel calibration, it is necessary to evaluate the TOT spectra for every pixel, i.e. we need to evaluate $128 \cdot 128 = 16384$ similar spectra. Of course, this number is too large to evaluate every spectrum manually. Therefore we used the following automatic procedure to perform this task[1]:

1. The first step is to cut off the part of the spectrum which does not belong to the peak that we want to fit. For the cutting the spectrum is divided by a cutting point p_c in two parts - a left and right one; and the part which does not contain the peak is cut away. Then around the highest bin of the remaining spectrum (which is close to the peak position) everything is cut away which is outside of a particular radius r_c. Before the cut the average peak positions and peak width have to be estimated roughly by hand to give the procedure a reasonable cutting point p_c and cutting radius r_c. Since the peak positions vary a lot between different pixels (figure III.20), the estimation has to be done to ensure that the cutting parameters are set in such a way that the desirable peak is never cut away. The cutting is important to ensure that the fit is performed for the right peak even if statistics is not the best[2]. The step is shown for the ^{57}Co TOT spectrum of pixel 23453 on figure III.21 before (a) and after (b) the cut for the 122.06 keV peak.
2. In the next step the peak is fitted with a Gaussian distribution G(TOT,A,μ,σ). The initial fit values for the mean μ and the amplitude A are the position and the bin value of the maximum bin in the cut distribution. The initial width σ for all peaks is manually estimated roughly, beforehand.
3. Sometimes the fit can fail because of a particularly misplaced distribution of the hits. This can be identified by a big fit error and in this case, a second fit is performed with the log likelyhood method, which is more robust to statistical fluctuations. Although this step may seem redundant, we want to state that this step can increase the fit routine reliability enormously, especially in case of bad statistics.

1 The procedure is performed by a self-written software tool. Some details for the usage are given in Appendix B.

2 The numbers for the statistics that we used in this calibration are given later.

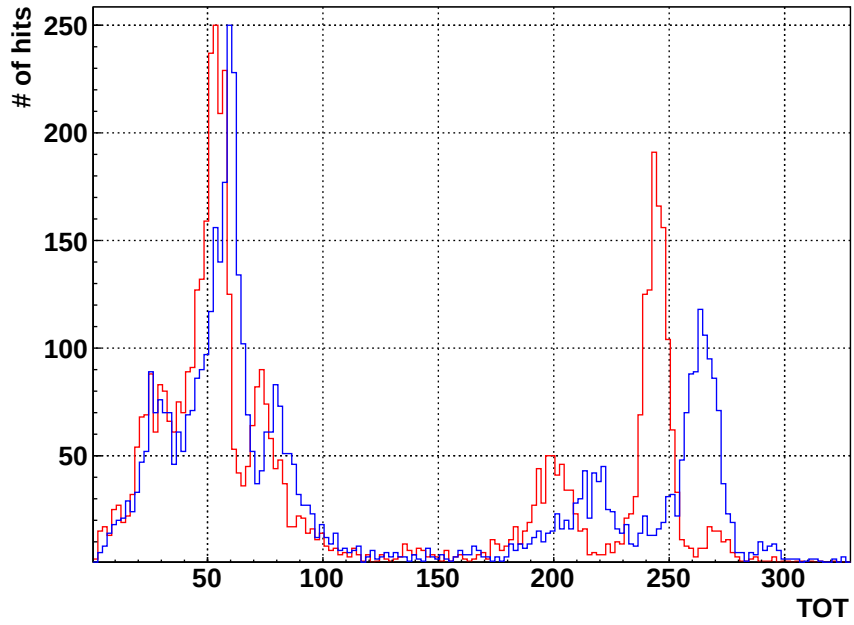

Figure III.20: The ^{57}Co TOT spectra for pixel number 23453 (red) and 23459 (blue). The distance between the 122.06 keV peaks is about 20 TOT clock ticks.

4. The last step is a second fit with a Gaussian distribution. Now the initial fit values are the mean, the amplitude and the width of the Gaussian in the previous step. The fit range is now limited to the interval $[\mu - 1.8 \cdot \sigma;\ \mu + 1.8 \cdot \sigma]$. Both fits are shown on figure III.22. The second fit is necessary as the first fit gives often results which are too wide.

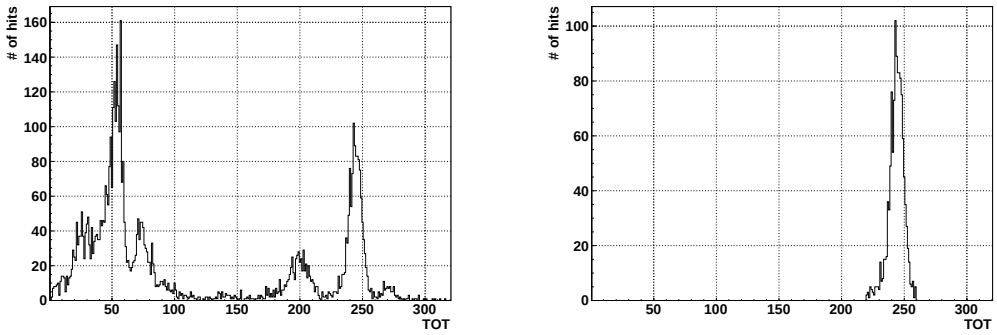

(a) before cutting **(b)** after cutting

Figure III.21: The 122.06 keV peak in the ^{57}Co TOT spectrum of pixel number23543 (a) before and (b) after the cutting procedure.

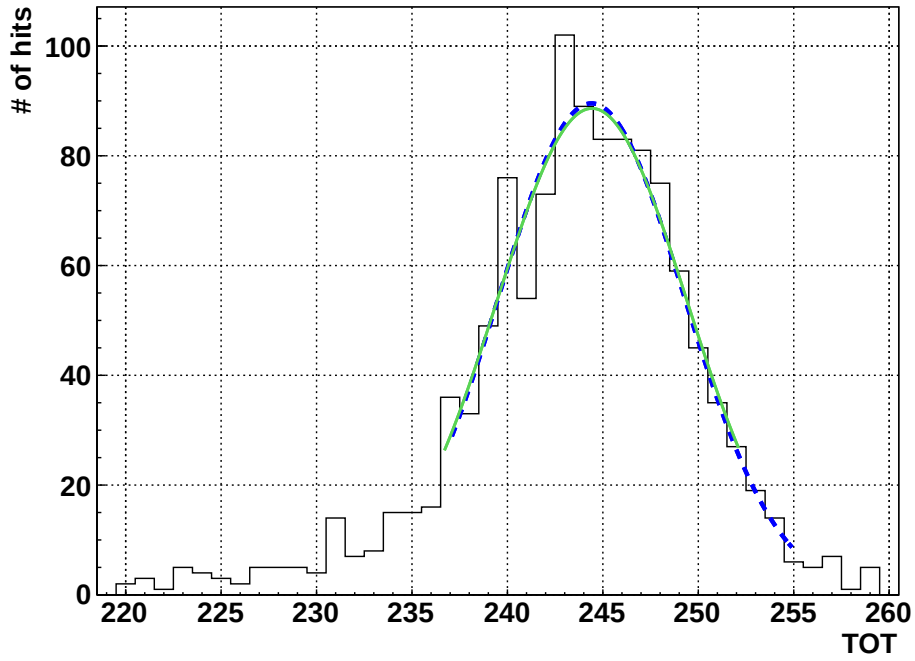

Figure III.22: The 122.06 keV peak in the ^{57}Co TOT spectrum of pixel number 23543 fitted. The first fit is blue. The second fit, limited to the $[\mu - 1.8 \cdot \sigma;\ \mu + 1.8 \cdot \sigma]$ interval, is green.

Sometimes the fit can fail either because the pixel is defect or due to some statistical misfortune. It is important to identify these cases and save them. For actual useful spectra of good pixels, where the fit went wrong, the peaks can be refitted (or the mistakes can be fixed during the calibration curve fitting) but bad pixels have to be sorted out for further measurements. For this task we used two methods. The first is to use the following quantity for the "fitting error":

$$L^{2W}[f] = \sqrt{\frac{1}{a-b}\int_b^a \frac{(f(x)-h(x))^2}{h(x)}\mathrm{d}x}, \tag{III.6}$$

where f(x) is the resulting fit function and h(x) the distribution that has to be fitted in the interval [a; b]. The idea of this measure is that the smaller relative errors of the fit function and the distribution at every point are, the better the fit is (see figure III.23). In the case of discrete points or histograms the integral has to replaced by a sum over all points (bins) x_i, i = 1,..,N.

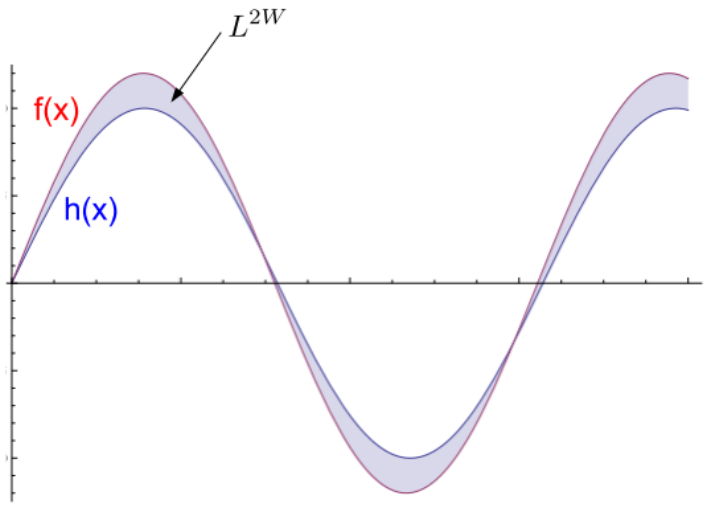

Figure III.23: Blue is the distribution h(x) which is to be fitted and red the fit fuction f(x). The light blue marked space between the curves is the descriptive meaning of the L^{2W} error measurement.

$$L_{dis}^{2W}[f] = \sqrt{\frac{1}{N}\sum_{i=1}^{N}\frac{(f(x_i)-h(x_i))^2}{h(x_i)}} \tag{III.7}$$

The number of counts in every TOT bin is Poisson distributed. Therefore $h(x_i) = {\sigma_P}^2(x_i)$, where σ_P is the width of the distribution. In other words, we are summing up the deviations from the Poisson distribution normalized to the width. If we call this quantity

$$\eta(x_i) = \frac{f(x_i)-h(x_i)}{\sigma_P(x_i)}, \tag{III.8}$$

then we know that η is a Gaussian distributed around 0 with $\sigma_\eta = 1$. These properties can be used to calculate the best value that L_{dis}^{2W}[f] can have for a particular fit function f, namely the value of L_{dis}^{2W} at which f is really the "envelope" of a Poisson distributed process. In this case L^{2W} will have the value

$$L_{opt}^{2W} = \sqrt{\frac{\int_{-\infty}^{\infty}\eta^2\exp\left(\frac{\eta^2}{2\cdot 1^2}\right)\mathrm{d}\eta}{\int_{-\infty}^{\infty}\exp\left(\frac{\eta^2}{2\cdot 1^2}\right)\mathrm{d}\eta}} \tag{III.9}$$

$$= 1 \tag{III.10}$$

The integral in the numerator is equal to the value of the sum in the case of an ideal fit and the denominator corresponds to the normalization N. The fit quality L_{dis}^{2W} for every pixel can be estimated and compared with this quantity. If it is above a particular value,

fits will be marked as "bad". This value has to be estimated manually for every radiative source. The second method is to mark fits as bad if the fit results are just not reasonable at all ($\mu < 0$, $\sigma \approx 0$, or $\mu >$ highest TOT value in the spectrum, or σ too large).

Automatic calibration curve fitting

For most of the pixels (98.4 %) the spectra fitting will work without any problems if a minimum level of statistics is guaranteed (at least 200 hits in the peak which has to be fitted); however, if the pixel is not completely defect but some measurement or some fitting process was unlucky, usually you can observe the following scenario: Most of the results from the automatical spectrum fitting give good points in the TOT versus E plot (to fit the calibration curve to them) but for one of the points something went wrong (for whatever reasons) and the point is totally off (figure III.24 (a)). In this case the mean of the fitting position distribution for a particular peak can be used but at this point with a 2σ error bar to have a correct error measure (figure III.24 (b)). Now the calibration curve can be fitted without any problems[1].

If this scenario occurs for points at low energies, or rather, TOT, the curve can sometimes flip (figure III.25 (a)) because of the large error bars. This problem can be overcome by changing the sign of c after the fitting and performing a second fit for the linear part to correct the a and b values (figure III.25 (b)). Of course, this will produce small errors but is still way better than having no calibration points at the lower edge at all or using the global calibration result for low TOT.

For the fitting quality control we used the sum of all relative fitting errors

$$\Delta_\Sigma = |\Delta_a| + |\Delta_b| + |\Delta_c| + |\Delta_t| \tag{III.11}$$

and masked all pixels above a certain threshold value for Δ_Σ to check them manually. By this procedure a meaningful calibration could be achieved for almost all (99.7 %) pixels.

1 At this point we want to mention that it is better to have a value with a high error bar for the fitting than completely ignoring the point. If you start ignoring points, at some point the automatic fitting will break down completely (simply due to a lack of fitting data) since the number of calibration points is limited.

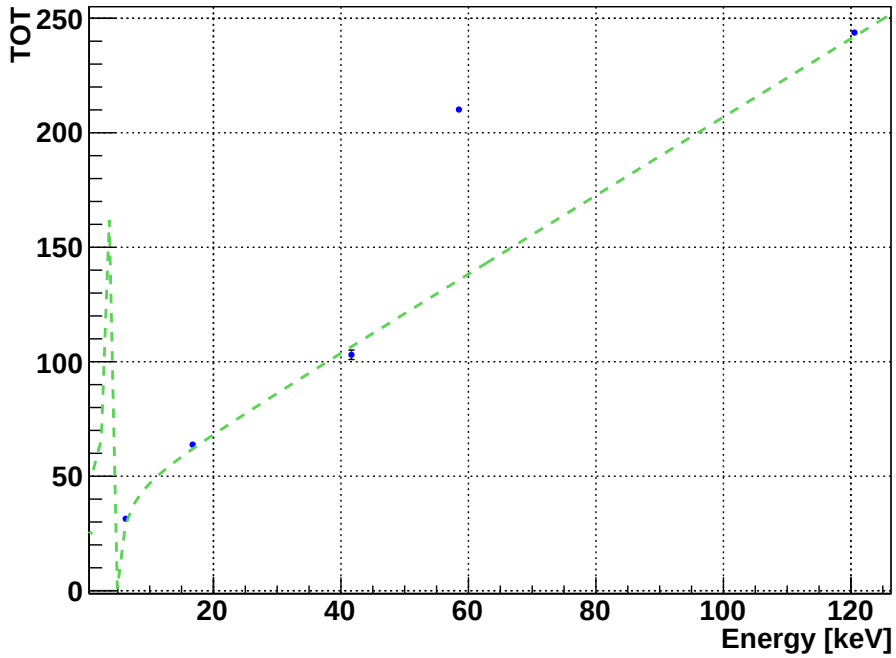

(a) before correction

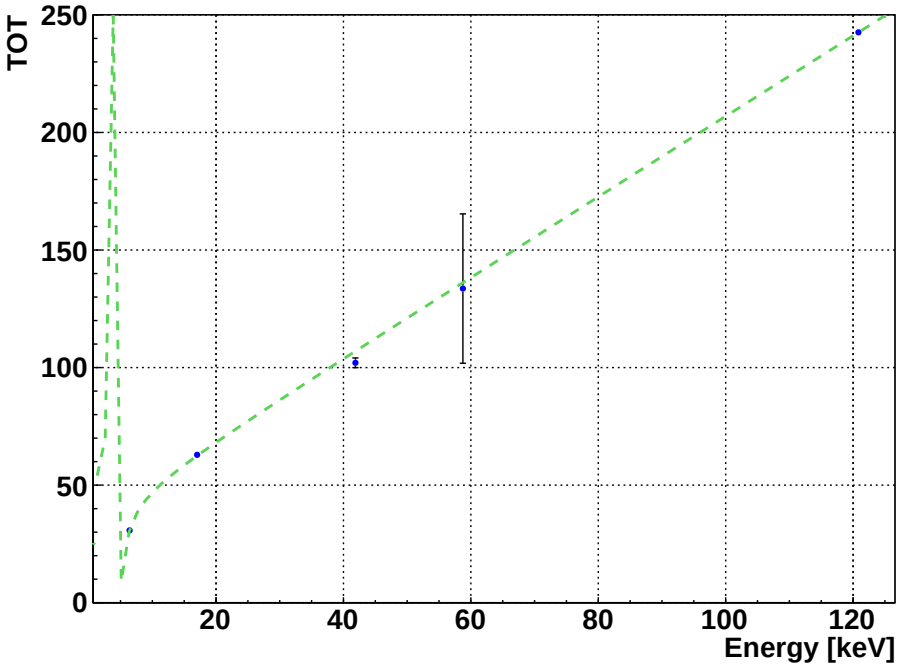

(b) after correction

Figure III.24: The calibration curve for pixel number 6135 (a) before (the point at 59.54 keV is totally off) and (b) after the correction.

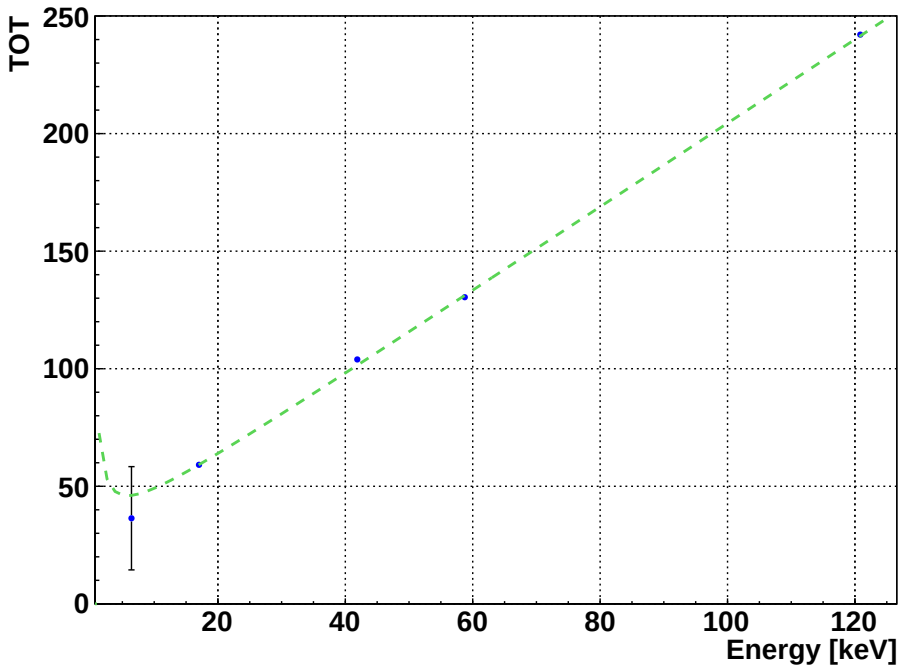

(a) before correction

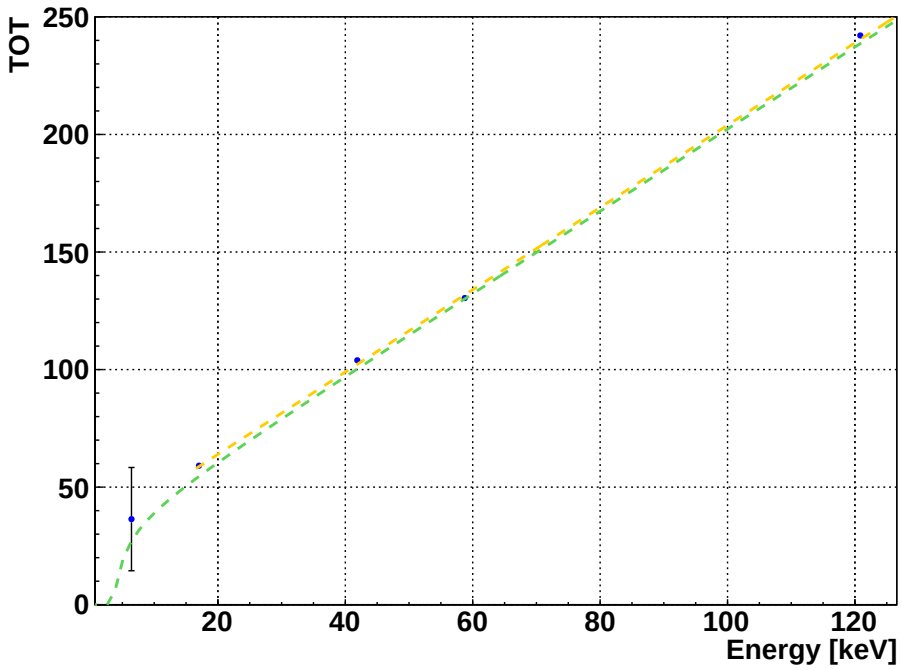

(b) after correction

Figure III.25: The calibration curve with bad fitting at low energies (a) before and (b) after the flipping. The yellow line is an additional fit for the linear part to obtain more reliable values for a and b.

Experimental data

For the pixel-by-pixel calibration that was performed in this work, we used five points: Gd L-lines mixture (6.43 keV), Mo K-lines mixture (17.03 keV), Gd K-lines mixture (41.88 keV), the ^{241}Am 59.54 keV decay line and the ^{57}Co 122.06 keV decay line. We had about 90 - 600 counts in the peaks (depending on the spectrum and pixel). The time which is required to perform the fitting for one peak and 16384 pixels is roughly about 20 minutes. The time which is required to perform the fitting for the calibration curve of 16384 pixels is about 40 minutes.

Apparently the number of "bad" fits decreases with increasing amount of counts in a peak but a quantitative interdependency could hardly be established and is therefore not discussed here. The reconstructed energy spectrum of ^{57}Co is shown on figure III.26. The spectrum is now obtained by calculating the spectrum for every pixel and then summing up all spectra. This is what is plotted on figure III.26 and meant if we speak of reconstructing the spectrum pixel-by-pixel. Now the 122.06 keV peak is at its right position and the 136.47 keV peak can be resolved. A detailed discussion on the energy resolution is given in the next section.

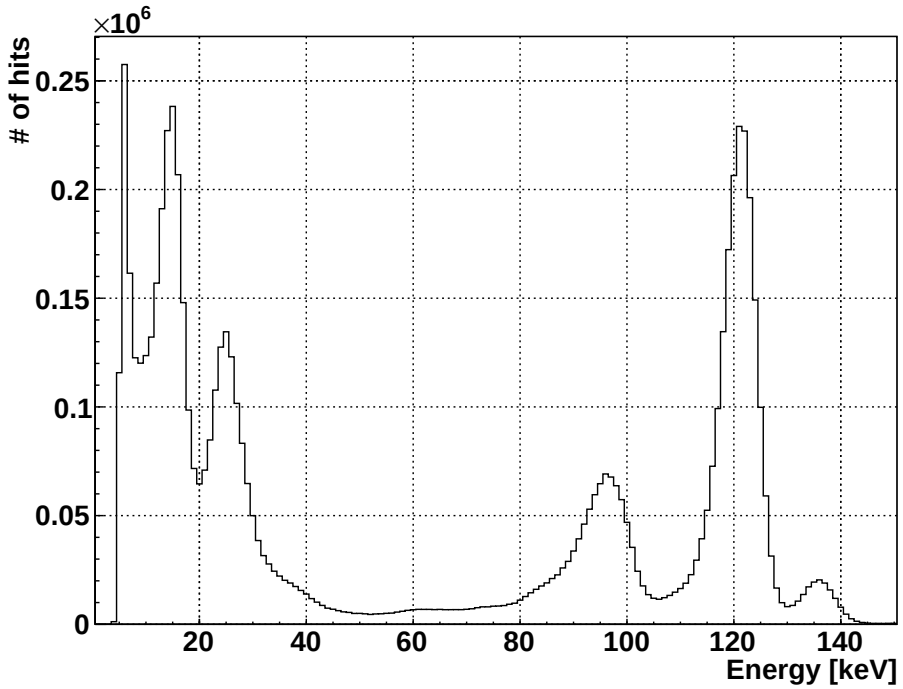

Figure III.26: The energy spectrum of ^{57}Co with the pixel-by-pixel calibration.

III.3.3 Calibration curve reliability

A major issue concerning the calibration is its reliability. It can be tested comparing the peak positions in the measured spectra to their expected positions (see figure III.27). We will call this quantity the calibration error ΔS. To do this correctly, we have to estimate the expected positions by the ROSI simulations. This is nessecary because the photon energy and the real measured energy are not the same due to charge losses and other undesirable effects within the sensor material. You can see $\frac{|\Delta S(E)|}{E}$ on figure III.28 for peak energies within the range of the calibration [6.432 keV; 120.84 keV]. We can see that the deviations are about 5 % for points in the non-linear and near to the non-linear part of the calibration curve. In the linear part the deviations are normally smaller than 1%.

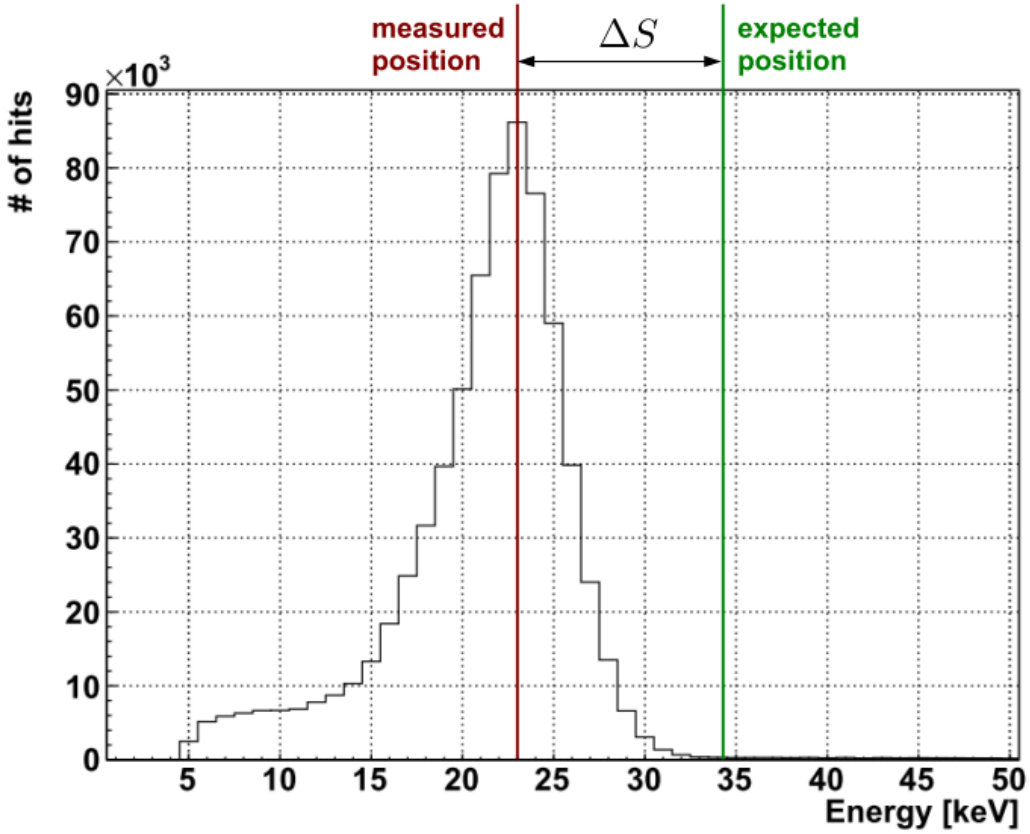

Figure III.27: Definition of the quantity ΔS: The difference between the measured and expected position of a peak after calculating the energy spectrum with the calibration curve.

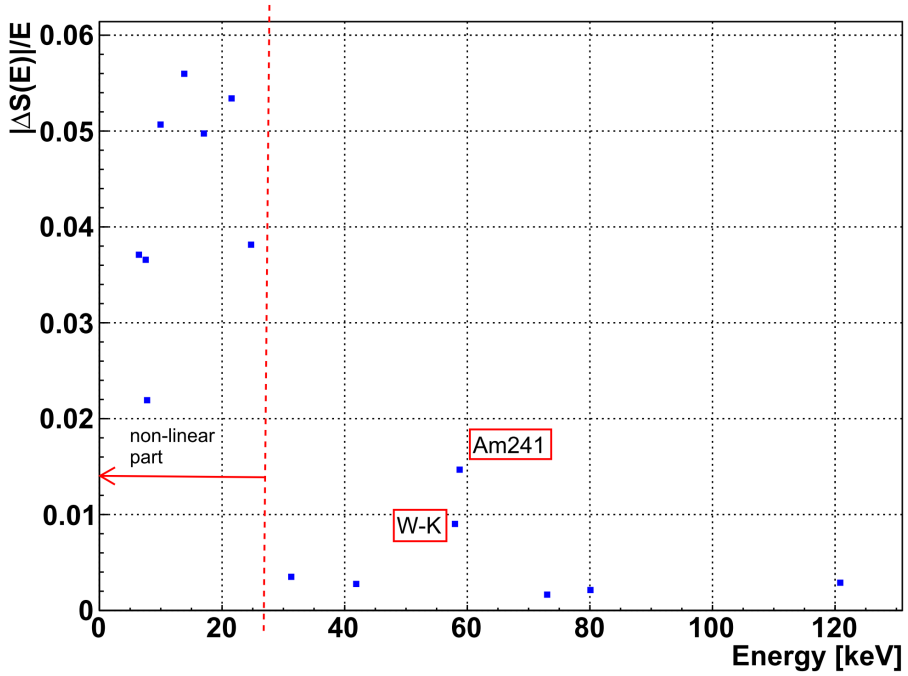

Figure III.28: The determined value of $\frac{|\Delta S(E)|}{E}$ for peaks in the energy interval [6 keV; 125 keV]. The $\frac{|\Delta S(E)|}{E}$ value for the peaks at 59 keV is surprisingly high.

A strange exception is ^{241}Am. Its error is significantly larger than the error of all the peaks around it. Indeed, if you go back and take a closer look at either the global calibration curve III.18 or one of the calibration curves for a particular pixel, you will see that the ^{241}Am point is always below the calibration curve. There is a systematic error suggesting that either there is something special, unpredictable about ^{241}Am (which was not analyzed in detail due to the lack of time) or the calibration curve has some strange unexpected behaviour at about 59 keV. Some evidence for this hypothesis is that the tungsten fluorescence peak at 57.99 keV is almost perfect on the calibration curve but the ^{241}Am peak is not.

As next we analyzed the distribution of the deviations over the matrix for ^{241}Am. On figure III.29 the ΔS value for every pixel of the matrix is shown. You can see that ΔS is distributed homogeneously over the matrix expect for some clusters (orange) which can be identified as Tellurium inclusions (impurities) within the CdTe. In this regions the pixels do not work properly and therefore no reasonable calibration could be performed. Consequently, such an analysis can provide a useful method to identify impurities in the sensor layer. The upper edge and the right edge are orange because no ΔS value was calculated for them as for most of them the calibration procedure failed.

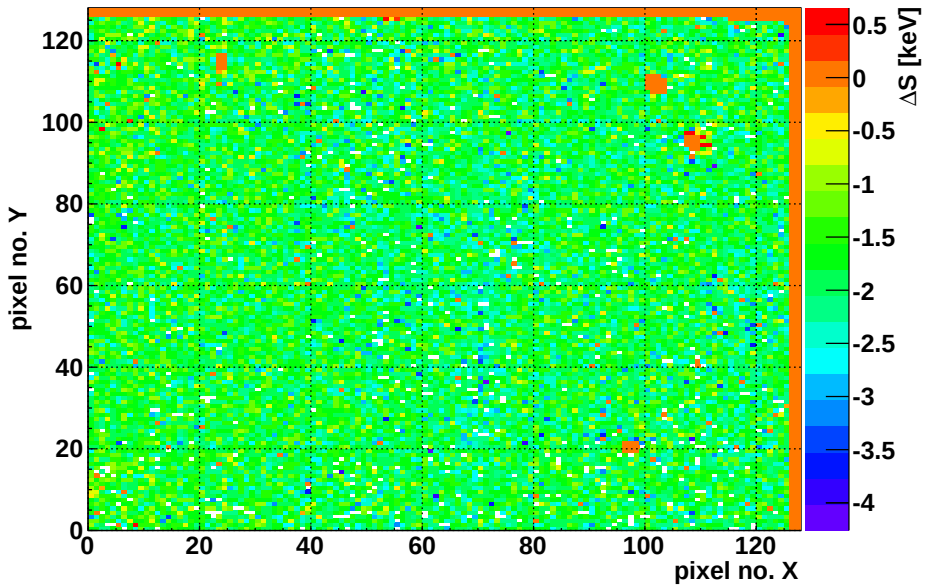

Figure III.29: The distribution of ΔS across the matrix for the 59.54 keV peak of ^{241}Am. It is relatively homogeneously distributed despite point at which Tellurium inclusions occur (orange blobs).

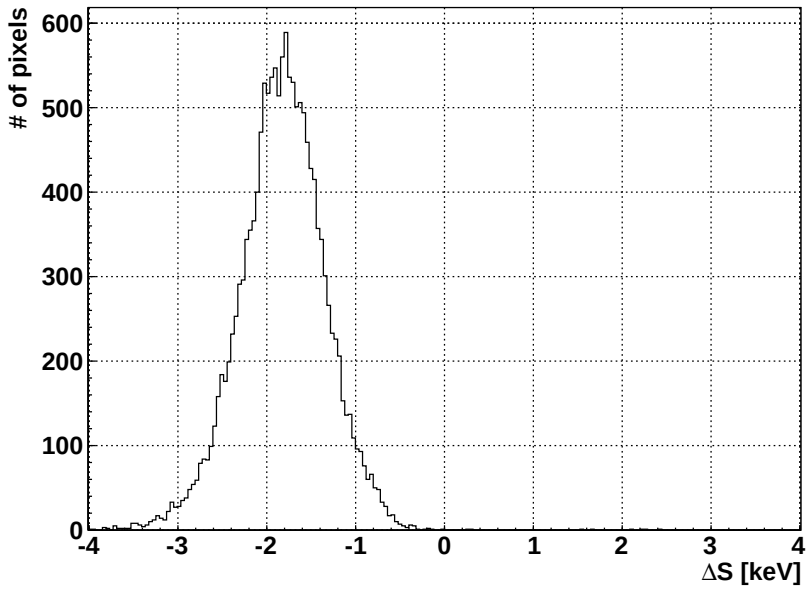

Figure III.30: The distribution of ΔS of the ^{241}Am measurement plotted for all pixels. It is (almost) a Gaussian distribution around -1.88 keV.

If we plot ΔS versus the number of pixels for ^{241}Am, a Gaussian distribution around about -1.88 keV is the result (see figure III.30). In the case of a perfect calibration we would expect a sharp distribution centered at 0 keV. Therefore errors in the calibration provide another source for peak broadening and limit the energy resolution. We will discuss this effect in the energy resolution sections.

Of big importance for our forthcoming purposes is to check if the curve is reliable above the calibration range, i.e. on extrapolation. We performed this task by fitting several peaks from the ^{57}Co, ^{137}Cs, ^{133}Ba and ^{232}Th (122.06 keV, 136.47 keV, 184.35 keV, 238.63 keV and 356.02 keV) spectra and comparing them again to the ROSI estimated values. The result is shown on figure III.31. We can see a clear trend: The energy is always too high. The reason is probably the empirical calibration function which is assumed to be linear for all energies above 20 keV. This approximation works within the calibration range but does not hold if you extrapolate to higher energies.

In a first approximation this error can be faced by a linear correction function c(E) = aE + b fitted to the points in the ΔS plot. After the correction the peaks are much closer to their expected positions. We will see how important the correction is in the next chapter when peak energies at the 1 MeV scale and energy depositions per pixel higher than 300 keV are considered.

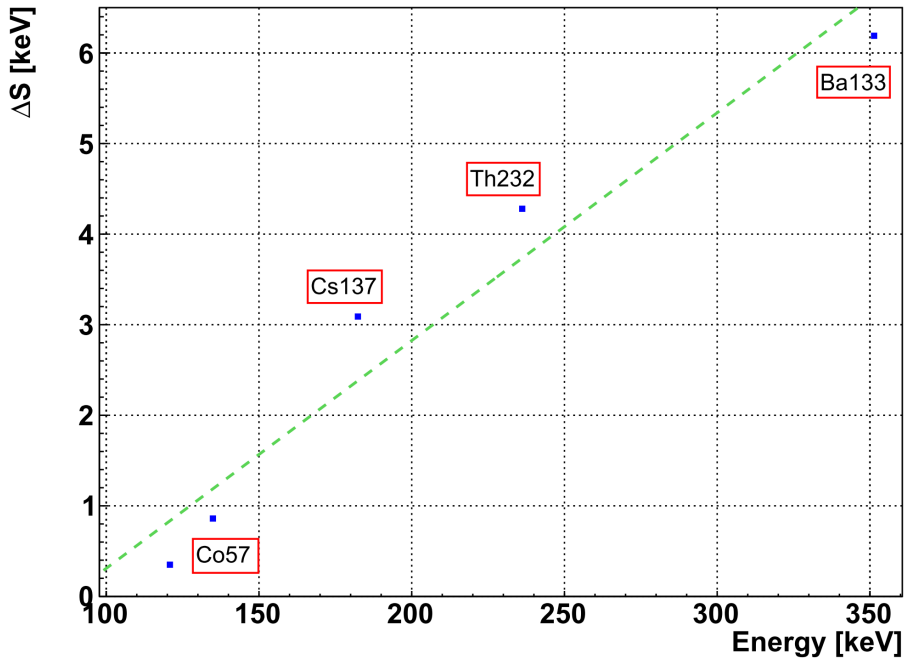

Figure III.31: ΔS for peaks above the calibration range and the linear correction line. The parameters of the curve c(x) = a·E + b are a = 0.0350±0.0183 and b = −3.761±1.064 keV.

III.4 Energy resolution for single pixel hits

After the calibration is performed and the energy spectra can be reconstructed, it is interesting to investigate the energy resolution $\frac{\sigma}{E}$ of the detector. This is done by fitting particular peaks in the single clustering spectra with a Gaussian distribution N(E,A,μ,σ) and calculating the ratio from the fit results. Again, single clustering means that only such pixels are taken into account which have no counting neighbours. Therefore here we investigate the energy resolution in the particular case that the whole deposited energy is counted in one pixel only. On figure III.32 the energy resolution for the global calibration with DAC values according to table III.3 (IKrum 10, PreAmp 210, THL 190) is shown. The radioactive sources are shown in blue, the fluorescences are shown in red.

In the table of Appendix A the energy resolution is given for all materials appearing on figure III.32. From the plot you can observe, that the energy resolution of fluorescences is always worse than the energy resolution of radioactive sources. This is due to the fact that the fluorescence peaks are usually an overlay of several K and L lines, which cannot be resolved, whereas the radioactive lines consist normally only of one or two major neighbour lines and therefore only they give us a reliable energy resolution value for single hits. Thus, we used only them to determine the energy resolution as a function of energy.

We assumed an interdependency of the form

$$\frac{\sigma}{E}(E) = \alpha + \frac{\beta}{(E-\gamma)^{\delta}} \tag{III.12}$$

between the energy resolution $\frac{\sigma}{E}$ and the energy E for several reasons: Firstly, if σ would not depend on the energy but be a constant, the interdependency would simply be

$$\frac{\sigma}{E}(E) = \frac{\beta}{E}, \tag{III.13}$$

where β is a constant and to be determined from the measurement. But for a real detector the resolution cannot be arbitrary good and has always a lower limit. Therefore the limit $\lim_{E\to\infty} \frac{\sigma}{E}(E)$ must not be zero but a certain value α what gives us

$$\frac{\sigma}{E}(E) = \frac{\beta}{E} + \alpha. \tag{III.14}$$

Now we know that the energy cannot be measured down to 0 eV but only down to a particular threshold value γ and therefore the curve has to be shifted to the right as otherwise we would predict an non existing energy resolution between 0 eV and γ.

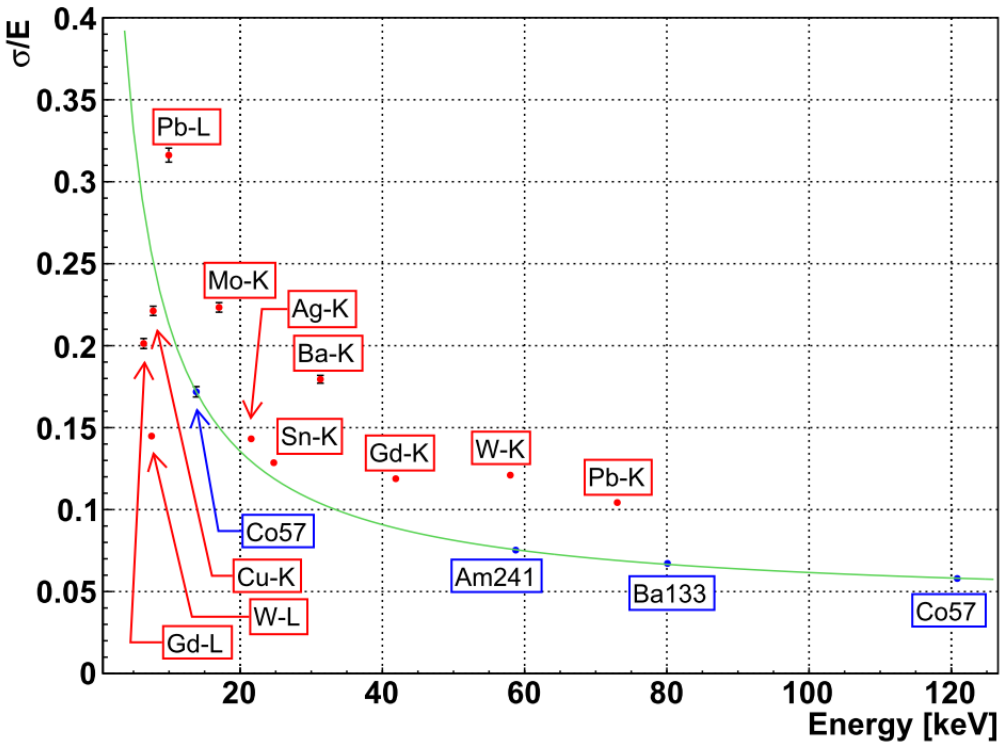

Figure III.32: The dependency of the energy resolution $\frac{\sigma}{E}(E)$ on the energy E. The fitted function is $\frac{\sigma}{E}(E) = \alpha + \frac{\beta}{(E-\gamma)^\delta}$ with $\alpha = 0.04084 \pm 0.00245$, $\beta = 2.101 \pm 0.245$, $\gamma = 2.2379 \pm 1.6863$ and $\delta = 1$.

Additionally it is more general to assume that σ is not constant, but depends on the energy power-law-like:

$$\sigma(E) = E^p, \tag{III.15}$$

where p is a constant exponent. All arguments combined bring us to the final fit formula for the energy resolution:

$$\frac{\sigma}{E}(E) = \alpha + \frac{\beta}{(E-\gamma)^\delta}. \tag{III.16}$$

Fitting of experimental data shows that δ is always at a value of about ~0.98. Hence, we will set it to 1 for simplicity in our further investigations. Indeed, as you can see on figure III.32, the fit function and the data are in very good agreement. Therefore the described fit function can be used for practical purposes but in fact it is rather empirical and would need a more solid theoretical foundation, or rather, derivation. The energy resolution

limit for the global calibration (and the particular DAC settings we used) is

$$\alpha = 4.109\ \%. \tag{III.17}$$

III.4.1 Differences between global and pixel-by-pixel calibration

The energy resolution can be increased dramatically by the pixel-by-pixel calibration. The reason for this is that the TOT spectra measured by each pixel can vary a lot. This was illustrated in a previous section on figure III.20 for two pixels with the TOT spectrum of ^{57}Co. The 122.06 keV appears at 249 TOT for the blue and at 230 TOT for the red curve. In a global calibration, practically, you would change the numbers below the x-axis but the spectra would still maintain their shape and if you sum up all the spectra, the peak is broadened by the shift range of the peaks. The shift range, which is the difference between the mean of the largest and the lowest TOT peak position, can be up to $7\sigma_{TOT}$. σ_{TOT} is the width of the peaks in the TOT spectrum fitted with a Gaussian distribution. The enhancement can be clearly seen on figure III.33. Figure (a) shows the energy spectrum of Pb with the global and (b) with the pixel-by-pixel calibration. In the first case the K_α- and K_β-fluorescence lines are merged whereas in the second case they can be distinguished.

On Figure III.34 the energy resolution for the global calibration (blue) and the pixel-by-pixel calibration (red) are shown in comparison. The brown points in the curve are the results of the ROSI simulation which takes into account the physics within the sensor layer but neglects the noise within the electronics. Although the ROSI simulation can take this noise into account we did not include it into the simulation to compare our experimental data results to the very limits that are given by the physics of the sensor only.

Let's consider the low energy peaks (E $<$ 15 keV) first. Here the energy resolution can be even better with the global calibration since it is primary limited by the physics in the sensor and only secondly by the calibration mistakes. Additionally, the global calibration was slightly better since we used more calibration points at low energies for the global calibration. The energy resolution in the simulation increases much faster since it does not take into account calibration mistakes and TOT variations which are high at low energies. It drops below 5 % at about 20 keV and almost reaches the plateau at about 60 keV whereas for the experimental data the decrease is much slower.

From 20 keV on the advantage of the pixel-by-pixel calibration can clearly be seen: The energy resolution is almost a factor of 2 better for the pixel-by-pixel calibration compared to the global calibration. A special point is at the Pb K-fluorescence line where the K_α- and K_β-fluorescence lines can be distinguished in pixel-by-pixel calibration but not in the global calibration case and therefore the resolution increases dramatically.

In the limit of very high energies the energy resolution can drop down to $\alpha = 4.1$ % for the global calibration whereas it is a factor of about 4 better in the pixel-by-pixel case and reaches a value of $\alpha = 1.01$ %. However, the theoretical value of $\alpha = 0.54$ % which is proposed by the simulation is not reached for the pixel-by-pixel calibration as well.

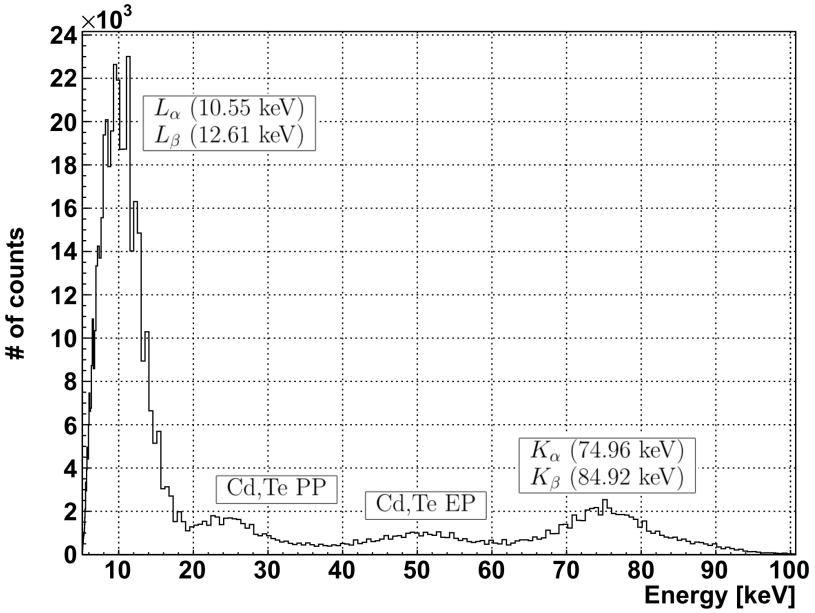

(a) global calibration

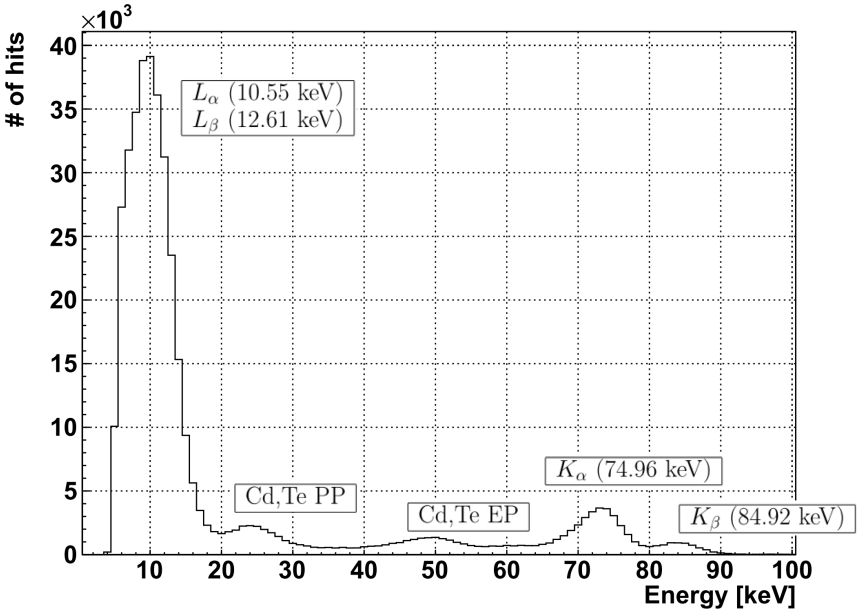

(b) pixel-by-pixel calibration

Figure III.33: The same spectrum of Pb fluorescence lines with a global calibration (a) and a pixel-by-pixel calibration (b). The K_α and K_β lines are distinguishable in the case of the pixel-by-pixel calibration, but not for the global calibration.

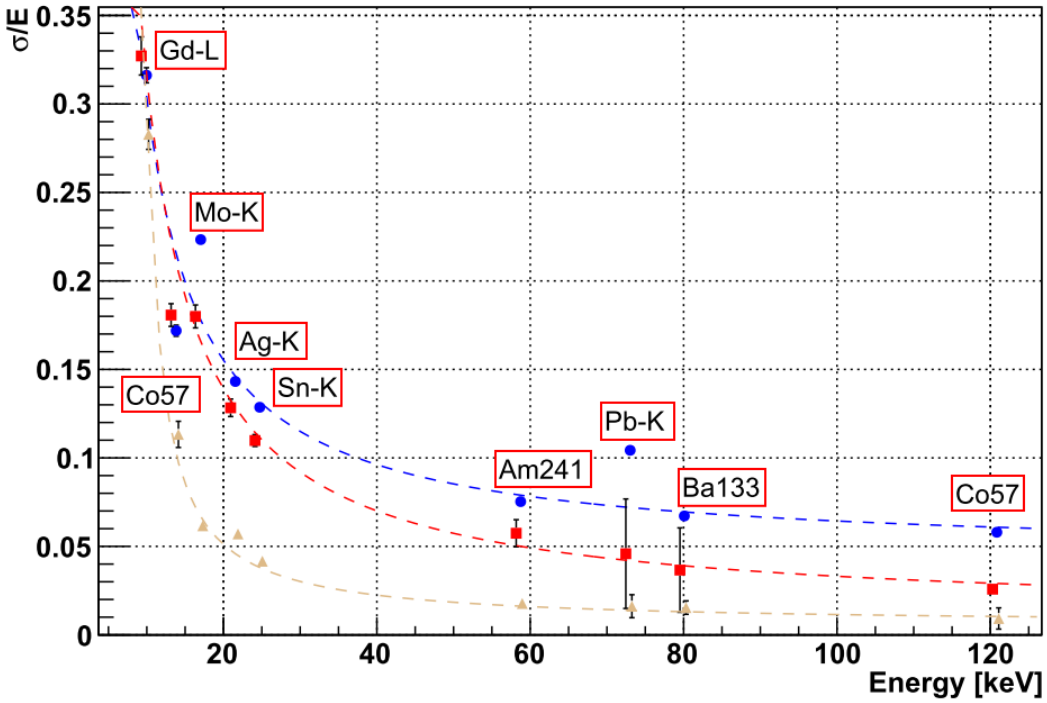

Figure III.34: The energy resolution for various fluorescence peaks; (blue) with global calibration, (red) with pixel-by-pixel calibration, (brown) ROSI simulation data.

III.4.2 Dependence of the energy resolution on working parameters

As the shape of the voltage pulse after integration is sensitive on the DAC values (see II.4.2.), they have an influence on the energy resolution of the detector. The energy resolution should be affected by the IKrum (which affects the length of the pulse during the decharging process) and the THL. Therefore we investigated the dependence on these two parameters. Another important parameter to investigate is the bias voltage as the charge sharing effect, which is one of the major reasons for the decline in the energy resolution, is strongly affected by this quantity. We used ^{241}Am (59.54 keV), ^{133}Ba (80.99 keV) and ^{57}Co (122.06 keV) as radioactive sources for this purpose.

Note: We investigated the dependency of the energy resolution on the PreAmp setting as well. We tested the values 170, 210 and 240 (The detector is usually used in the range from 160 to 240.). All the other DAC settings were set according to table III.3. We started with the ^{241}Am source but could not observe any reasonable change in the energy resolution and therefore assume that the PreAmp does hardly affect the energy resolution for reasonable PreAmp values.

Dependency on IKrum and THL

First we tested the effect of IKrum and THL on the energy resolution for global spectra. The IKrum values that we tested were 2, 4, 7, 10, 15, 20, 25, 33 and 40. During the evaluation we observed that IKrum 2, 25, 33 and 40 do not give reasonable results[1] and therefore these values go by the board. For the THL we used 180, 190, 215, 230, 250, 270, 295 and 315. As 270, 295 and 315 did not produce any reasonable results (too much of the spectrum is cut, as the threshold is too high), they go by board as well. All the other DAC settings were set according to table III.3.

The dependency of the TOT spectrum on the IKrum is shown exemplarily on figure III.35 (a). It is the spectrum of ^{57}Co for the IKrum values 4, 10 and 15. The TOT values grow higher with declining IKrum because the voltage pulse length increases with smaller IKrum. With increasing THL more and more of the spectrum is cut and therefore the TOT values go down with increasing THL. It is shown on figure III.35 (b) for the THL values 190, 215 and 295. We can see that for THL 295 the 14.41 keV peak is already below the threshold and the right part of the spectrum is merged all together.

The dependency of the energy resolution on the IKrum for ^{241}Am (blue), ^{133}Ba (red) and ^{57}Co (brown) is shown on figure III.36 (a). The energy resolution limit (parameter α of the fit function III.12) are the green boxes. The dependency on the THL is shown on figure III.36 (b). Unfortunately no real trend can be observed. The reason for this is that the energy resolution for global spectra is limited by the pixel-to-pixel variations and therefore no significant effect can be observed.

Nevertheless an effect can be observed if pixel-by-pixel spectrum reconstruction is taken into account. If IKrum is set to 4 and THL to 215, the energy resolution for lower energies increases whereas the energy resolution for higher energies is less affected. We achieved an enhancement for ^{241}Am, ^{133}Ba and ^{57}Co. The values are given in table III.5.

DACs	^{241}Am	^{133}Ba	^{57}Co
IKrum 10, THL 190	5.6	3.5	2.5
IKrum 04, THL 210	3.4	3.2	2.3

Table III.5: The energy resolution of ^{241}Am,^{133}Ba and ^{57}Co given in % for two different DAC settings measured with a pixel-by-pixel calibration. The relative errors are about 2 %.

1 In the first case the current is too small and the capacitor cannot be decharged fast enough. In the other cases the pulse is too short and the spectrum is jolt altogether; the peaks are smeared into each other.

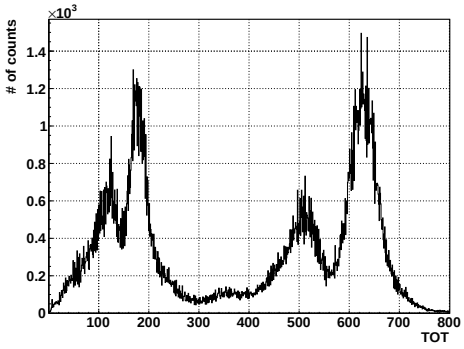

(a) IKrum 04, THL 190

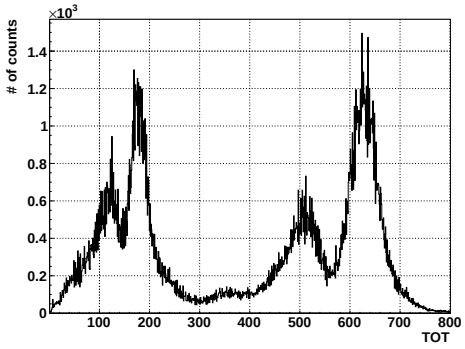

(b) THL 190, IKrum 04

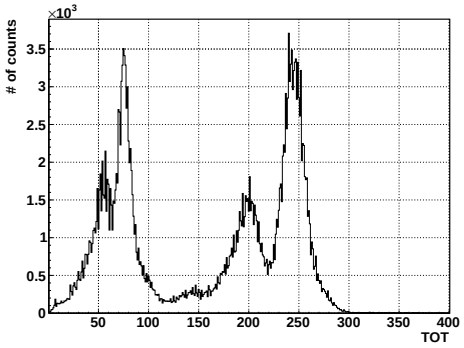

(c) IKrum 10, THL 190

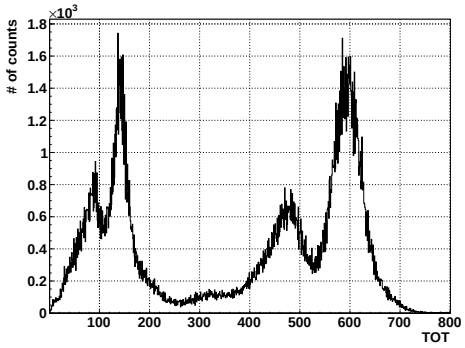

(d) THL 215, IKrum 04

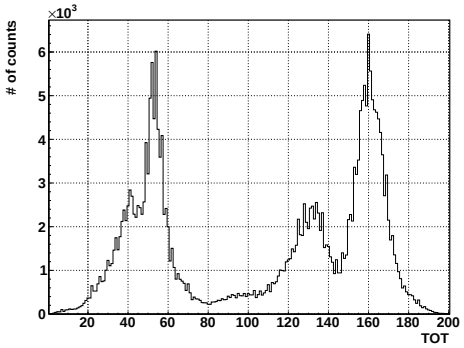

(e) IKrum 15, THL 190

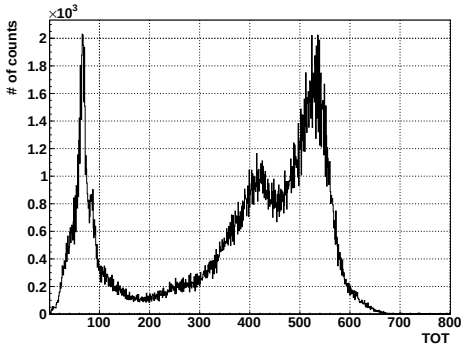

(f) THL 295, IKrum 04

Figure III.35: The dependency of the TOT spectrum of ^{57}Co on the IKrum ((a),(c),(e)) and the THL ((b),(d),(f)).

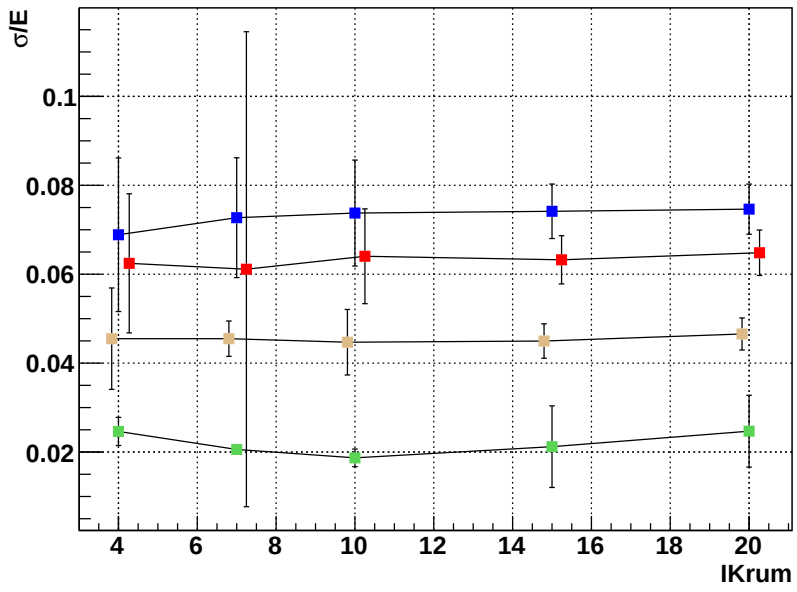

(a) IKrum (THL 190)

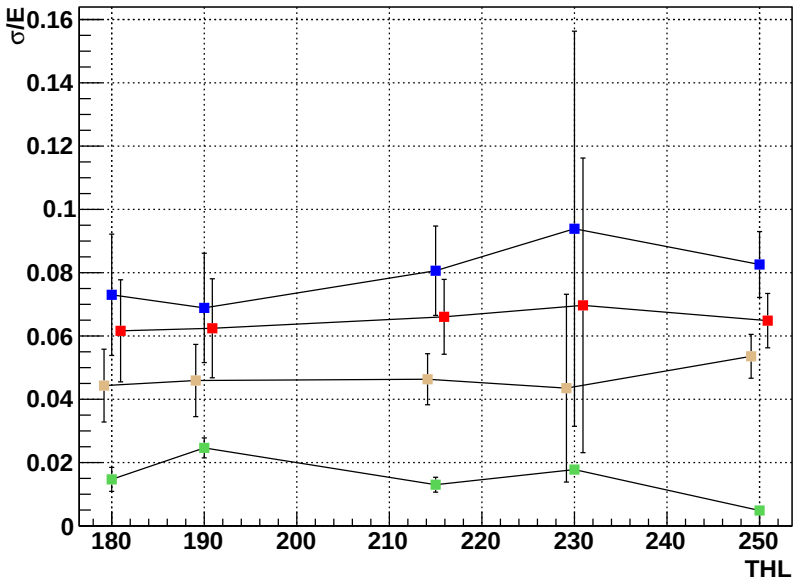

(b) THL (IKrum 10)

Figure III.36: The dependence of the energy resolution on the IKrum (a) and the THL (b) measured with a global calibration. The boxes are ^{241}Am (blue), ^{133}Ba (red), ^{57}Co (brown) and the energy resolution limit (green). The boxes are slightly shifted against each other in the plot for a better visibility but do belong to the values given in the text.

Dependence on the bias voltage

We tested the dependence on the bias voltage for 300 V, 400 V, 500 V, 600 V and 700 V but even voltages up to 800 V should be possible as the leakage current is still below 20 μA for 800 V. Nonetheless we did not use this voltage to prevent the detector from taking any damage in case the voltage increases abruptly due to any unpredictable reasons. The energy resolution was investigated for pixel-by-pixel spectrum reconstruction as the desirable effect is smeared out in the global spectra (see previous subsection).

The first important observation was that the number of bad pixels (in this case, always counting pixels) increased with the bias voltage. On figure III.37 the interdependency between the number of bad pixels and the bias voltage is shown. The number of bad pixels is the average number of pixel per frame which had TOT entries above 11000. The relative errors for both quantities are lower than 1 % and therefore neglected on the plot. The dependency is apparently not linear. At 300 V there are 20 bad pixels whereas at 700 V the number increases up to 226. We fitted a power law (red) of the form N(V) = $a \cdot (V - b)^2 + c$ and an exponential function (green) of the form N(V)= $a \cdot \exp(-b \cdot V)$ to the data points. The power law seems to fit the data better and is therefore a good first approximation to describe the diagramed interdependency.

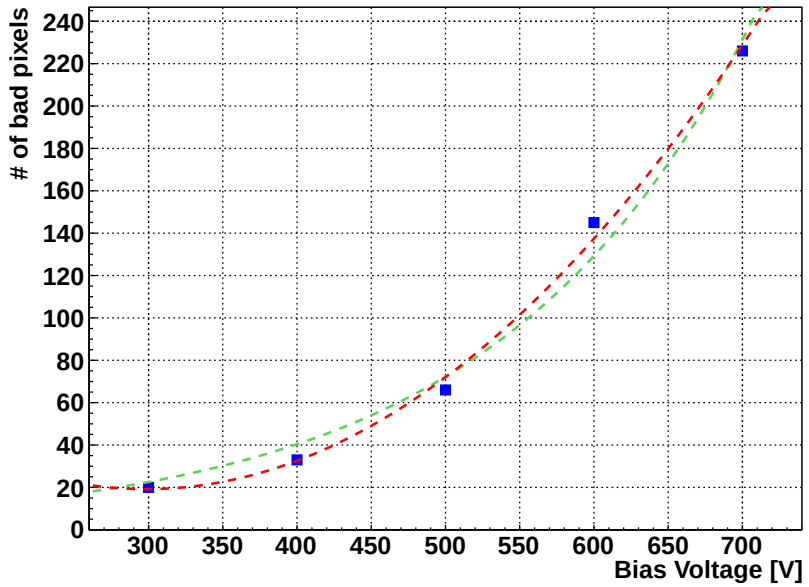

Figure III.37: The interdependency between the number of bad pixels on the matrix and the bias voltage. A power law (red) of the form N(V) = $a \cdot (V - b)^2 + c$ and an exponential function (green) of the form N(V)= $a \cdot \exp(-b \cdot V)$ are shown as possible fit functions. The parameters are a = $1.3 \cdot 10^{-3} \pm 2.67 \cdot 10^{-05} \frac{1}{V^2}$, b = 298.4 $\pm$ 4.3 V and c = 1.91 $\pm$ 0.95 (power law); a = 3.94 $\pm$ 0.11 and b = $-5.81705 \cdot 10^{-03} \pm 4.519 \cdot 10^{-05} \frac{1}{V}$ (exponential).

We measured the energy resolution of the most prominent ^{241}Am and ^{57}Co lines. The dependence of the energy resolution on the bias voltage is shown on figure III.38 (blue is ^{241}Am, red is ^{57}Co). As expected, a clear trend can be observed. The energy resolution increases with the bias voltage. By increasing the bias voltage from 300 V to 700 V the energy resolution for ^{241}Am (at 59.54 keV) can be increased from 3.6 % to 3.2 % (which is an improvement of 11.1 %) and for ^{57}Co (at 122.06 keV) from 2.8 % to 2.1 % (which is an improvement of 25 %).

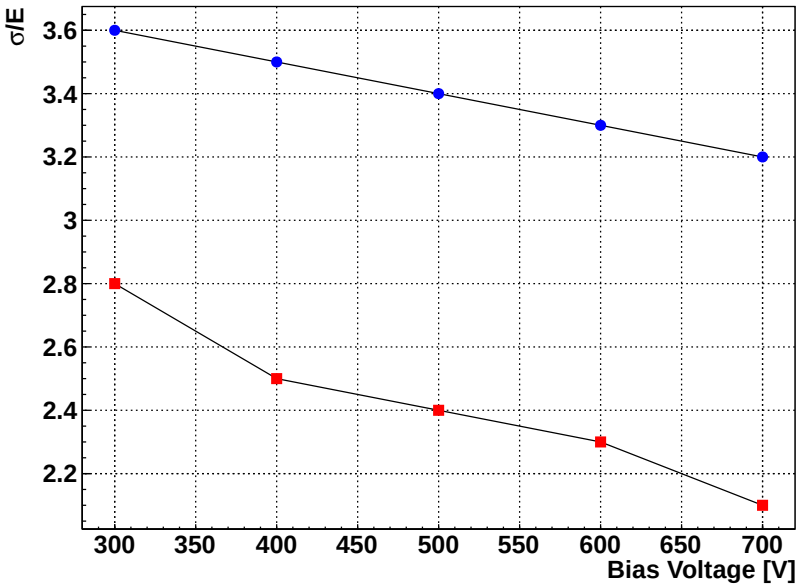

Figure III.38: The energy resolution plotted versus the bias voltage in V for (blue) ^{241}Am (at 59.54 keV) and (red) ^{57}Co (at 122.06 keV) with a pixel-by-pixel calibration.

III.5 Summary

We could apply the common calibration techniques (calibration with radioactive sources and fluorescences) to perform a global and a pixel-by-pixel calibration for a CdTe Timepix detector. Especially for the pixel-by-pixel calibration it is convenient to use radioactive source since they are reliable and stable (particularly in comparison to X-ray tubes). These properties provide good and homogeneous hit statistics all over the sensor which is required to ensure a high quality pixel-by-pixel calibration.

The automatization of the pixel-by-pixel calibration worked out well. By the developed automatic routine 99.7 % of the pixel could be calibrated successfully. With better statistics an even higher coverage can be achieved. The fitting procedure parameters have to be determined only once for particular DAC settings and particular radioactive sources. In fact, if the detectors are more or less equivalent[1], the automatization settings can be applied for all detectors. This is important if a large setup with Timepix detectors (~10^4 detectors) is considered. The calibration process of this large amount of detectors could be performed automatically with radioactive sources, a robotic setup and a appropriate software package. The software developed for this work could easily be adjusted for this purpose.

The reliability of the calibration curve was tested. The result was unsatisfying especially in the nonlinear (E < 20 keV) part and for energies higher than the highest calibration point (E > 120 keV). In the non-linear part the deviations from the expected values are about 5 %. In the linear part they are smaller than 1 % and increase in the extrapolation part with energy. They rise (in first approximation linearily) up to 1.6 % at 356 keV. The deviations seem to be distributed homogeneously across the matrix except for the Tellurium inclusions, at which the pixels are not working properly and therefore no reliable calibration can be established.

The energy resolution was measured for single clustering spectra with the global calibration and the pixel-by-pixel calibration. For really small energies (E < 17 keV) the pixel-by-pixel calibration does not provide a significant improvement of the energy resolution whereas for energies higher than 40 keV the energy resolution improves by about a factor of 2 - 3. Particularly for fluorescences the energy resolution improves significantly since only with the pixel-by-pixel calibration nearby K_α and K_β lines can be resolved. The energy resolution limit towards high energies is $\alpha = 4.1$ % for the global and $\alpha = 1.01$ % for the pixel-by-pixel calibration. Compared to the simulation results which claim an energy resolution of 0.54 α = % in the limit, we still lack a factor of 2. The simulation takes into account all the physics in the sensor material but does not for all process in the electronics.

1 Equivalent in this context means that the TOT spectra do not vary between different detectors if they are used with the same DAC settings.

The variation of the DACs IKrum and THL does not affect the energy resolution for the global calibration; however, for the pixel-by-pixel calibration the energy resolution for energies lower than 120 keV can be increased by lowering the IKrum and increasing the THL.

Concerning the bias voltage it was possible to push it up to 800 V. We performed measurement runs without damaging the detector at least with 700 V. On the one hand the energy resolution could be increased by increasing the bias voltage. Especially for higher energies the energy resolution could be increased by 25 % by going from 300 V to 700 V. But on the other hand the price you have to pay is the increasing amount of bad pixels on the matrix, which increased from 20 to 226. Hence the effective detection area is decreased and it is questionable if the amount of valuable events and therefore the effective sensivity can really be increased by a higher voltage.

Overall we can state, that by optimizing the working parameters the energy resolution could be increased by almost 67 % at the 59.54 keV peak of ^{241}Am and concerning the data analysis, a detector can be calibrated automatically without any problems.

IV Background Identification and Energy Resolution for Tracks

Contents

IV.1 Clustering, α-particle and muon identification . . . 75
IV.1.1 Identification of α-particles . . . 77
IV.1.2 Identification of muons . . . 79
IV.2 Discrimination of one and two electron tracks . . . 82
IV.2.1 Artificial neural networks . . . 84
IV.2.2 The pair production experiment . . . 86
IV.3 Energy resolution for tracks . . . 101
IV.3.1 The energy resolution for tracks at 661.5 keV . . . 101
IV.3.2 The energy resolution for pair production events at 1588.53 keV . . . 101
IV.4 Summary . . . 104

The great advantage of pixelated detectors are the funny coloured pictures that you get after the analysis. They allow you to extract not only the energy of an event but identify its type as well: Was it a muon or probably a low energy X-ray photon? This sort of questions can be solved by a simple glance at a 2D histogram where the color of each bin indicates the energy deposition in this pixel (as shown on figure IV.1[1]). This is a two dimensional projection of the particle track in the sensor layer. Our eye can easily identify structures like (A) as α-particles, structures like (B) as muons or structures like (C) as electrons. All events which are undesirable can be identified and sorted out. This would provide a very elegant method to suppress background - no veto or shielding is actually necessary, just let it go and then pick out the events you like. Sounds pretty nice, in theory, but we all know - life isn't that easy. In fact, as we know from simulations (see [29]), there are a lot of events which generate very fancy graphical patterns. You can try to identify them but you will find out pretty fast - that is a really, really troublesome business. For these cases more sophisticated pattern recognition techniques have to be applied.

1 On such plots the colour always denotes the energy deposition in keV.

But one after the other. The background are photons, α-particles, muons and electrons. Low energy photons ($E_{ph} < 200$ keV) will deposit their energy in a small amount of pixels and are easy to sort out. Therefore we will skip this case as it is not really challenging. More detailed we have to look at other kind of expected background - α-particles, muons and electrons: The first section of this chapter deals with the easier task - clustering and the identification of α-particles and muons. The second section is about the tough story - the separation of one electron and two electron events by artificial neural networks (ANNs). After a short introduction to the concept of ANNs (which is roughly following [30]), we will present the results of employing ANNs on experimental data.

One of the most important questions considering a large scale experiment is the energy resolution for electron tracks. As stated in the motivation the $2\nu\beta\beta$ and $0\nu\beta\beta$ can only be distinguished by their energy signature and therefore a high energy resolution of the detector is required. We measured the energy resolution for several track energies and compared it to the predictions of the simulation. This is presented in the last section.

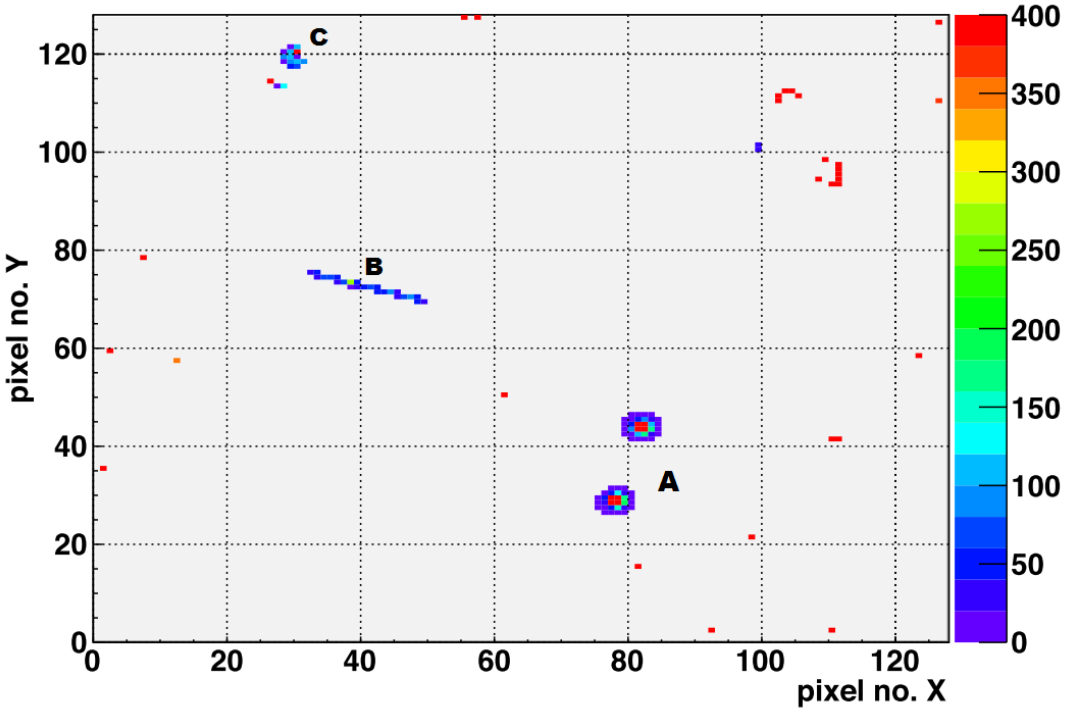

Figure IV.1: The pixel matrix of a measured frame. The colour denotes always the energy deposition in keV. There are two α-particle (A), a muon (B) and an electron (C) on the picture.

IV.1 Clustering, α-particle and muon identification

Before the actual identification can take place, all the events on the matrix have to be "sliced out" to be analyzed individually later. This process is called "clustering". We define a cluster as a set of pixels with the following two properties:

1. Every pixel has energy deposition entries bigger than zero. We will call such pixels "non-zero" pixels.
2. Every pixel in the cluster has at least one neighbour within a distance of 1.

The meaning of distance[1] in this context is illustrated on figure IV.2. The green pixels have distance of 1 to the pixel in the center; the blue pixels a distance of 2 and so on. We will call neighbours of distance δ δ-neighbours (The green pixels are therefore 1-neighbours and the blue pixels 2-neighbours to the central pixel.). The size of a cluster is the number of pixels it contains. We will call a cluster of size σ a σ-cluster. Figure IV.3 (a) shows a 5-cluster; on figure IV.2 (b) you can see a 6-cluster A. Cluster B does not belong to cluster A as there are no pixels in cluster B to have a neighbour within a distance of 1 belonging to cluster A. For the clustering process we used a recursive algorithm[2] with the following structure:

1. Save all the positions of all "non-zero" pixels in a set P.
2. Take the first pixel in the position set P, remove it from the position set P, and add it to a new cluster set C_i.

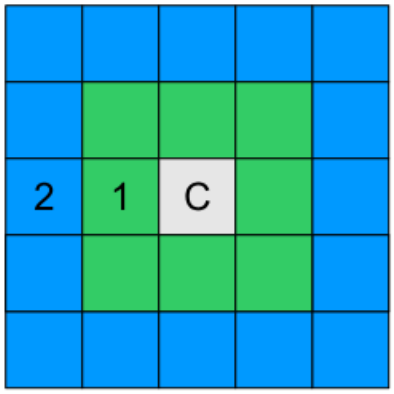

Figure IV.2: The definition of "distance" and "neighbour". The green pixels have distance of 1 to the pixel in the center; the blue pixels a distance of 2. The green pixels are 1-neighbours to the central pixel, the blue pixels 2-neighbours.

1 The concrete definition of distance between two pixels i and j is d(i,j) := max($|x_i - x_j|$,$|y_i - y_j|$). x and y are the positions of the pixels on the matrix (which are natural numbers).

2 A C++ implementation of this algorithm is given in Appendix B.

3. Add all 1-neighbours of this pixel to C_i and remove them from P.
4. Repeat the last step for all the pixels added to C_i in the last step.
5. If there are any pixels left in the set P, start over from step two. If P is empty, stop.

An example for this process is given on figure IV.4. The numbers denote the energy deposition in each pixel. We see a 5-cluster. It is recognized in the following way: In the first step the green pixel is added to the cluster and checked if it has any 1-neighbours. Indeed, this is the case and therefore the two red pixels are added to the cluster. All pixels which were added to the cluster are set to 0. In the second step the first pixel that was recognized as a 1-neighbour in the previous step is checked whether it has any 1-neighbours. The red pixel is added and set to 0. In the third step the green pixel is checked for 1-neighbours but does not have any and therefore the procedure is continued in step 4 with the next pixel in the cluster which was not checked for neighbours yet. The last neighbour is found, added to the cluster and checked for neighbours in step 5. After step 5 all pixels were checked for neighbours and no more neighbours can be found. The procedure is over and the cluster is recognized (step 6).

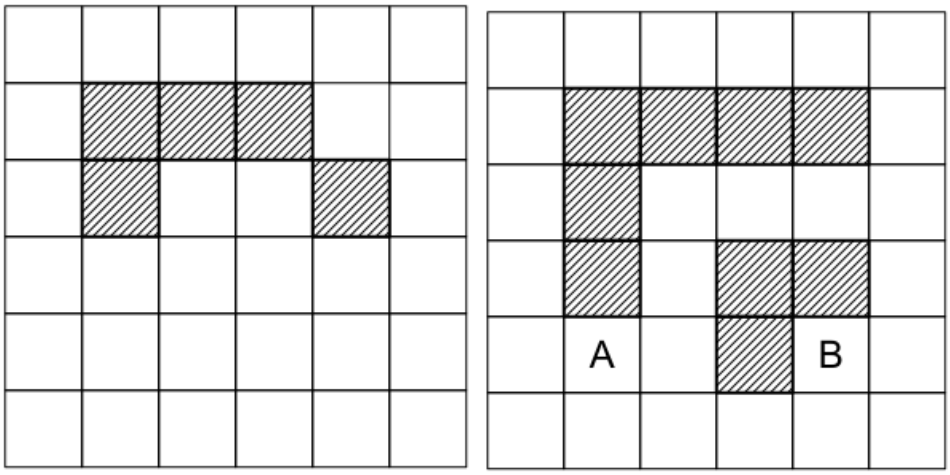

(a) 5-cluster **(b)** 6-cluster

Figure IV.3: A 5-cluster (a) and a 6-clusters with a 3-cluster (b).

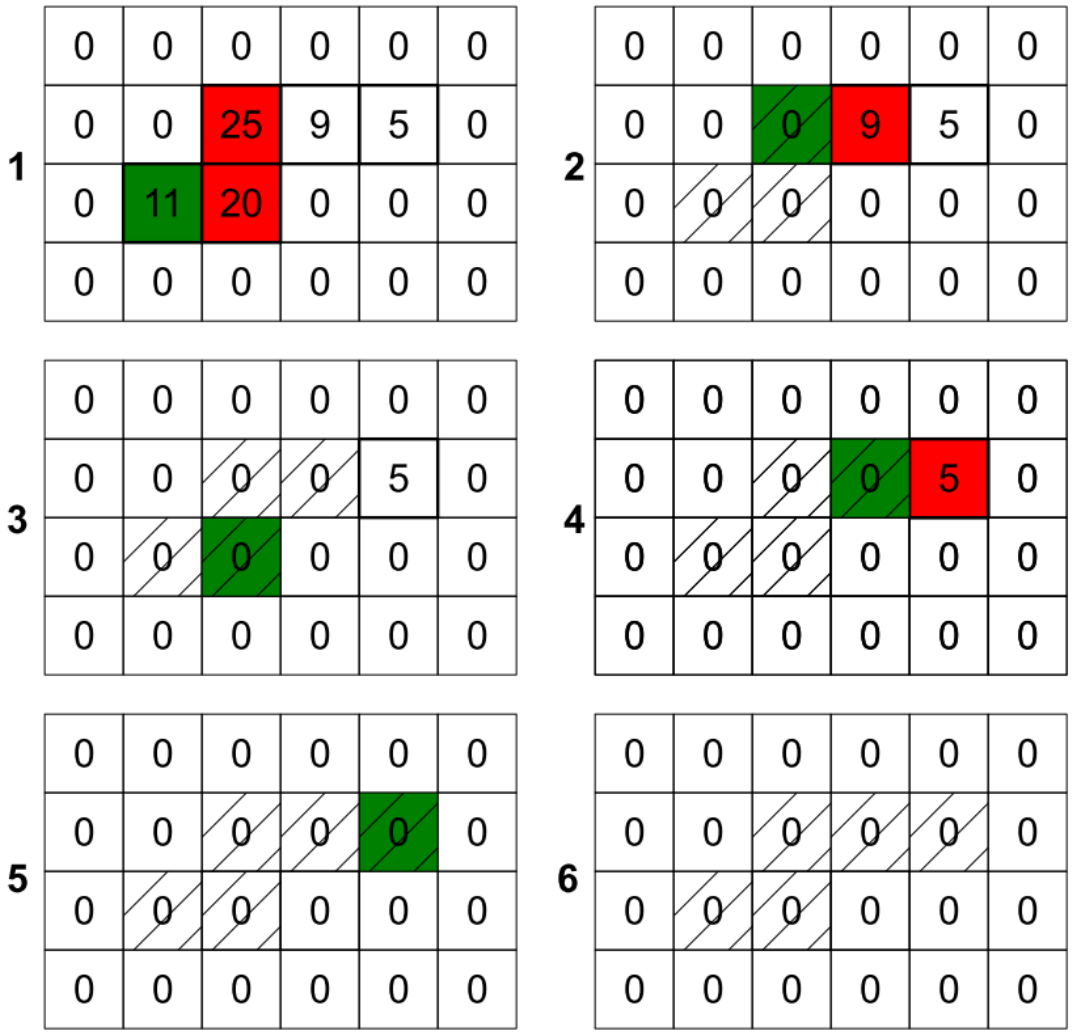

Figure IV.4: An example for the functionality of the clustering algorithm. The hachured pixels belong to the cluster after the previous step.

IV.1.1 Identification of α-particles

The easiest kind of events to identify are α-particles. Some examples are shown on figure IV.14. The clusters they form usually have a size between 20 and 30 pixels (for a chip with 110 μm pixel pitch !), 3 - 5 pixels with very high energy deposition in the center and a circle / square shape. These properties make them unique in comparison to any other sort of background events, that can normally be expected, and these properties can be used to identify α-particles with a very high efficiency. We used the following algorithm to identify α-particles[1]:

1 A C++ implementation of this algorithm is given in Appendix B.

1. Check, if there is at least one pixel in the cluster, having at least eight 1-neighbours.
2. Check if the pixel with the highest energy deposition in the cluster has at least 20 neighbours within a distance of 1 or 2.
3. If both conditions are fulfilled the cluster is considered to be the signature of an α-particle.

Considering this work the algorithm was highly successful and there was not one case of a misidentification. Of course, cross-overs of α-particles with other particles like muons or electrons will be considered as α-particles as well. But since these cases are undesirable background events, too, these mistakes can be accepted without any problems. Additionally, postprocessing is possible to identify crossovers.

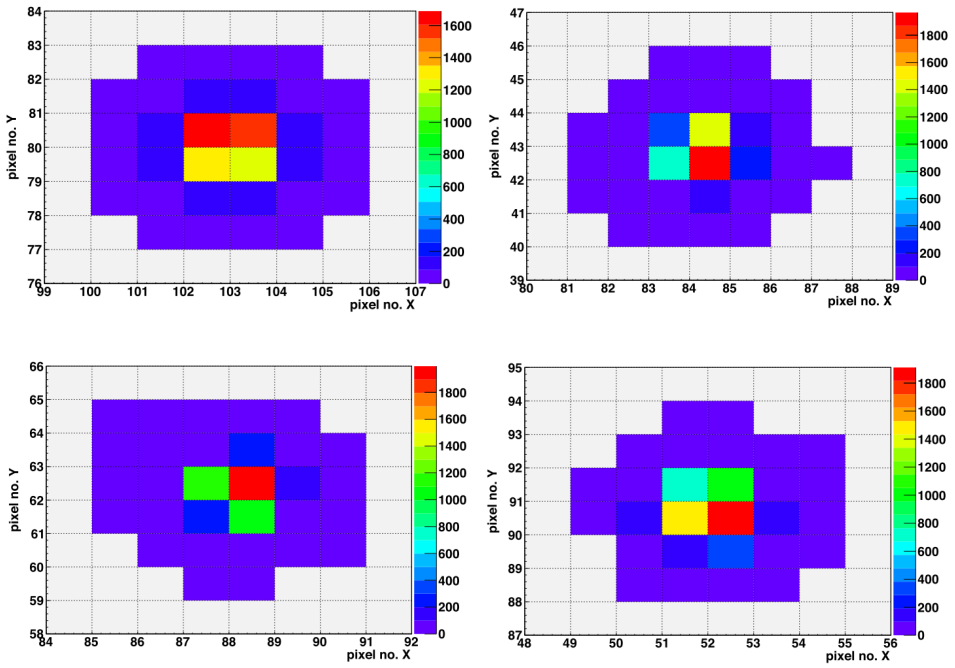

Figure IV.5: Some examples for α-particles detected with the Timepix detector.

IV.1.2 Identification of muons

The next kind of background we want to discuss are muons. After α-background is eliminated, this is the next sort of background to be rejected. As muons have a high kinetic energy and a high mass compared to the electron mass, their kinetic energy and momentum is hardly affected by the scattering within the sensor layer and they go straight through the sensor. The typical graphical pattern is a straight line as shown back on figure IV.1. Apparently, the linearity is the most distinct property in the graphical pattern of a muon and thus we will use it to identify this kind of particle. We used a reduced Hough Transformation to recognize the line structure of the tracks.

The idea is to transform the original illustration from the (x,y)-coordinate space to a parameter space more suitable for line recognition. We will characterize the track information by the angle ϕ which is the angle between the x-axis and the line connecting two pixels (see figure IV.6). The angle is calculated for every pair of pixels and filled into a histogram.

By this histograms electrons can be clearly distinguished from muons. As muon tracks are highly linear, there is a strong accumulation around a particular angle. On the opposite the angles for an electron track are spread wider. On figure IV.7 four muon tracks (on the left) and their reduced Hough Transformation are shown (on the right). The same is shown for electron tracks on figure IV.8. The differences can clearly be recognized. We projected all angles between 0 and 2π back to the interval $(0; \frac{1}{2}\pi]$ as the projection still provides enough information to recognize the two sorts of events but is easier to handle if the tracks are short.

To distinguish between muons and electrons automatically, we rebinned the histrogram of the reduced Hough Transformation by a factor of 8 and searched for the position of the maximum bin. Let's call this point on the ϕ-axis P_{mb}. Then, if 80 % of the histogram's entries are in the interval $[P_{mb}$ - 10°; P_{mb} + 10°], the event is considered to be the signature of a muon.

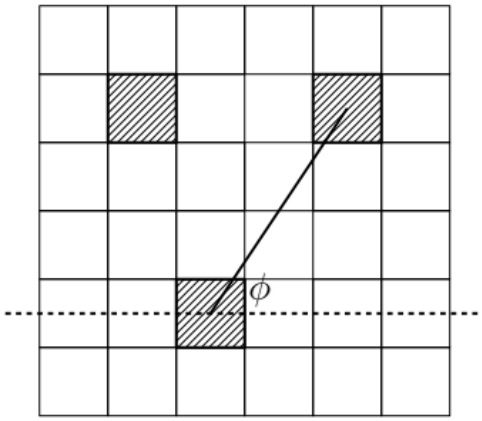

Figure IV.6: The definition of the angle ϕ for the reduced Hough Transformation.

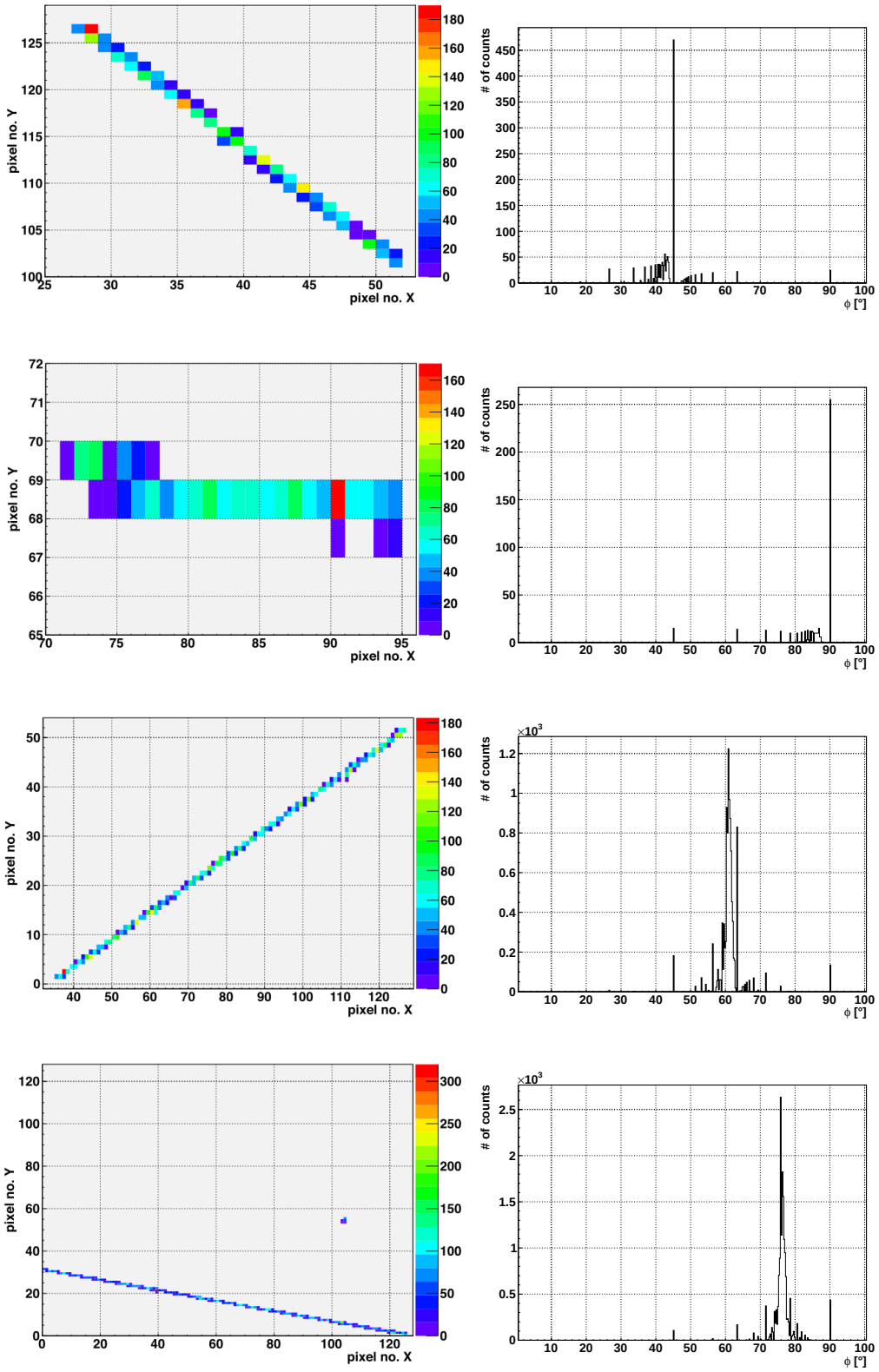

Figure IV.7: Four typical muon tracks and their reduced Hough Transformations.

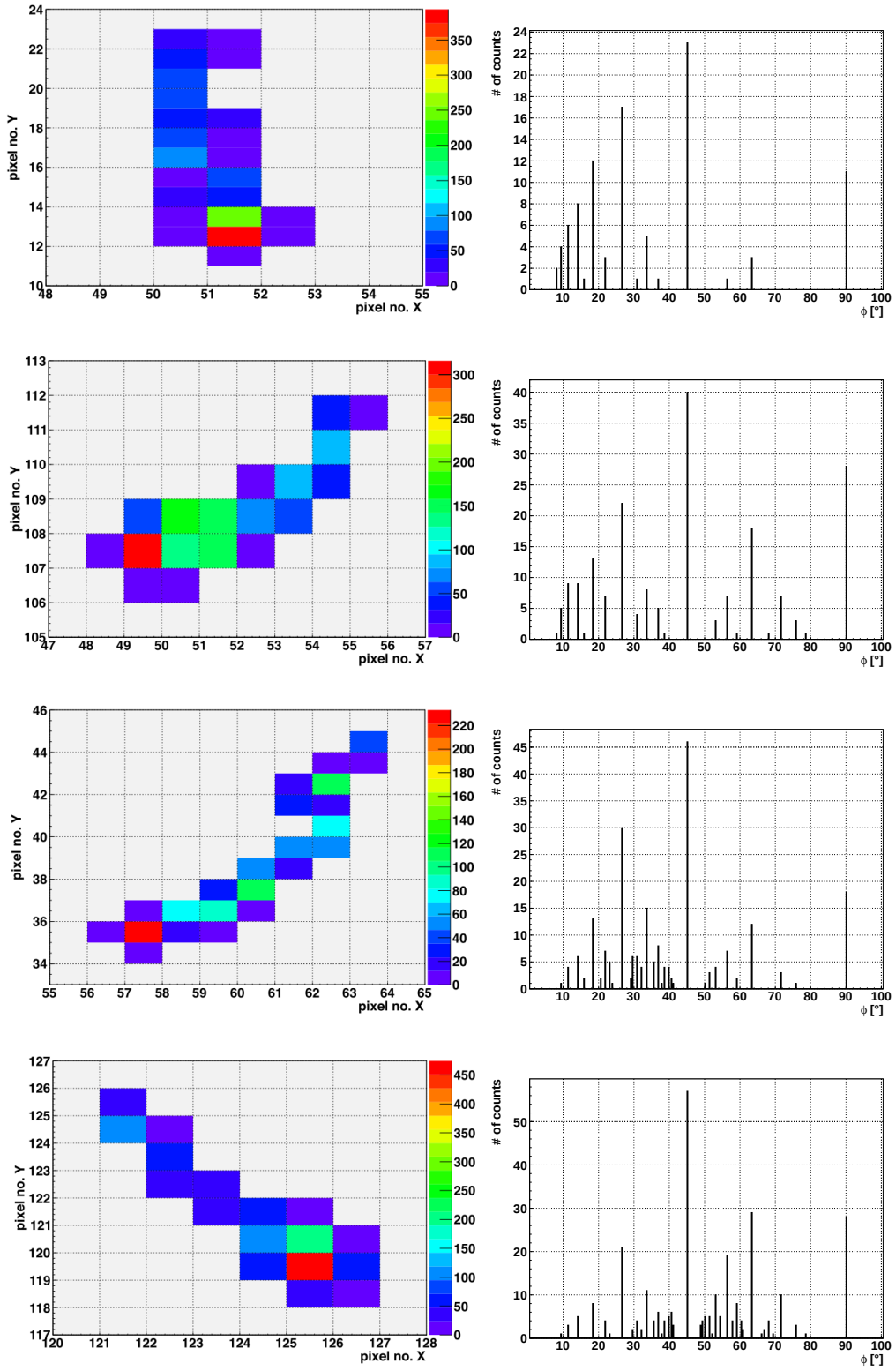

Figure IV.8: Four typical electron tracks and their reduced Hough Transformations.

IV.2 Discrimination of one and two electron tracks

As stated in the introduction of this chapter, electrons are the most challenging kind of background in connection with background identification by graphical pattern analysis. Indeed, if you take a look at the first four events on figure IV.9, on the one hand it is pretty clear that (a) and (b) are highly probably two but (c) and (d) are one electron tracks. You can see the two so-called "heads", where most of the electron energy is deposited. According to the Bethe-Bloch-formula for electrons[1]

$$\frac{dE}{dx} = \frac{4\pi e^4 N_A}{c^2 m_e} \frac{Z}{A} \frac{1}{\beta} \left(\ln \frac{m_e c^2 \gamma \beta^2}{2I} - \beta^2 - \frac{1}{2}\delta \right) \tag{IV.1}$$

the highest energy deposition is at the end of the track, where most of the initial particle energy is already lost. On the other hand, the last four pictures show "bad" events. In these four cases it is much harder to make the right guess; (e) and (f) are two electrons, whereas (g) and (h) are one electron - would you have guessed it right?

A possible approach to face this problem is to use artificial neural networks. We will introduce the basics of this concept in the next subsection. We trained the networks with simulated data of one and two electron events and tested their classification efficiency in an experiment which will be presented in the second next subsection.

1 Discussed in detail in [31] and [2].

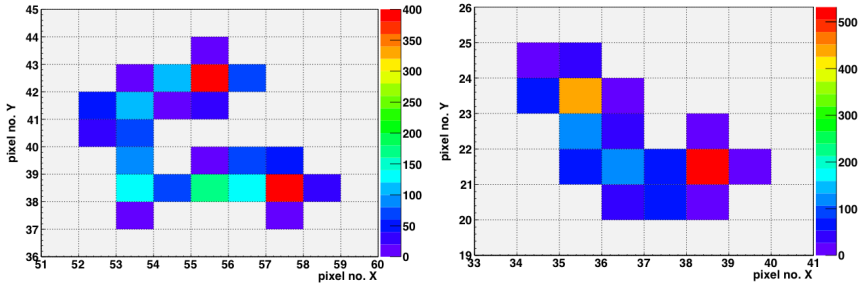

(a) two **(b)** two

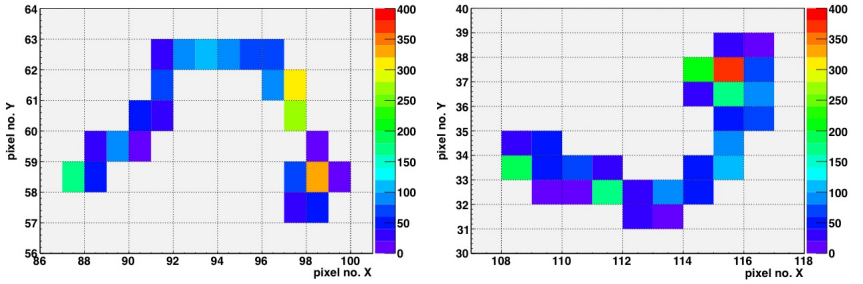

(c) one **(d)** one

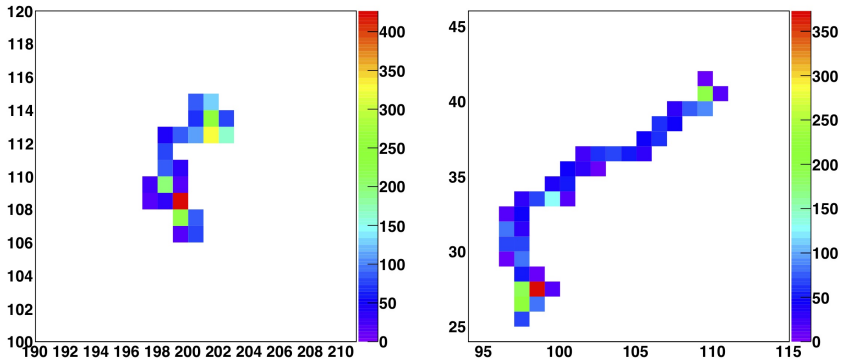

(e) two **(f)** two

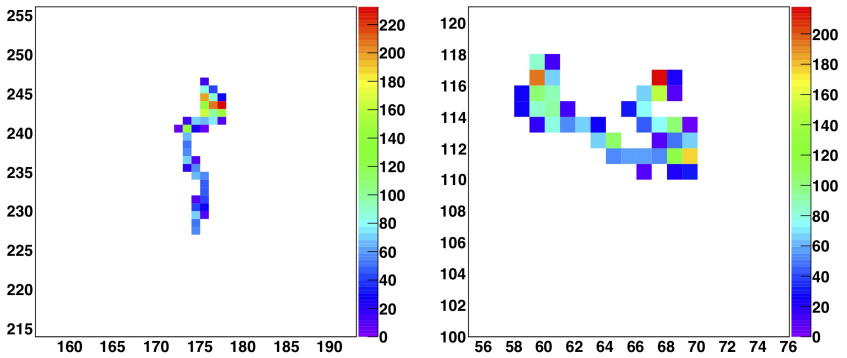

(g) one **(h)** one

Figure IV.9: Four two electron (a,b,e,f) and four one electron tracks (c,d,g,h). Tracks (a) - (d) were measured whereas (e) - (f) were generated by simulations. Particles on (a) - (d) had an energy of about 2.3 MeV and (e)-(f) are tracks of particles with 2.8 MeV.

IV.2.1 Artificial neural networks

The idea of artificial neural networks (ANNs) is to create a system which implies properties of the human brain and can be used for similar tasks. The elementary cell of an ANN is, analogue to the human brain, a neuron. A real neuron consists of the main body, called the soma, where the signals are processed. The signals are injected through the dendrits and the processed output signal is forwarded to the next neurons or other cells by the axons. An easy, but useful, model for the functionality of this system is the following (see figure IV.10):

We denote the value of the N input signals as I_1,..,I_N. While they are coupled into by the dendrites, they are weighted with the weights ω_1,..,ω_N, respectively. In the soma the weighted sum of the input signals is calculated:

$$\sigma = \sum_{j=1}^{N} \omega_j I_j \tag{IV.2}$$

The output signal of the cell Ω is determined by a non-linear activation function f. A simple example for f can be a Heaviside step function: $\Omega = \Theta(\sigma$ - s). In this case the output signal Ω is either 1 (if the sum of the input signal σ is above a particular threshold value s, $\sigma >$ s) or 0 ($\sigma <$ s). If a continuous output signal is required, a typical example for f would be

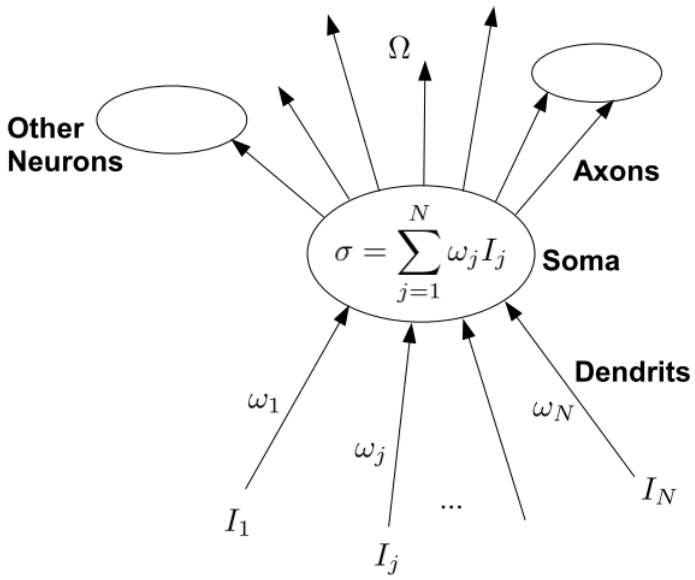

Figure IV.10: The basic model for a neuron, consisting of the dendrits, the soma and the axons.

$$f(x) = \frac{1}{1 + \exp(-x)}. \tag{IV.3}$$

With one single neuron basic logical operations like the AND- and OR-function can be realized easily: Take a neuron with two input channels I_1, I_2 and use the Heaviside step function $\Theta(x)$ for f. If you choose $\omega_1 = \omega_2 = 1$ and s = 0.25 the neuron will be equivalent to an OR-Gate. For $\omega_1 = \omega_2 = 0.5$ and s = 0.75 an AND-Gate is realized.

Such neurons can be combined in various ways to form a neural network. The easiest way to built up a network is to use N independent neurons[1]. All of the neurons receive the same M input signals. This kind of network is called a perceptron. The task of our perceptron is to identify particular input pattern (an input pattern is a particular set of values for the input signals) and sort them into equivalence classes. If we denote such an input pattern as $\vec{I}^{\nu}$ with ν = 1,..,q (for instance q photos of N people) and if for every ν it is known to which of the N equivalence classes $\vec{I}_{\nu}$ belongs to (in our example the equivalence classes are the identities of the people on the photos), then one particular of the N neurons should give an output signal to identify the equivalence class. The condition for the r-th Neuron to give an output signal is

$$\sigma_r = \sum_{j=1}^{M} \omega_{r,j} I_j^{\nu} > 0. \tag{IV.4}$$

Now the question is: If the pattern are in such a way, that they can be theoretically separated by a perceptron (then the pattern are called linear separable), how the weights $\omega_{r,j}$ have to be chosen to perform this task? The process of finding the right weights is called "training". A simple example how to do it is the following:

1. Start with a random, reasonable matrix of weights $\omega_{r,j}$ and classify the events.
2. If the classification was correct, do not change the weights. If the classification was wrong, adjust the weights for every neuron R whose output signal was wrong by the so-called "Delta Rule"

$$\Delta\omega_{r,j} = \lambda(\Omega_r^{soll} - \Omega_r^{ist})I_j. \tag{IV.5}$$

3. Repeat step 2 until the weights $\omega_{r,j}$ are chosen in such way that the classification is performed correctly.

1 Independent means, that the neurons are not connected among themselves. An axon of one neuron is never the dendrit of another.

The positive parameter λ is called learning rate and is usually chosen $\lambda \ll 1$. For linear separable pattern the process always converges if the learning rate is $\lambda = \frac{1}{\left|\left|\vec{I}\right|\right|}$ (see [32]). $\left|\left|\vec{I}\right|\right|$ is the norm of the presented input signal. Apparently, the training is an optimization problem and therefore in the application techniques like Simulated Annealing or evolutionary algorithms (see [30]) are used to perform the training.

As suggested above not every pattern is linear separable - in fact, this is the case in our problem. We wanted to distinguish between single electron and double beta events. These are our equivalence classes - only two actually; again sounds easy but it isn't since the variety for image patterns falling into this two classes is enormous. For our problem we used a more complicated ANN structure with ten input signals for the neurons. We will call these input signals "criteria". Some examples for such criteria are the number of pixel hit during an event or the distance between the spatial and the energetic center of mass. The criteria will be discussed in more detail in subsection IV.2.2. We used the FANN package [33] for the implementation of ANNs in our data analysis. The preparation and training of ANNs for the discrimination between single electron and double beta events is discussed in [29].

IV.2.2 The pair production experiment

To verify the predictions of the simulations and the classification efficiency of the ANNs, a preliminary experiment is needed in which the same graphical pattern will occur as in the $0\nu\beta\beta$ experiment which we actually want to perform. From $0\nu\beta\beta$ events we expect the signature of two electrons starting at a common point and spreading (figure IV.9 (a) and (b)). As the detector does not take into account whether the particles are positively or negatively charged, positron tracks will have almost exactly the same shape as electron tracks. Therefore pair production events of the form

$$\gamma \rightarrow e^+ e^- \tag{IV.6}$$

will give us the same graphical pattern as $0\nu\beta\beta$ events[1]. Consequently, the idea is to use a high energetic γ-source in order to generate electron-positron pairs in the sensor with high statistics and discriminate them against an electron background. The electron background will be produced by the same source at the same time because of Compton scattering.

Our source of choice was ^{208}Tl. It is the isotope with the highest γ-line energy of $E_\gamma = 2614.6$ keV existing in a natural decay chain. Subtracting the energy of $2 \cdot 511$ keV for the production of the positron and the electron, they have a kinetic energy of 1588.52 keV to be detected in the sensor. Since the graphical pattern depend not only on the kind

1 After the propagation the positron annihilates but as the annihilation photons have an energy of 511 keV they are usually detected in pixels far from the main cluster or escape from the sensor completely.

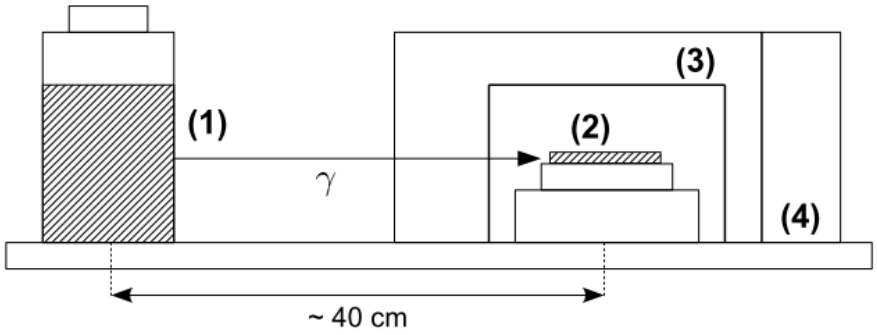

Figure IV.11: A scheme of the experimental setup for the ^{232}Th measurement. (1) The ^{232}Th source, (2) the sensor layer, (3) the cardboard and (4) the lead wall. The distance between the source and the detector was about 40 cm.

of the detected particle but especially on its energy in a very sensitive way (and thus the pattern recognition), we want to come to the Q-value of the $0\nu\beta\beta$ (2813.50 keV) as close as possible. Fortunately, as the γ energy is still sufficiently lower than the Q-value, the line does not provide any background at the Q-value.

The experimental setup is surprisingly easy: A ^{232}Th source (1) (pulverised thorium filled into a transparent plastic tin) was placed in front of the detector at about a distance of 40 cm. The detector lied tapped to a lead block on the table with the sensor layer (2) parallel to the table surface (see figure IV.11). The detector was shielded from low energy photons by a cardboard (3) and from other radiation by a lead wall (4) around the setup. In the experiment we used ^{232}Th instead of pure ^{208}Tl for two reasons: On the one hand ^{208}Tl is in the decay chain of ^{232}Th and about 35 % of the γ-radiation that is emitted from ^{232}Th are 2614.6 keV photons and on the other hand ^{232}Th is much easier to get and handle than pure, enriched ^{208}Tl. We chose a distance of 40 cm to ensure that the photon momentum is parallel to the sensor layer surface for most of the photons hitting the sensor layer. Such photons are more likely to produce tracks which are parallel (and not perpendicular) to the sensor surface and therefore have more reasonable graphical pattern. We used about 400 g of ^{232}Th with an activity of about 14.3 MBq for the 2614.6 keV line. This gives us about 1 - 3 events every 0.3 s, what provides us the maximal possible statistics considering the limitations given by the size of the sensor layer and the frequency of the USB readout (3 Hz).

We recorded 248.2 hours of data and evaluated 34.4 hours for the presentation in this work[1]. After clustering this are 3636025 events. After removing α, low energy γ and muon background, we have 606813 remaining electron (single electron and pair production) events.

1 Actually, we evaluated a much higher part of the data but as the spectra were very similar to each other, we present only a sufficiently significant part of the data here.

The spectrum of ^{232}Th

The event spectrum for the ^{232}Th measurement is shown on figures IV.12 and IV.13. Event spectrum means, that every entry in the spectrum is not the energy measured by a single pixel but the energy summed up for all pixels in a cluster. The bin size is 1 keV. For a clear view we divided the spectrum into a single clustering part (interval [0 keV; 250 keV]) and two electron cluster parts (interval 1 [100 keV; 1100 keV] and interval 2 [1180 keV; 2680 keV]). Every interval has another zoom level as the amount of electron events is much lower than the amount of single photon hits. In these spectra α-particles and muons were already rejected.

We could identify the peaks although they are slightly shifted to the right, which happens because of extrapolation mistakes in the calibration. We will cover this topic in the energy resolution section in detail. Particularly, we want to emphasize on the peaks at 1608 keV and 520 keV, which are actually the pair production and the positron annihilation peak (which is actually overlayed by a γ-peak) shifted to the right from their real positions at 1588.53 and 511.5 keV. The photo peak is rather small (due to the small interaction cross section for the photo effect at high energies) but can still be found at 2650 keV. The shifts can be corrected by the calibration correction function which was presented in chapter III. We will consider this in the energy resolution section in detail.

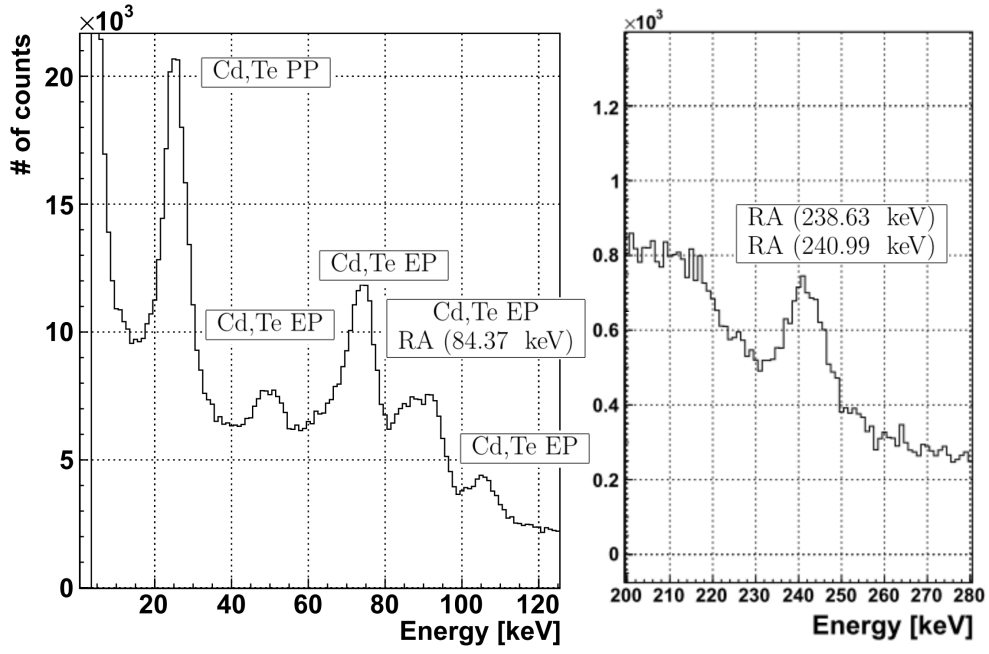

Figure IV.12: The low energy, single-clustering spectrum of the ^{232}Th source. The abbreviations are the origin of the peaks: PP - fluorescence peak, EP - escape peak, RA - γ-line of a radioactive emitter.

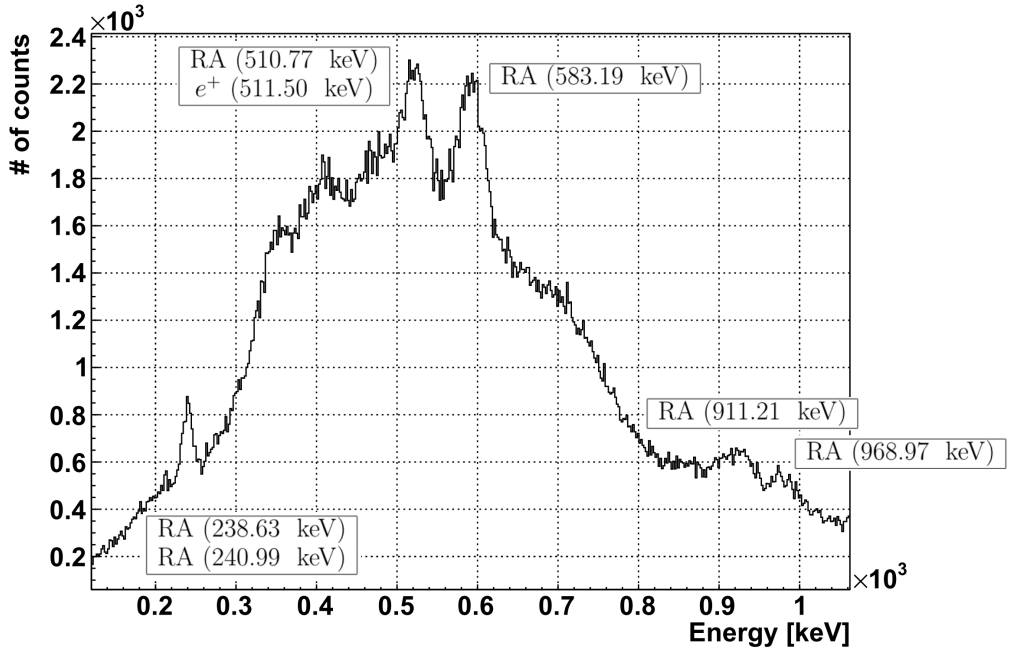

(a) low energy

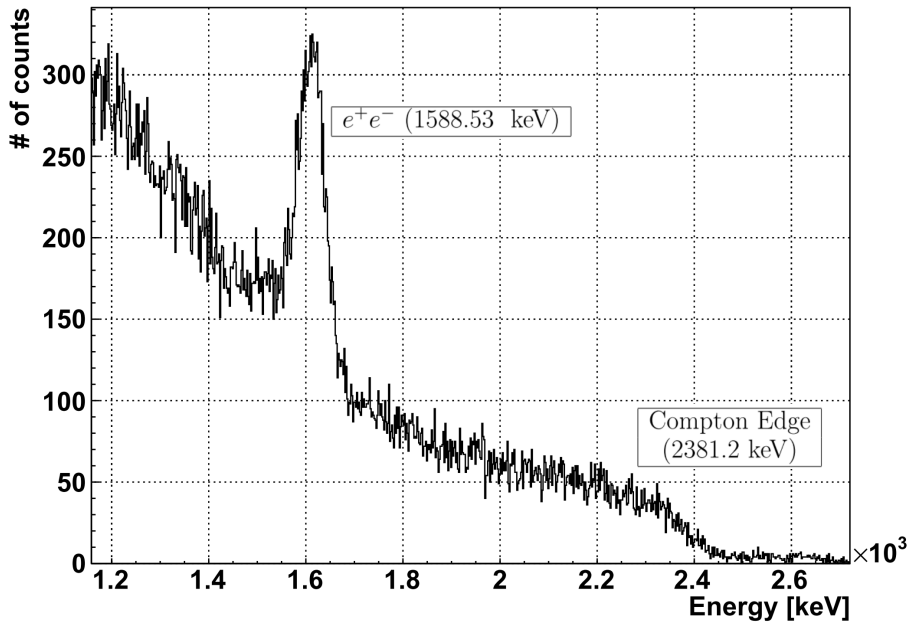

(b) high energy

Figure IV.13: The spectrum of photo-, Compton-electrons and positrons produced in the sensor layer by the radiation of ^{232}Th. The measurement time for this spectrum was 34.3 h. The abbreviations are the origin of the peaks: RA - γ-line of a radioactive emitter, e^+ - photons from electron-positron annihilation, e^+e^- - pair production peak.

If you take a closer look at the Compton spectrum between 1000 keV and 2400 keV (figure IV.13 (b)), you will see that it does not fulfill the plausible expectations. The first point is that if you calculate the expected ratio between pair production events and Compton electrons in the region of interest (in this case it is the interval [1538 keV; 1624 keV] around pair production peak) it is

$$\left(\frac{N_e}{N_{ee}}\right)_{exp} \approx 0.44. \tag{IV.7}$$

However, the ratio that we measured was

$$\left(\frac{N_e}{N_{ee}}\right)_{mes} \approx 0.96 \tag{IV.8}$$

which does not correspond to the theoretical predictions. For our calculations we used the Beer-Lambert-Bouguer law [34]

$$N(x) = N_0(1 - e^{-\rho \cdot \sigma \cdot x}) \tag{IV.9}$$

to compute the number of events contributing to the spectrum. ρ is material density in $\frac{g}{cm^3}$, σ the cross-section for a particular interaction in $\frac{cm^2}{g}$ and x the path-length of the particles through the sensor layer. For the pair production events we extracted the value of σ from the NIST XCOM database [35]. For the Compton electrons we calculated the total cross-section in the region of interest by integrating the Klein-Nishina formula [36]

$$\frac{d\sigma}{d\Omega} = (P(E,\theta) - P(E,\theta)^2 \sin(\theta)^2 + P(E,\theta)^3). \tag{IV.10}$$

P(E,θ) is a formula connecting the energy of the incident photon E with the scattering angle θ and the energy of the scattered photon E_s [36]:

$$P(E,\theta) = \frac{E_s}{E} = \frac{1}{1 + \frac{E}{m_e c^2}(1 - \cos(\theta))} \tag{IV.11}$$

We think that the reason for this loss of Compton scattering events above the region of interest is a high percentage of electrons leaving the sensor material. If an electron leaves the sensor its energy is detected only partially and the electron's actual energy is not detected correctly but underestimated. Compton electrons with energies above the region of interest are produced with initial velocities which have higher angles α (see

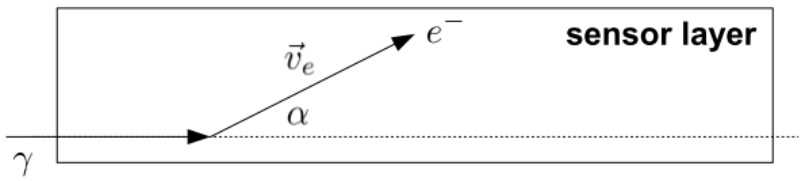

Figure IV.14: The definition of the angle α in the context of the escape of the Compton electrons.

figure IV.14) compared to electrons of pair production events. Therefore a large amount of Compton electrons is lost above the region of interest as they often can escape from the sensor layer and be detected incorrectly within the region of interest.

Indeed, if we compute the real Compton spectrum of the electrons and compare it to the Compton spectrum of the electrons produced by the ROSI simulation (i.e. simulated the detection of the Compton electrons in the sensor layer of a Timepix), we see that the rising wing at the Compton edge is gone in the simulation (see figure IV.15 (a) and (b)). Nevertheless on the left side of the pair production peak the spectrum is not slowly rising as the Compton spectrum in the simulation but the gradient is significantly higher.

Two reasons are likely to contribute to produce this spectrum. The first reason is that electrons which escape the sensor but have a high energy are sorted into the spectrum at the wrong position and consequently contribute to the wrong part. The second reason is that we did not take multiple Compton scattering within the detector into account when we calculated the cross sections. If a photon was involved in a Compton scattering process but maintained a large percentage of its initial energy, a second Compton scattering process is not unlikely and therefore processes of this kind can lead to inflated counting rates at lower energies.

Still additional contribution may be provided by the background radiation (radiation in absence of the ^{232}Th source) which is presented in the next subsection.

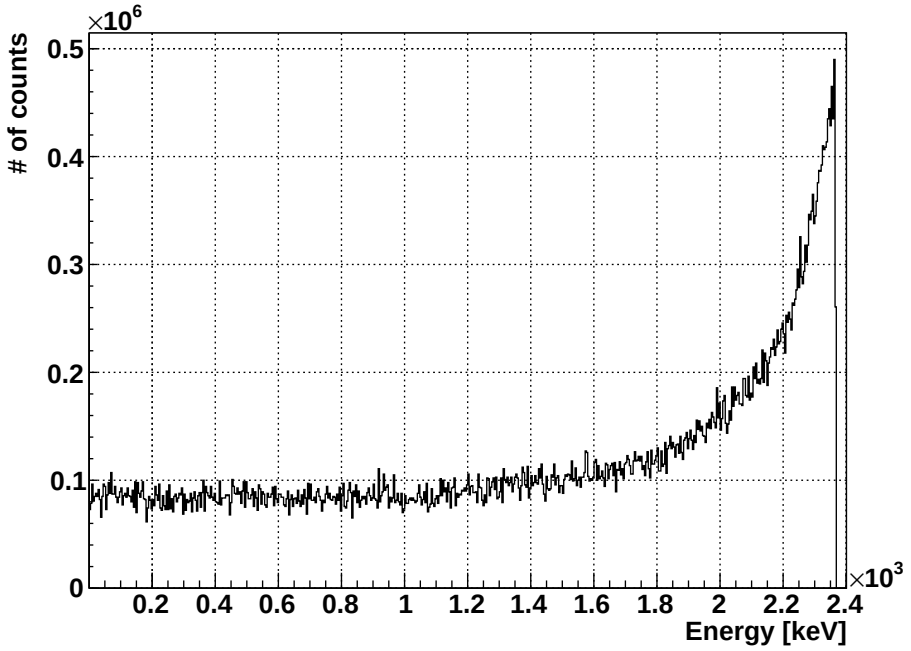

(a) decay0 spectrum

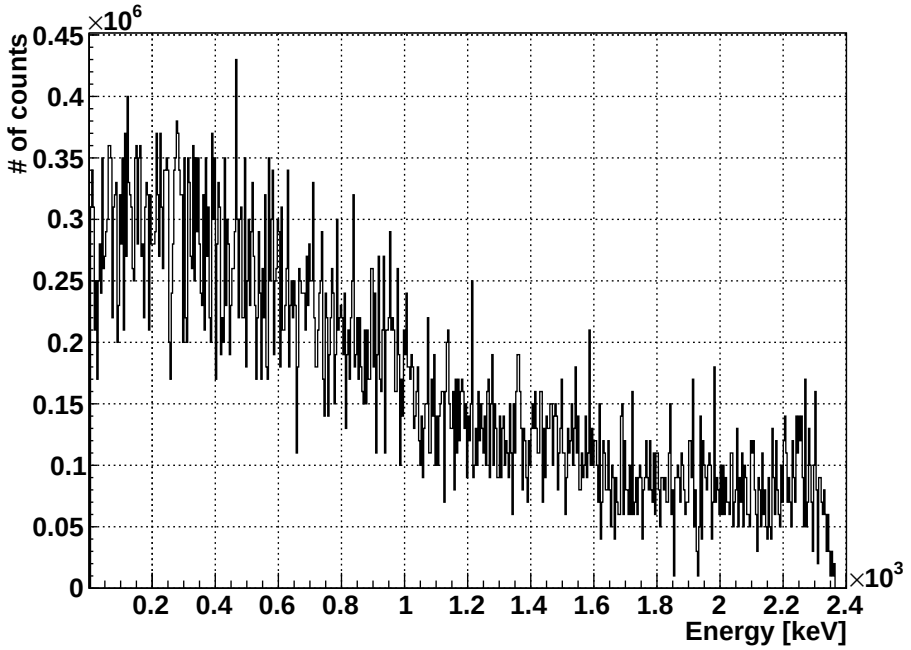

(b) simulated spectrum

Figure IV.15: The Compton electron spectrum; (a) the theoretical shape and (b) the spectrum as detected within the sensor layer of a Timepix detector (simulated using ROSI). The high edge at the end of the spectrum is cut as a lot of electrons escape from the sensor.

Background data

As the measured spectrum was not in full correspondence with the expectations, we took data from the background radiation. This means we removed the ^{232}Th source but left the rest of the experiment unchanged and observed the radiation with the detector for 277 hours. The spectrum is shown in two parts on figure IV.16 - (a) is the low energy spectrum and (b) is the electron spectrum.

At a first glance, surprisingly, the Cadmium and Telluride fluorescence peaks are in the spectrum, which means that there is a lot of X-ray radiation hitting the sensor layer. The same radiation is probably responsible for the large amount of background electron events as well. Still it does not explain the gradient in the electron spectrum of the measurement as its contribution is rather low. The background does provide only about 1.5 % of the events in the interesting region whereas an event frequency of about 45 % is required to explain the unusually Compton spectrum by background events. In fact, the background radiation rates are at the level of natural radiation and even lower.

Since the experiment was carried out in a radionuclide laboratory and the detector was inside of a cardboard the contamination by α-particles was really low. We measured 378 α-particles in 277 hours, what is a rate of 1.22 $\frac{\text{events}}{h}$. This is much lower compared to the natural radiation rates which we measured in a small lead chamber (312.5 $\frac{\text{events}}{h}$).

Comparison between simulation and experiment

Because of the discrepancies between the simulation and the experiment considering the spectrum, we compared the criteria which are used for the event identification by the ANNs between the simulation and the experiment. On figures IV.17 and IV.18 these ten criteria are shown in the integrated form; red always the simulation and blue the experiment. We used a combination of Compton electron and pair production events in a 1:1 ratio (according to the experimental data) for the simulated data.

The matching is not perfect for all criteria but pretty good for criteria 8 and 10. We want to point out criteria 5 and 8 which are the number of pixels (C5) hit during an event and the distance between the energetic center of mass and the spatial center of mass (C8), respectively. As the experimental data curve is shifted to the right in the first case (more pixel are usually hit) and to the left in the second case (the centers of mass are usually nearer together), we assumed that a part of the discrepancy comes due to the isotropic angle distribution of the electrons in the simulation; however, in the experimental setup the photons invaded the sensor only from one direction (parallel to the sensor layer's surface) and therefore particular angles are favoured. If we adjust the simulation according to this, the matching gets better as shown for C5 on figure IV.19.

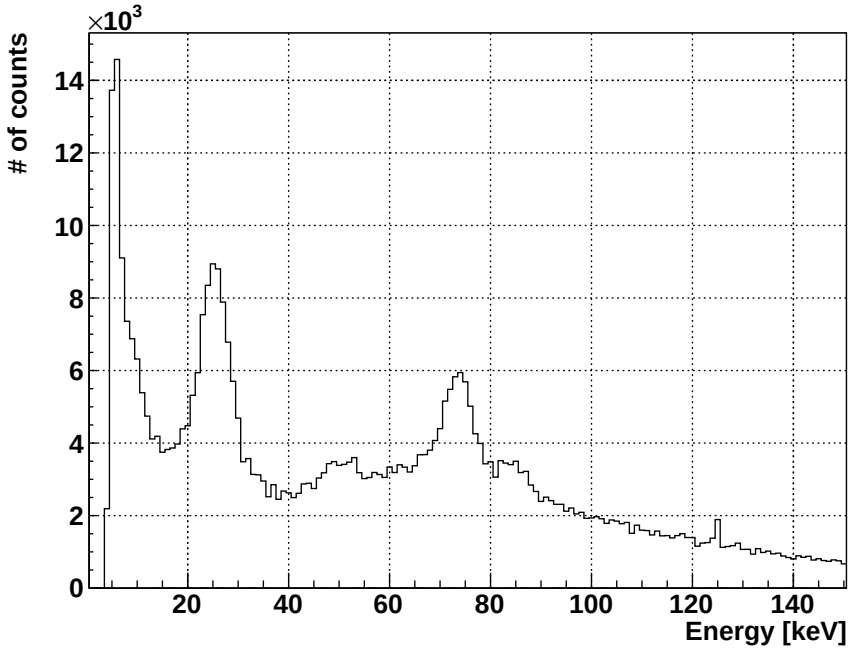

(a) low energy, single-clustering

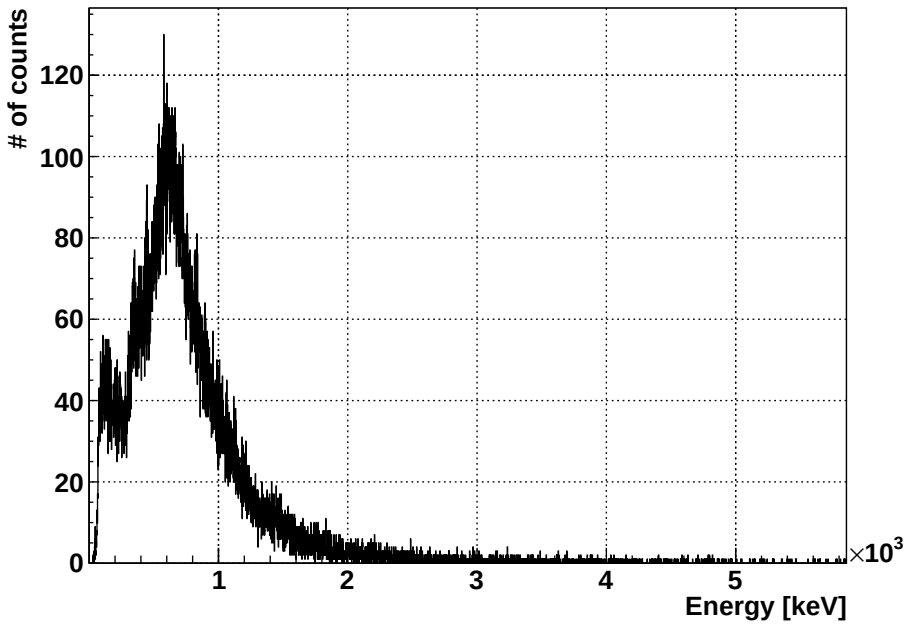

(b) electron spectrum

Figure IV.16: The (a) low energy and (b) the electron spectrum of the background measurement (277 hours of data).

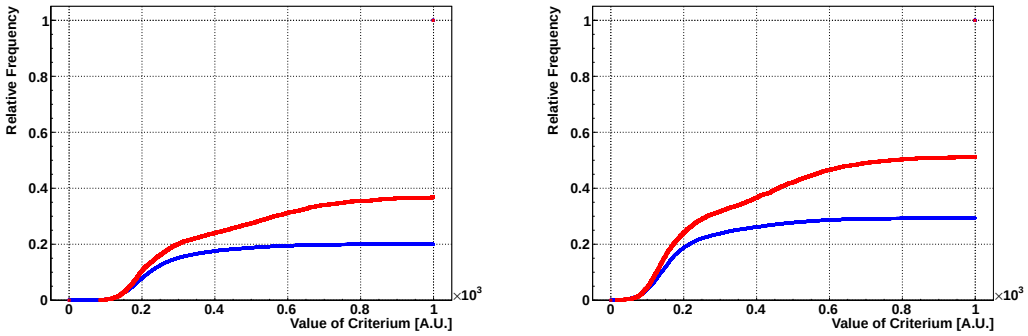

(a) C1 (b) C2

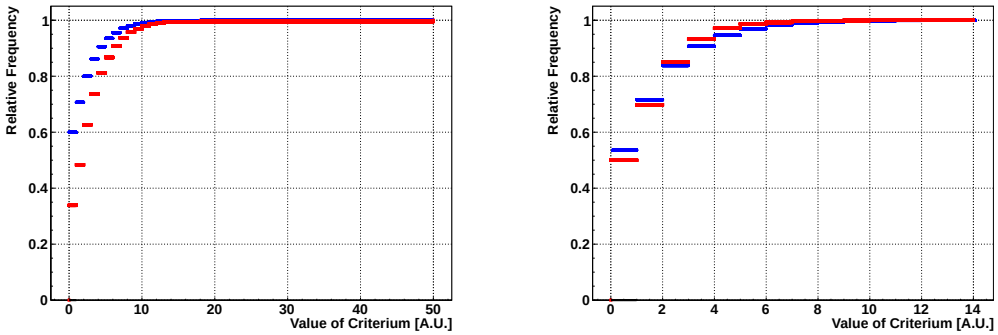

(c) C3 (d) C4

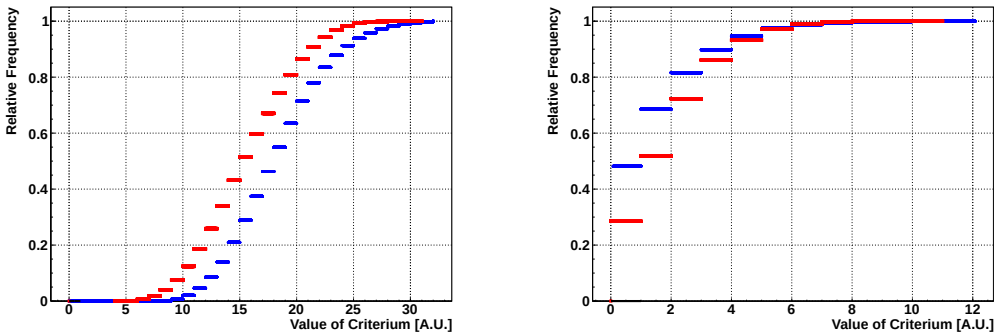

(e) C5 (f) C6

Figure IV.17: Criteria 1-6 used for the event identification; (red) for the simulated and (blue) for the experimental data. Details on the criteria can be found in [29].

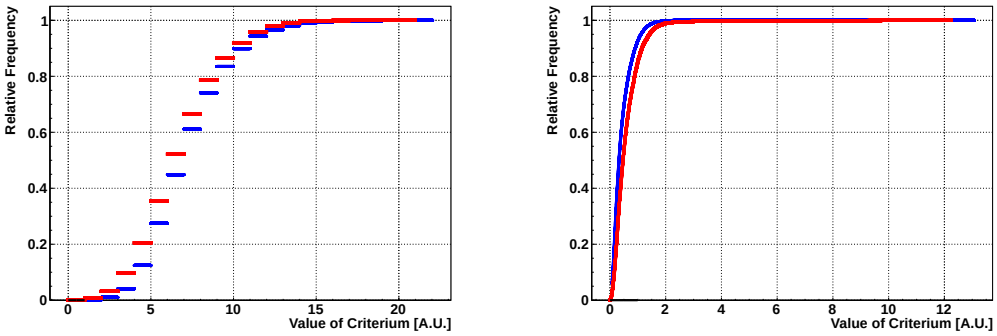

(a) C7 (b) C8

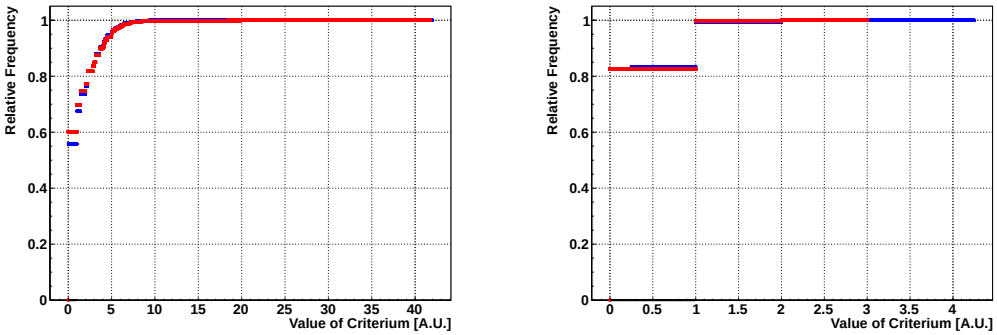

(c) C9 (d) C10

Figure IV.18: Criteria 7-10 used for the event identification; (red) for the simulated and (blue) for the experimental data. Details on the criteria can be found in [29].

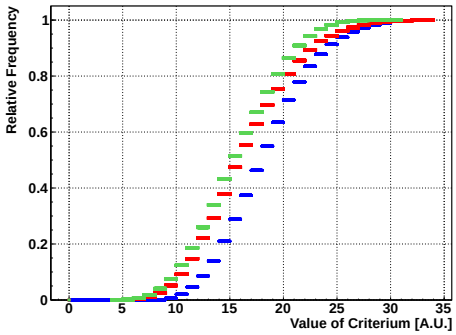

Figure IV.19: Criterium 5 (the number of pixel hit during an event) for the initial simulation (green), the adjusted simulation (red) and the experimental data (blue). The matching improves by the adjustment.

The Compton and pair production spectra

Finally, we will discuss our main aim. It was to discriminate two electron events from single electron background. On figure IV.20 (a) the mixed spectrum of single electrons and pair production events (i.e. the original spectrum after rejecting α, muon and low energy γ background) in the range r = [1300 keV; 2000 keV] is shown. In this range the ANNs were applied to the experimental data. As every network can operate most effectively only in a particular energy range, we divided r into 8 equal intervals of 200 keV size each. For every interval an individual network N_i was trained and an optimal cut parameter c_i, which will be explained in the next paragraph determined. We did not apply the ANNs to events of lower energy because for both single and two electron events the tracks are rather short and too few pixels are hit. Thus, the graphical pattern are not really distinguishable and a reliable identification cannot be performed. As the peak belongs mainly to the pair production events and the long continuum to the Compton scattered electrons, we expect our networks to separate these parts of the spectrum from each other.

The single electron and the pair production spectra are shown on figure IV.20 (b) separated from each other and stacked. Every event of the mixed spectrum was classified by the appropriate network N_i (according to the event's energy) and assigned a rating R. R can take values between 0 and 100. The cut parameter c_i divides this interval in two parts. If the rating of an event R is smaller than the cut parameter c_i, it is classified as a single electron event and vice versa. According to this valuation all events were sorted into the single electron or the pair production spectrum. The sharp edges are at the interval borders of every network. The reason for these abrupt jumps is, that we haven't taken the classification performance of the ANNs into account yet.

The value R is not a real physical quantity and does not describe the probability of an event being a two electron event. In fact, for every cut value c the network classifies a particular percentage of the single electron events correctly (we will call this quantity π_1) and a particular percentage of the two electron events (π_2). These values are known from the network training process. If we call the real number of single electron events η_1 and the real number of two electron events η_2, then the number of events identified as two electron events κ_2 can be computed the formula

$$\kappa_2 = \pi_2 \cdot \eta_2 + (1 - \pi_1) \cdot \eta_1. \tag{IV.12}$$

The first summand is the number of correctly classified two electron events. The second summand is the number of misclassified electrons which are added to κ_2 incorrectly. κ_2 is of course nothing else but the number of entries in every energy bin of the pair production spectrum histogram. By inverting formula IV.12 we can calculate the real number of two electron events η_2:

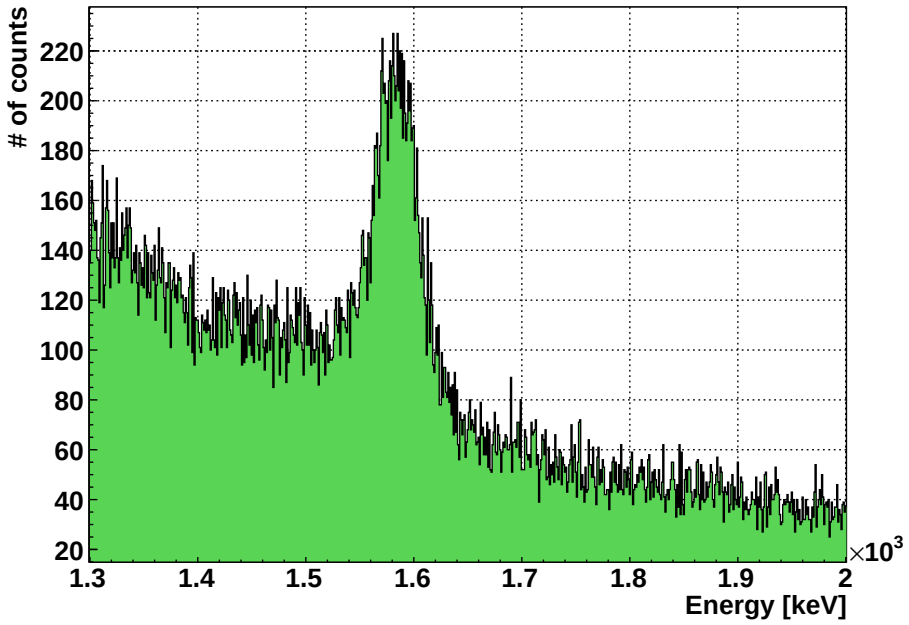

(a) before event classification

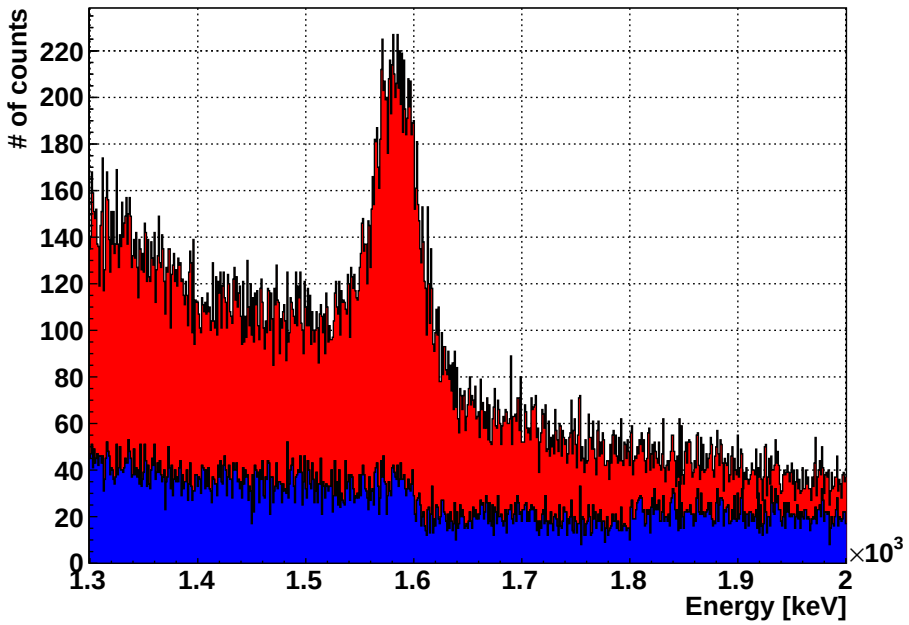

(b) after event classification

Figure IV.20: The electron spectrum in the region of interest (a) before and (b) after event classification by the ANNs.

$$\eta_2 = \frac{1}{\pi_2}(\kappa_2 - (1 - \pi_1) \cdot \eta_1) \tag{IV.13}$$

The real number of single electron events η_1 is then $\eta_1 = N - \eta_2$, where N is the total number of events. The recalculation is done for every energy bin and the high fluctuations between the bins are smoothed by using the average value over the next five neighbours of every bin instead of only the value in the bin. The results of this recalculation are shown on figure IV.21 (b). The single electron spectrum (blue) now consists only of the Compton spectrum and the two electron spectrum (red) contains only the pair production peak. This is consistent with the physical expectations. The remaining red events below the peak energy are probably pair production events where at least the electron or the positron escaped the sensor layer and therefore not the full peak energy is detected for the event.

At last we want to emphasize on the fact that the recalculated spectra are consistent with the expected physics but the events in the particular spectra (single electron and two electron) are inserted in randomly from the mixed spectrum only according to the calculated numbers η_1 and η_2. (You do not refill the events from the single electron into two electron spectrum or vice versa due to some criteria.). If you choose one point in the spectrum, it is unknown whether it belongs to a particular single or two electron event. Nevertheless the correct spectrum reconstruction is a good evidence for correctness of the simulation used to train the networks and the misclassification errors of the ANNs obtained in the training process.

Although the recalculated spectrum does not contain any information about particular events, it can be used to calculate the probability for every particular event to be a single or two electron event. To perform this task additional information about the network performance for every possible cut value c_i is necessary. This performance has been evaluated for simulated data but has not compared to experimental data yet [37].

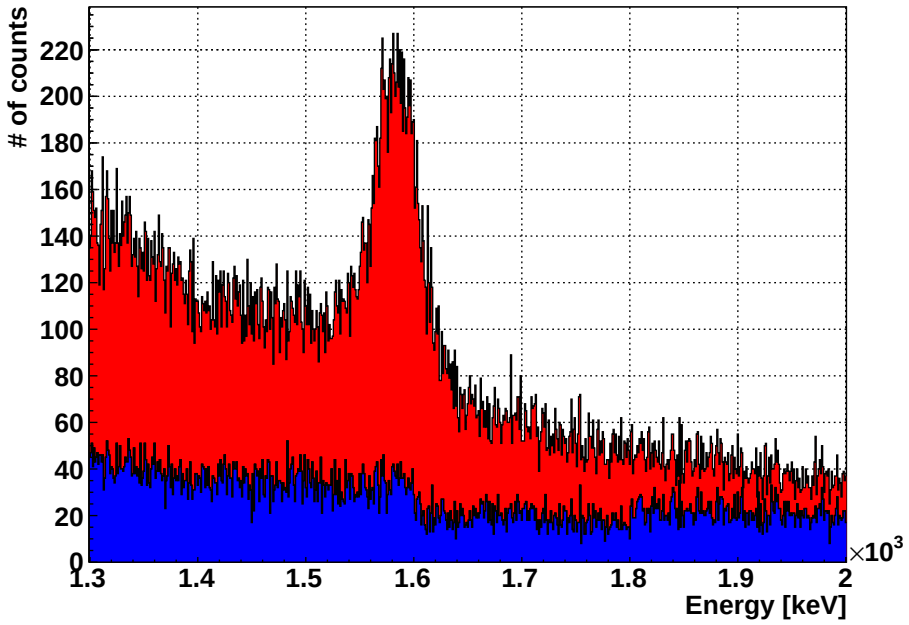

(a) before

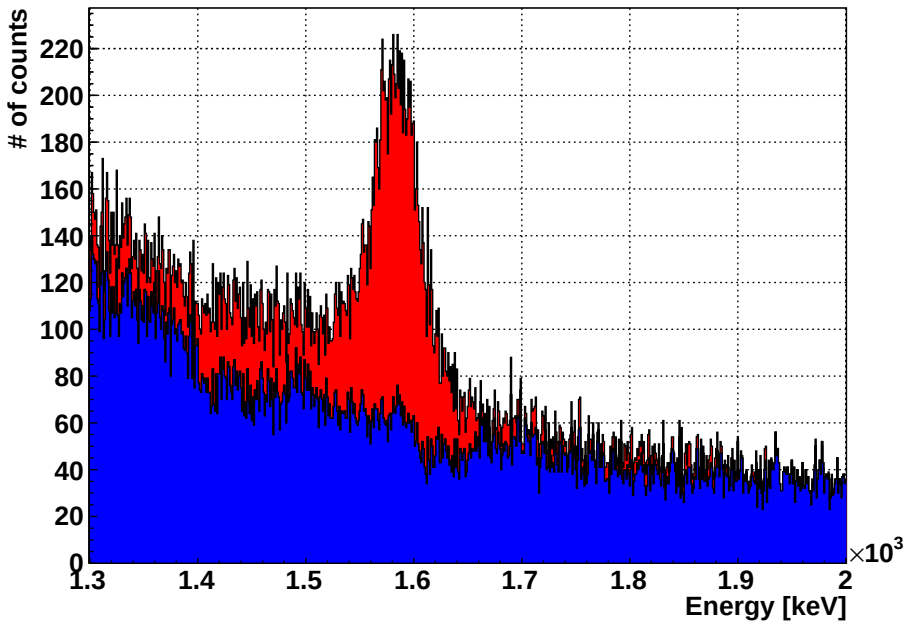

(b) after

Figure IV.21: The electron spectrum in the region of interest (a) before and (b) after taking into account the classification errors of the ANNs.

IV.3 Energy resolution for tracks

For particle energies larger than 150 keV the energy is most likely not to be detected in one pixel but to be detected in several pixels. As the pixels can be treated as independent little calorimeters, we expect the energy resolution at a particular energy E_0 for tracks to improve according to the formula

$$\frac{\sigma_T}{E_0} = \frac{\sigma_p}{\sqrt{N}E_0}. \tag{IV.14}$$

σ_T is the energy peak width for the whole track, σ_p is the energy peak width in one pixel at the energy which is most probable to occur for a particular kind of track and N is the number of pixels in the track. Indeed, this is only a rough approximation and won't be valid for precise measurements but generally represents a very important idea: The energy resolution increases with the number of pixels in the tracks because of an averaging effect over independent measurement cells. Therefore we measured the energy resolution of electrons caused by γ-radiation of ^{137}Cs at 661.5 keV and of ^{208}Tl at 1588.53 keV in order to observe this effect.

IV.3.1 The energy resolution for tracks at 661.5 keV

Often the 661.5 keV line of ^{137}Cs is used to calibrate and characterize spectroscopic detectors. In order to compare the energy resolution quality of the 110 μm Timepix to other detectors, we measured the energy resolution of this line. The complete electron spectrum (after removing α-particles, muons and low energy photons) is shown on figure IV.22 where you see the Compton spectrum and the photo peak. We measured an energy resolution of 1.9 % at the photo peak. As the probabilty for the electrons to escape is now much lower, the full, expected Compton spectrum can be seen. This is in good quantitative correspondence with the simulation results.

IV.3.2 The energy resolution for pair production events at 1588.53 keV

As next we investigated the energy resolution at the pair production peak. If we fit the bare peak, the energy resolution is 2.2 % but also the peak position is shifted. The reason for this are the extrapolation errors in the calibration curve. In fact, they do not only shift the peak position but do broaden the peak as well. This can be illustrated by the following procedure:

Since we know that the calibration errors increase with the energy (see previous chapter), we can try to leave away events which have at least one pixel with an energy deposition higher than a particular threshold energy E_{cut}. If we start with $E_{cut} = 200$ keV

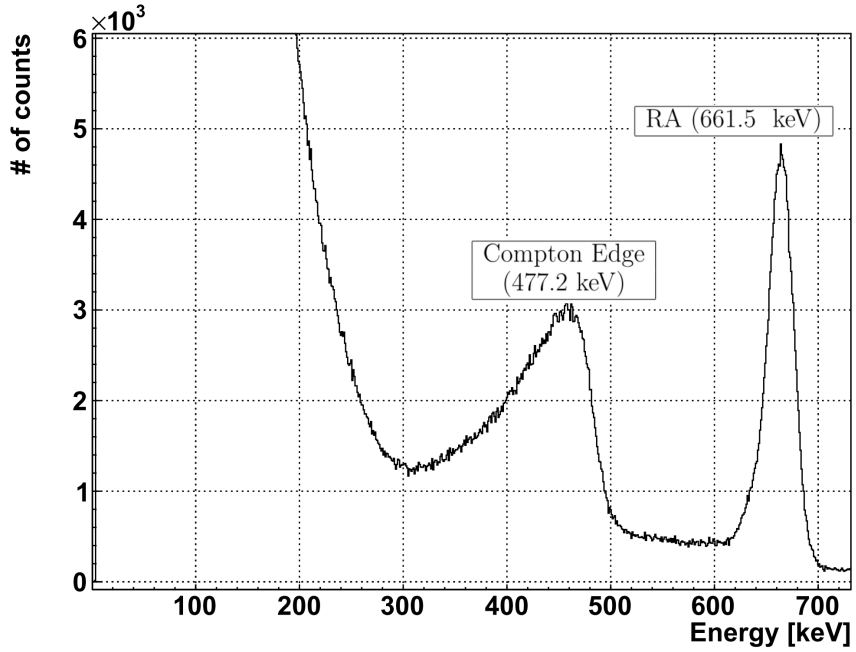

Figure IV.22: ^{137}Cs - clustering spectrum. The abbreviations are the origin of the peaks: RA - γ-line of a radioactive emitter.

the peak will vanish completely. By going to higher threshold energies, first, the peak will reappear and then it will start to get broader. The broadening is caused by the fact that for tracks with lower energy deposition a peak is produced at lower energies and on the opposite for tracks with higher energy deposition a peak is produced at higher energies. This is illustrated on figure IV.23 (a) and (b). The left figure shows the peak for $E_{cut} =$ 330 keV and the right figure shows the peak if all events with energy depositions above 390 keV are left out. The distance between the means of the two peaks is about 30 keV (!). All such peaks overlay and produce a wide peak which limits the energy resolution.

Figure IV.24 (a) shows the energy resolution at the pair production peak plotted against E_{cut} and figure IV.24 (b) the position of the peak which is constantly shifted to the right - the peak is shifted and broadened. We can achieve an energy resolution of about 1.2 % if events which are affected by the calibration errors too much are sorted out. Thus the energy resolution of the detector at this stage is clearly not limited by the detector physics but by the calibration mistakes; especially concerning events with high energy depositions.

The first attempt to solve this problem was to apply the linear correction function obtained in the previous chapter and as we can see the peak is shifted very much to its right position at 1588.53 keV. Figure IV.25 shows the peak before (red) and after (blue) the correction. The energy resolution is enhanced by 37.5 %, from 2.2 % to 1.6 %. An energy resolution of 0.54 % as proposed by the simulation could not be achieved. This is because the correction is done for the whole matrix but not for every pixel individually.

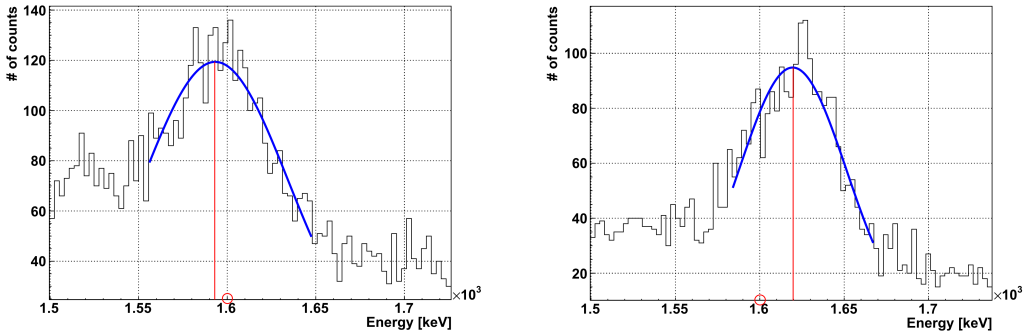

(a) < 330 keV **(b)** > 390 keV

Figure IV.23: The shift of the pair production peak due to calibration errors. On (a) only events with a maximum energy deposition in one pixel below 330 keV and on (b) only events with a maximum energy deposition in one pixel above 390 keV are taken into account.

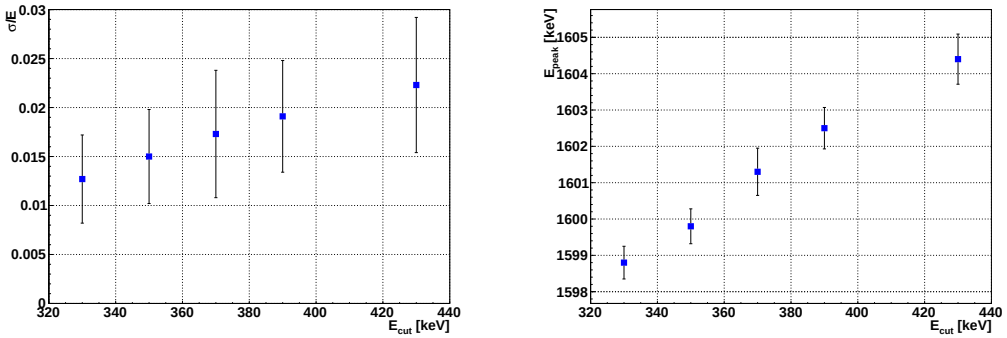

(a) energy resolution **(b)** peak position

Figure IV.24: The energy resolution (a) and the peak position (b) of the pair production peak plot against E_{cut}. You can see clearly the trend: The peak is shifted to the right and broadened. The error bars on plot (a) are huge because the fit is done with poor statistics since many events are left out due to the energy cut.

Basically, by the linear correction the mean of the ΔS distribution is shifted to its right position but its width is untouched and hence remains the same. Consequently, the energy resolution is not enough enhanced by the global linear correction to reach the theoretical limits.

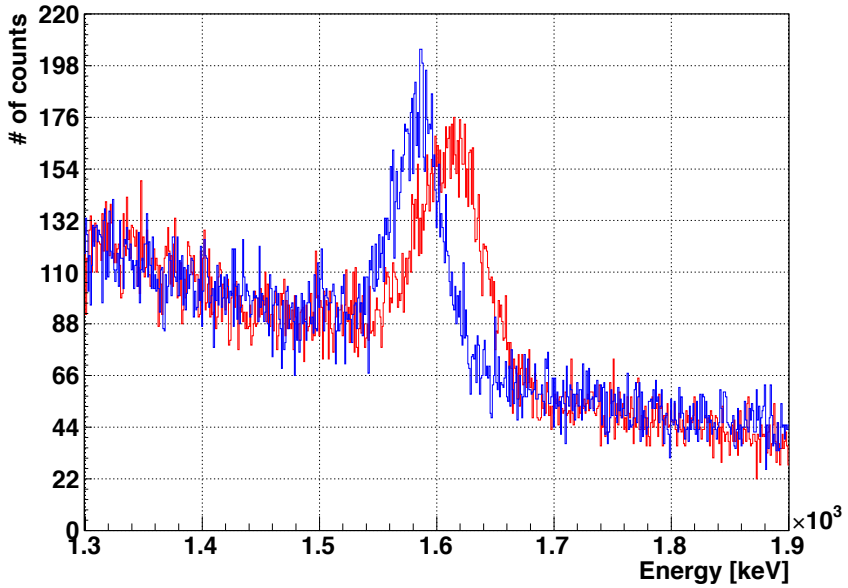

Figure IV.25: The pair production peak (red) before and (blue) after applying the linear correction. By the linear correction the peak is shifted to its right position and the resolution is increased from 2.2 % to 1.6 %.

IV.4 Summary

By the experiments and analysis carried out within the scope of this thesis we could show that tracking can be used to eliminate α and muon background with a very high efficiency. In fact, if tracking is applied α and muon background are not a problem any longer and actually much less passive shielding is necessary as such events can be rejected afterwards by the track data analysis.

The big challenge of distinguishing between one and two electron tracks was only partially successful. The predictions of the simulations for the ANNs could be proven right but the ANNs were not able separate the Compton spectrum from the pair production peak completely. Only after the classification error analysis the spectra can be reconstructed properly. However, by doing so it is impossible to trace every point in the spectrum back to a particular event afterwards. Therefore it is arguable if the technique of ANNs is appropriate for the final $0\nu\beta\beta$ experiment. The main problem is that a lot of statistics is required to gain a good reconstructed spectrum. As we expect only a few events in the experiment, the ANNs have to be adjusted in such a way that they can perform a reliable classification for poor statistics. By the comparison between the criteria found in

the simulated and in the experimental data we could understand the simulation better and bring the criteria to a better match.

The energy resolution that we obtained for electron tracks at 661.5 keV was 1.9 %. The energy resolution for electron tracks at 1588.53 keV was 1.6 % if all tracks are considered and 1.2 % if only tracks with an energy deposition below 330 keV are taken into account. The prediction of the simulation which is 0.54 % was not achieved. We think the main reason is the broadening of the peak by the calibration mistakes. The detector is calibrated with γ-radiation up to 122.06 keV and is reliable up to this energy. If the calibration curve has to be extrapolated to high energies, the error increases with the energy and all measured tracks usually contain at least one pixel with an energy deposition higher than 300 keV. It is very likely that the energy resolution could be enhanced with a better calibration for high energies.

V Conclusions and Outlook

The first main aim of the thesis could be achieved - the calibration of a 110 μm CdTe Timepix detector was performed successfully; both global and pixel-by-pixel. Only about 0.3 % of the pixels had to be sorted out and therefore the automatization is considered to be robust. The calibration can be performed with fluorescences and radioactive sources effectively down to about 6 keV and up to about 136 keV. A problem with high energy photons up to 661.5 keV is that although they have feasible detection effeciencies, most of the statistics is lost because of two effects: a) High energy photons produce lots of Cd and Te fluorescence and escape photons. Hence statistics is bad at the full energy peak. b) Energies up from 120 keV are more probable to be deposited in more than one pixel. Therefore a cluster analysis is necessary (like in the case of ^{137}Cs) to reconstruct the spectrum correctly and most of the statistics cannot be used for a single pixel calibration.

The calibration curve is most reliable in the "linear" part (from 40 keV to 120 keV) where the deviations are about 0.5 %. In the non-linear part the deviations are about 5 % and beyond the calibration range the deviations grow with the energy. This effect causes a significant shift for events at high energies (about 6 keV at 357 keV and about 20 keV at 1588 keV). We could apply a first order correction function to eliminate this effect.

For the energy resolution of single pixel hits a limit value (for infinitely high energies) of 1.1 % was measured. The energy resolution at the highest calibration point (122.06 keV) was 2.6 %. The energy resolution can be enhanced by optimizing the DAC settings and increasing the bias voltage. With lower IKrum (4) and higher bias voltage (700 V) the energy resolution was 3.2 % (instead of 5.7 % with regular settings) at the 59.54 keV peak of ^{241}Am and 2.1 % (instead of 2.6 %) at the 122.06 keV peak of ^{57}Co.

The energy resolution for electron tracks at 1588.53 keV was measured to 1.6 % and is about a factor of 3 worse than expected. The reason are the errors caused by the extrapolation of the calibration curve. As the Prague curve is only a rough empiric approximation for the real calibration curve, the errors are high for energies beyond the calibration range. If 1588.53 keV electron tracks (events in the pair production peak of ^{208}Tl γ-radiation) are considered, almost always some pixels with an energy deposition higher than 250 keV occur and therefore the pair production peak is broadened by calibration uncertainties.

Summing up, we see that a more reliable calibration is required to improve the detector

quality. A possible solution could be to calibrate the detector in equal steps[1] and fit a line through every three points (see figure V.1). Then for instance the red line will be used for energies between E_5 and E_7 and the blue line for energies between E_8 and E_{10}. As the curvature of the calibration curve is changing slowly with increasing energy, the linear approximation will provide much better results if only small intervals are used. The energy reconstruction could be performed individually on every small interval with a higher precision.

Precise equally distant calibration points could be provided by a pulsed low intensity LASER. A scheme for the experimental setup is shown on figure V.2. Between the LASER (1) (with all necessary optics (2)) and the sensor layer (4) a mask (3) with small holes of about 80 μm size is placed. The distance of the hole centers is 440 μm. The mask position is adjusted in such a way that every hole is above a pixel and we have an effective spacing of 4. If the LASER is turned on, every fourth pixel in a row and column is illuminated. The intensity of the laser pulse is adjusted in such a way that the required energy for a particular calibration point is deposited in every pixel during one frame. After the statistics are high enough the intensity is increased to the next calibration point and after one set of pixels was calibrated, the mask is adjusted to the next set of pixels. Instead of a mask a LASER with a focus of 80 μm and precise position adjustion could be used.

The second main topic was the event identification. α-particles, muons and low energy photons can be identified by automatic routines and eliminated as background with high efficiency. The application of artificial neural networks to distinguish between one and two electron events was only partially successful. A significant part of the electron background events could be sorted out and, if classification mistakes of the ANNs are taken into account, the pair production peak and the Compton spectrum can be separated from each

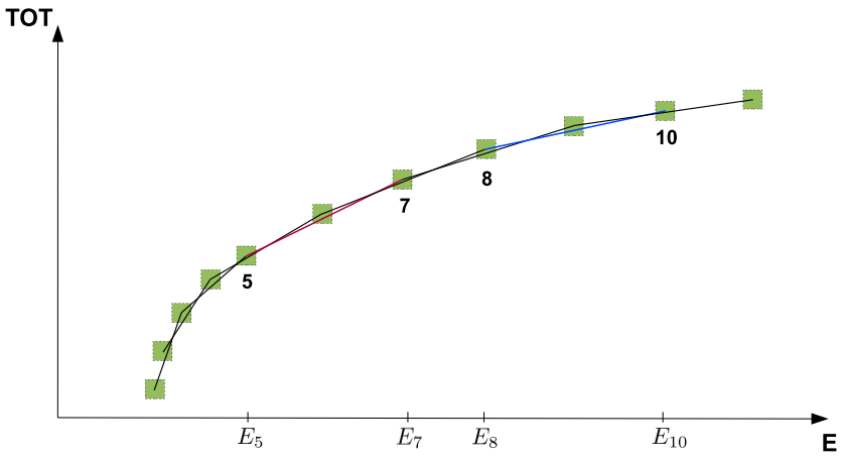

Figure V.1: The idea is to have a lot of sampling points and to fit always between three points to have small intervals in which the linear approximation is fulfilled better.

1 Excerpt for the non-linear part where of course more sampling points are needed.

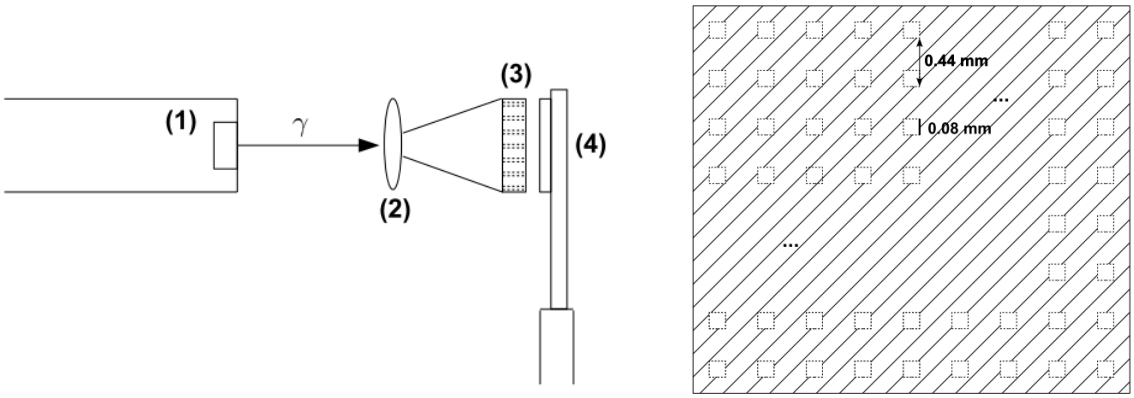

(a) the setup **(b)** the mask

Figure V.2: The experimental setup for the calibration with a LASER (a) and the mask (b); (1) LASER, (2) optics, (3) mask and (4) detector.

other. Nevertheless, for low count experiments (as in the case of $0\nu\beta\beta$ experiments) this way of background rejection is not appropriate by now. It needs huge statistics for a good spectrum reconstruction. It is highly desirable to have a reliable identification for each event individually.

Either the technique of ANNs can be improved or another possible approach to solve this problem could be tested: The usage of Minkowski functionals. According to Hardwiger's theorem Minkowski functionals are a complete basis for any measure M[1] of a vector space $\mathbb{R}^n$. That means that any measure M can be expressed as a linear combination of Minkowski functionals:

$$M^i = \sum_j \nu_j W_j^i \tag{V.1}$$

Here i denotes the tensorial order of the functionals. For i = 0, the Minkowski functionals are scalars and in the case of $\mathbb{R}^3$ can be interpreted as, for instance, the volume and the surface area of the measured topology. A detailed discussion and further information on Minkowski functionals can be found in [38].

Let's fix a particular linear combination, i.e. fix a set of values $\vec{\nu} = (\nu_1,..,\nu_n)$, and calculate the value of the measure M for both one electron and two electron events[2]. As we have two classes of events, we expect two distributions to appear as shown on figure V.3 (the red one for single electrons and the blue one for two electrons). The x-axis is the

1 Here, a measure is a mapping M from the vector space $\mathbb{R}^n$ to a measurement space σ ($M : v \in \mathbb{R}^n \rightarrow M(v) \in \sigma$) fulfilling the conditions of additivity, motion invariance and conditional continuity; see [38].

2 The events can be generated by a simulation, for instance.

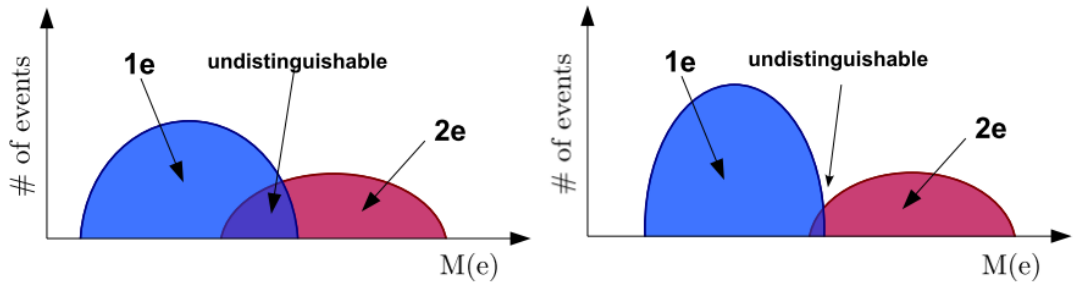

(a) $\vec{\nu}_1$ **(b)** $\vec{\nu}_2$

Figure V.3: The distributions for single (blue) and double (red) electron events. If the set of parameters $\vec{\nu}$ is changed from $\vec{\nu}_1$ to $\vec{\nu}_2$, the shape of the distribution is changed and the area of the overlay between both distributions (purple) can be decreased. The idea is to find an optimal configuration $\vec{\nu}_{opt}$ to minimize the purple area.

value of M(e) for each event e and the y-axis is the number of events with the particular value M(e). If we now want to identify a new event, we can calculate its measure and look whether it belongs to the one or the other distribution. If the events are in the purple overlay area, they cannot be identified uniquely.

As the shape and the position of the distributions can be changed by the choice of $\vec{\nu}$, we can optimize the set of parameters $\vec{\nu}$ in such a way that the puple overlay area becomes as small as possible and therefore a maximum number of events can be identified uniquely. However, we expect the purple area not to vanish completely as there can be events which are not distinguishable because we have a two dimensional projection of the track but not the full three dimensional information. Additionally, the two dimensional projection is limited in its spatial resolution.

Actually, from this point of view it would be rather interesting to analyze which spatial resolution is really necessary to perform a really unique classification of events if unplausible events[1] are not taken into account.

1 Unplausible in this context is referred to events which are theoretically possible but highly unprobable.

A Spectra and Tables

In the first part of this appendix the spectra for various materials which were used within the scope of this thesis are shown. The presented spectra were calculated from the TOT spectra by a pixel-by-pixel calibration. Fluorescence lines are always noted as K_α,K_β, L_α or L_β. PP is the abbreviation for the fluorescence peak and EP is the abbreviation for escape peak (see chapter II). As the Cd and Te fluorescence lines are too narrow to be resolved individually they usually overlay and the Cd and Te PP and EP are always noted together as Cd,Te PP and Cd,Te EP which means the overlay of all fluorescence peaks of Cd and Te or escape peaks of Cd and Te. γ-lines from radioactive decays are abbreviated as RA. If two lines are noted above each other in one box, the peak is an overlay of both lines. If a spectrum is labeled with "material - FL" (for instance Cu - FL), the spectrum is the fluorescence spectrum of this material. If the spectrum is labeled with an isotope name (for instance ^{241}Am), the spectrum is the γ-decay spectrum of this isotope. The working parameters were bias voltage 500 V, THL 190, IKrum 10 and PreAmp 210.

In the second part of this appendix useful data connected to the spectra of the first part is given. The table contains the energy[1] for a particular peak, its origin (i.e. the source of radiation it belongs to), the branching ratio, the detection efficiency and the resolution measured for this peak. The detection efficiency is calculated for a 1 mm thick CdTe sensor layer with a density of $\rho_{CdTe} = 5.85 \frac{g}{cm^3}$.

1 For energies < 300 keV, it is the energy deposition extracted from the ROSI simulation, for higher energies it is the literature value.

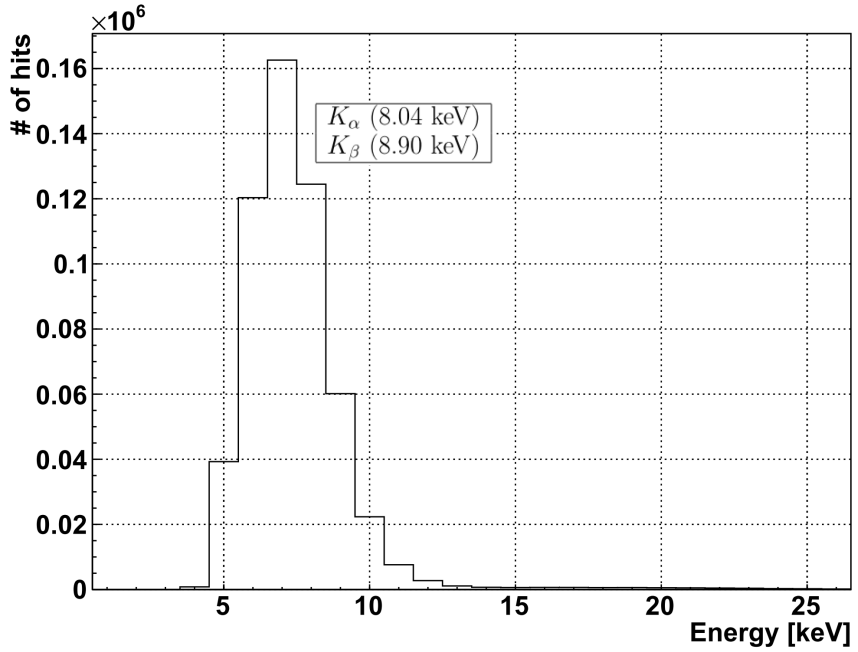

Figure A.1: Cu - FL

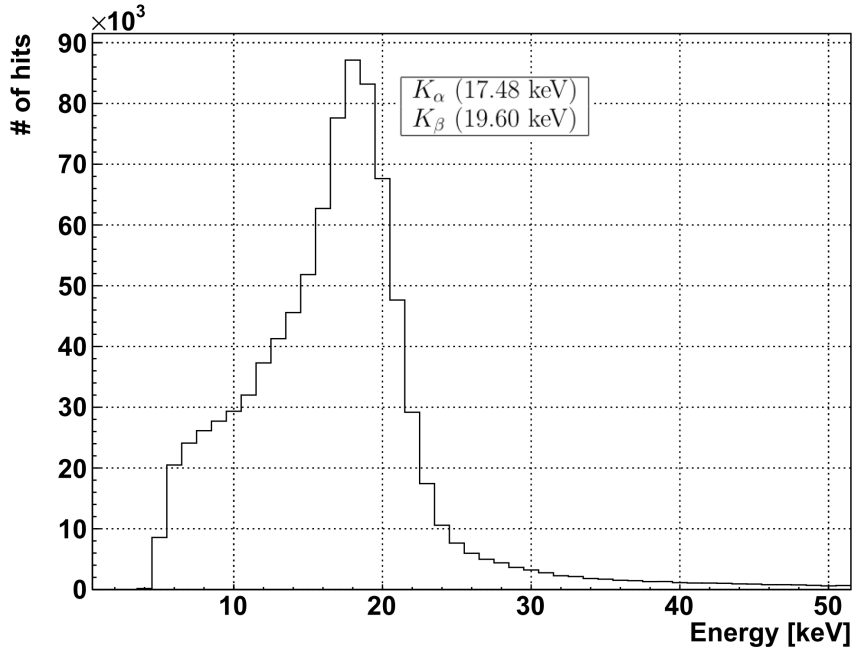

Figure A.2: Mo - FL

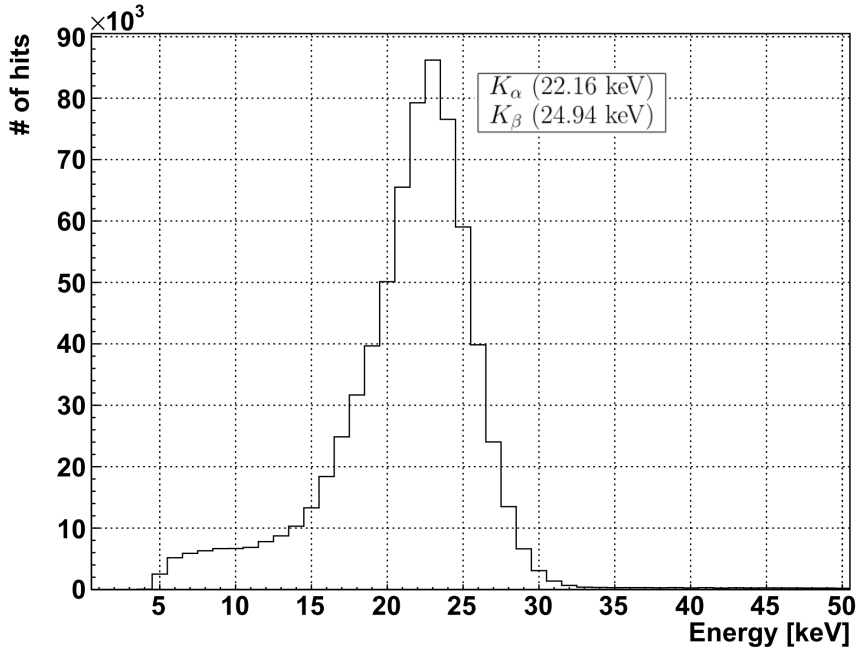

Figure A.3: Ag - FL

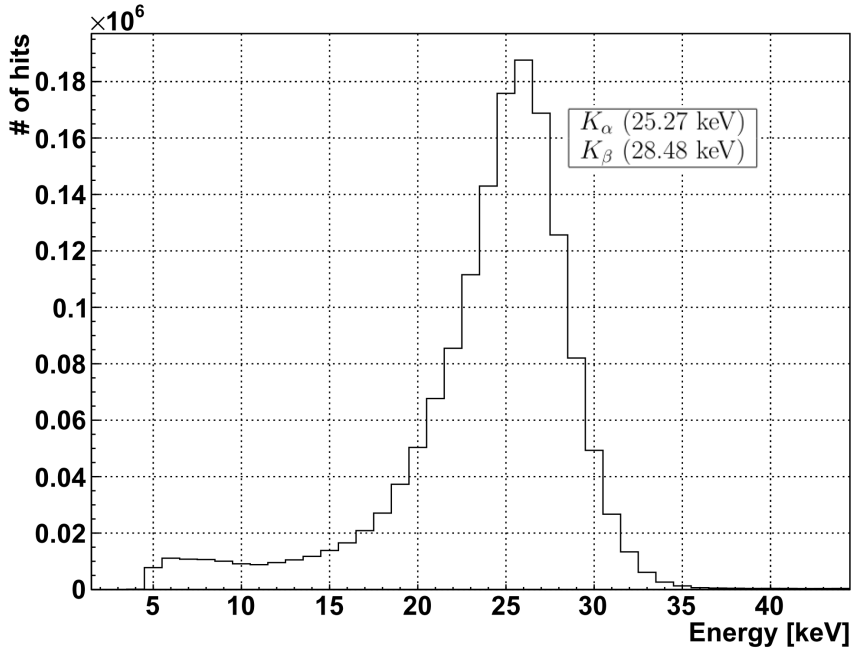

Figure A.4: Sn - FL

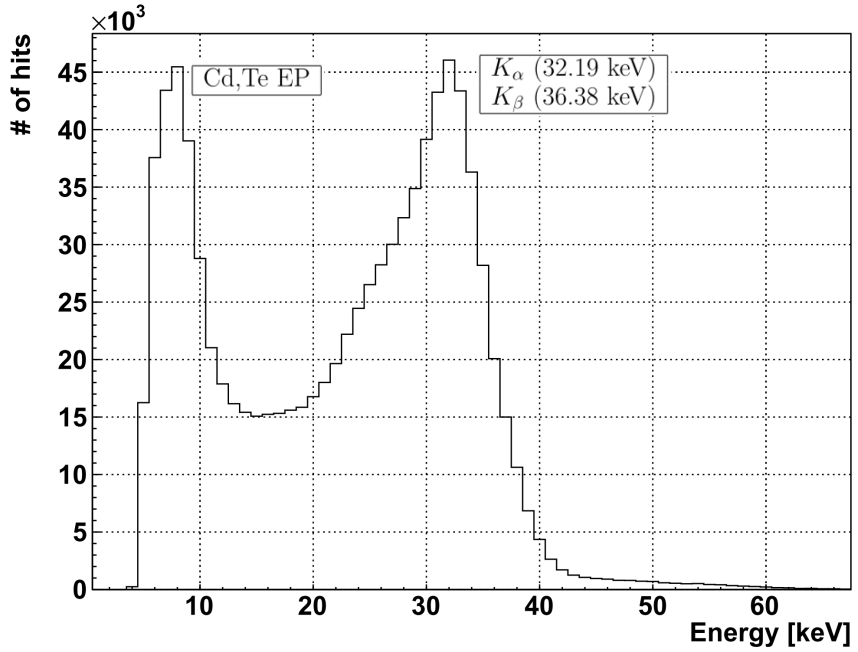

Figure A.5: Ba - FL

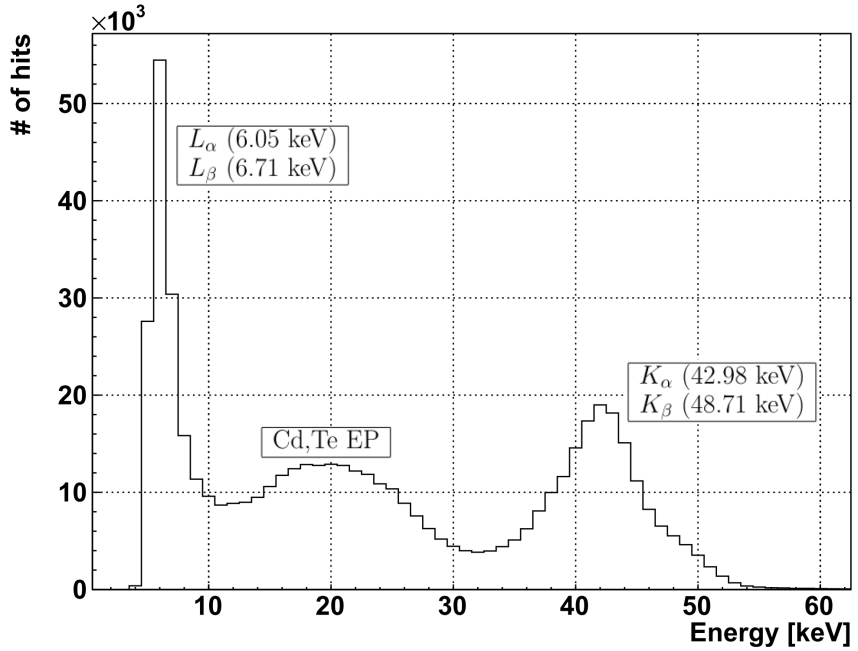

Figure A.6: Gd - FL

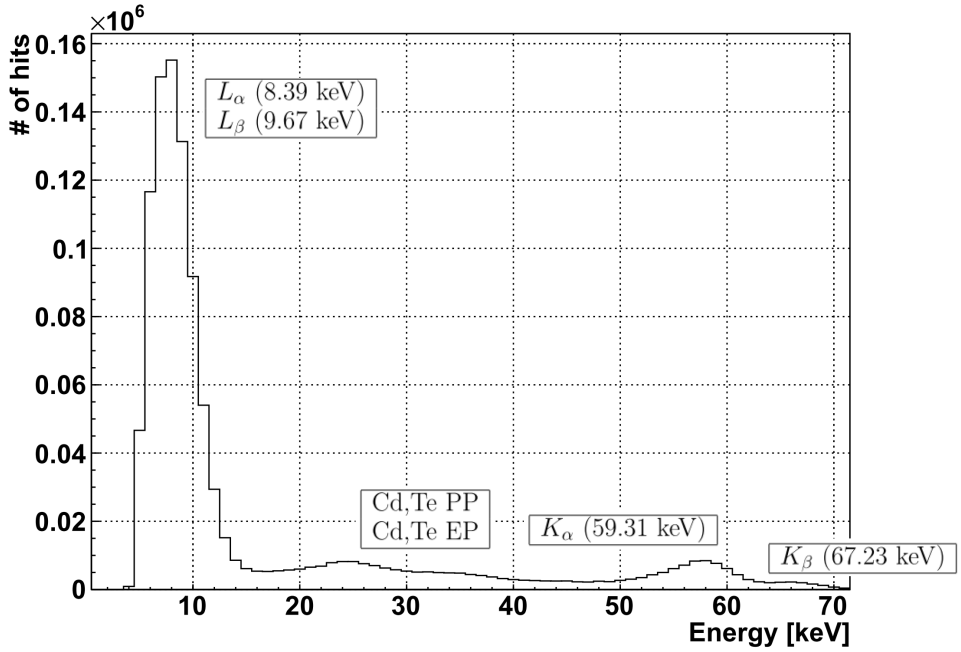

Figure A.7: W - FL

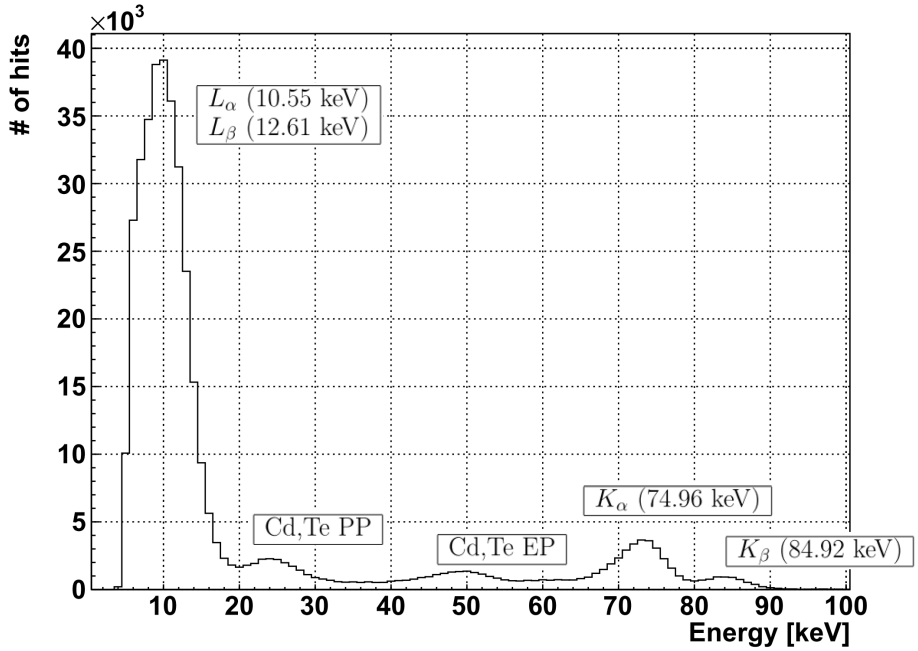

Figure A.8: Pb - FL

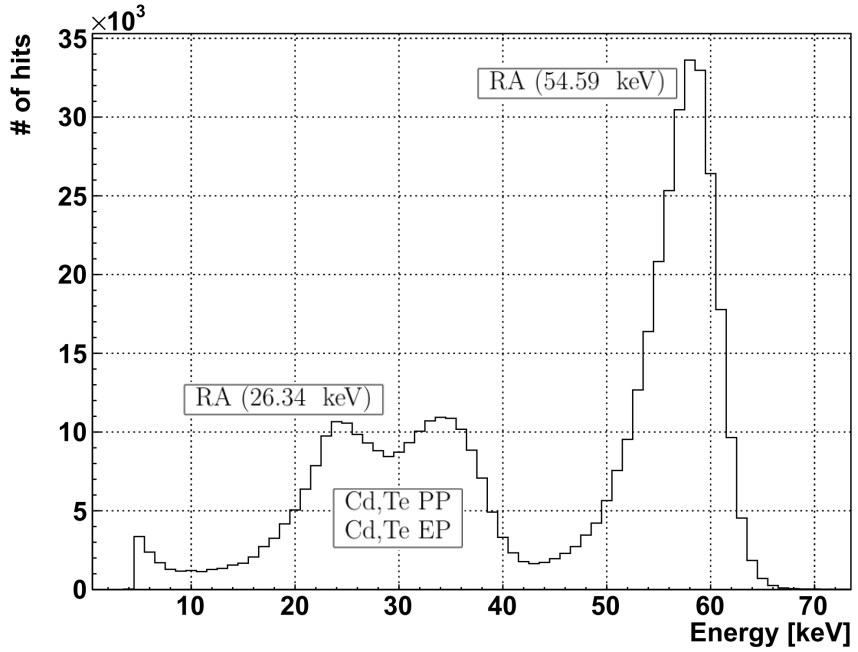

Figure A.9: ^{241}Am

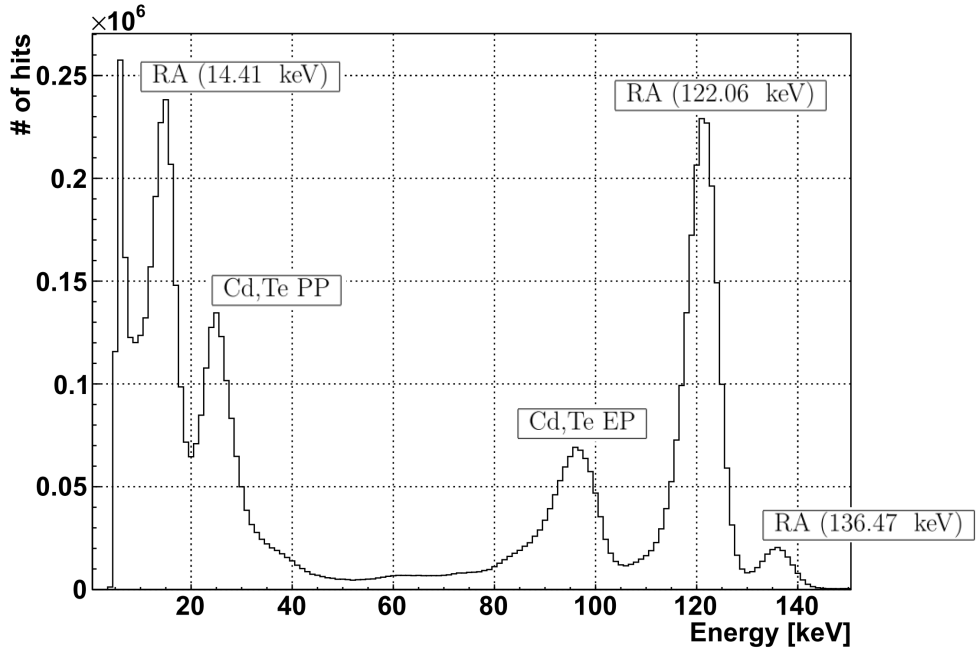

Figure A.10: ^{57}Co

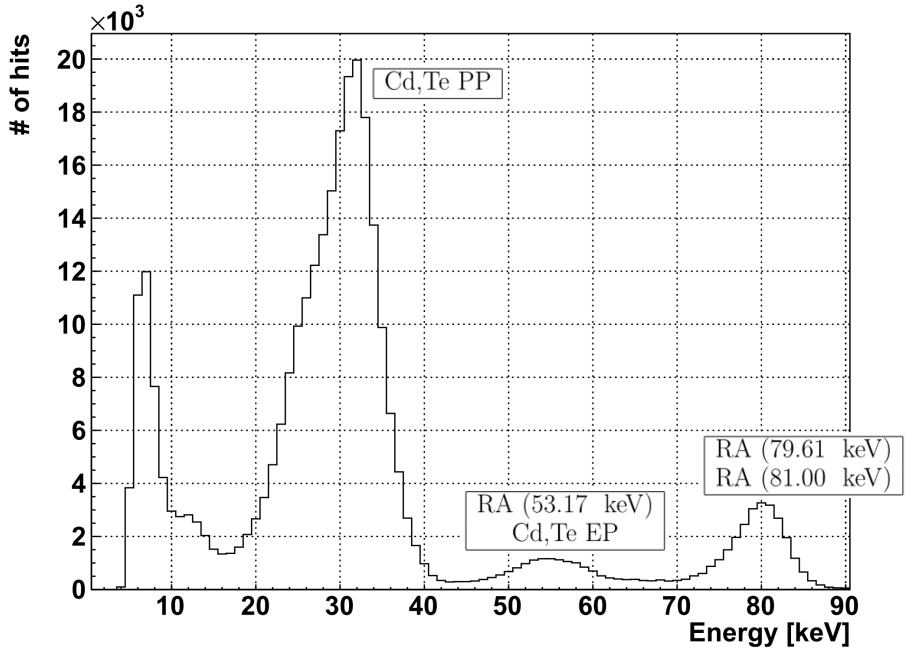

Figure A.11: ^{133}Ba - low energies

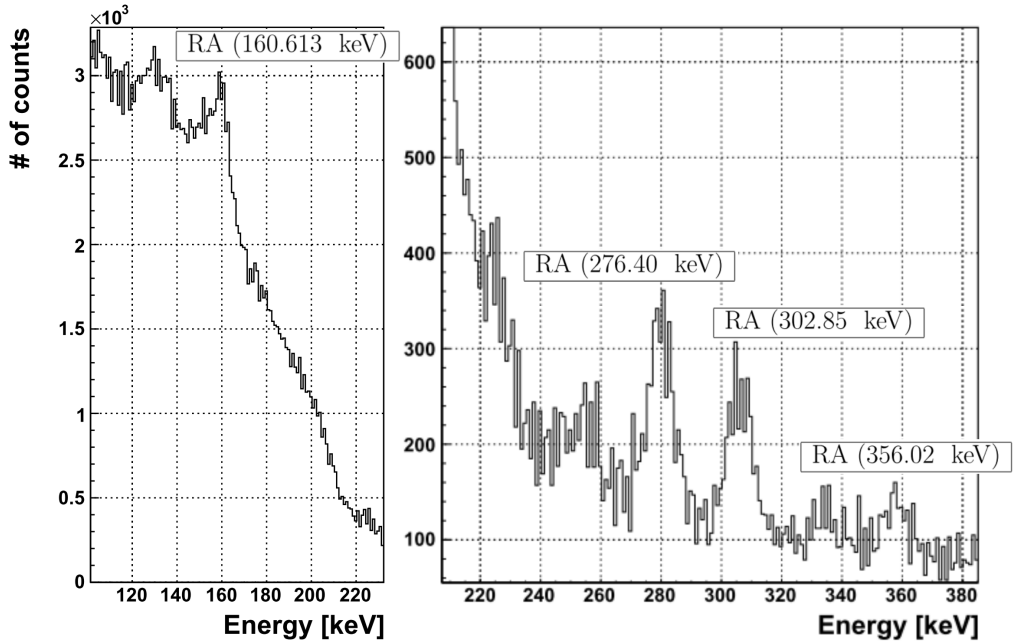

Figure A.12: ^{133}Ba - high energies

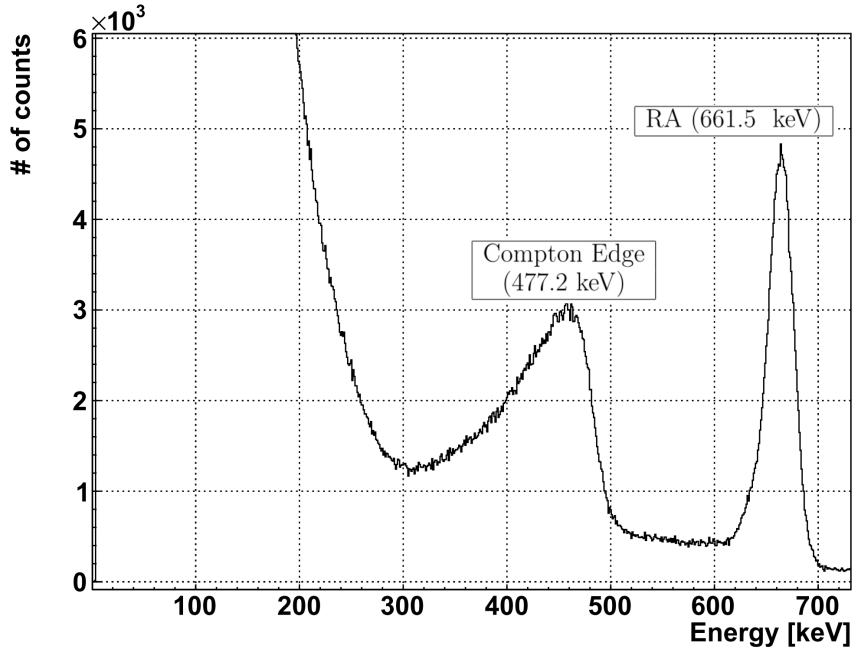

Figure A.13: ^{137}Cs - clustering spectrum

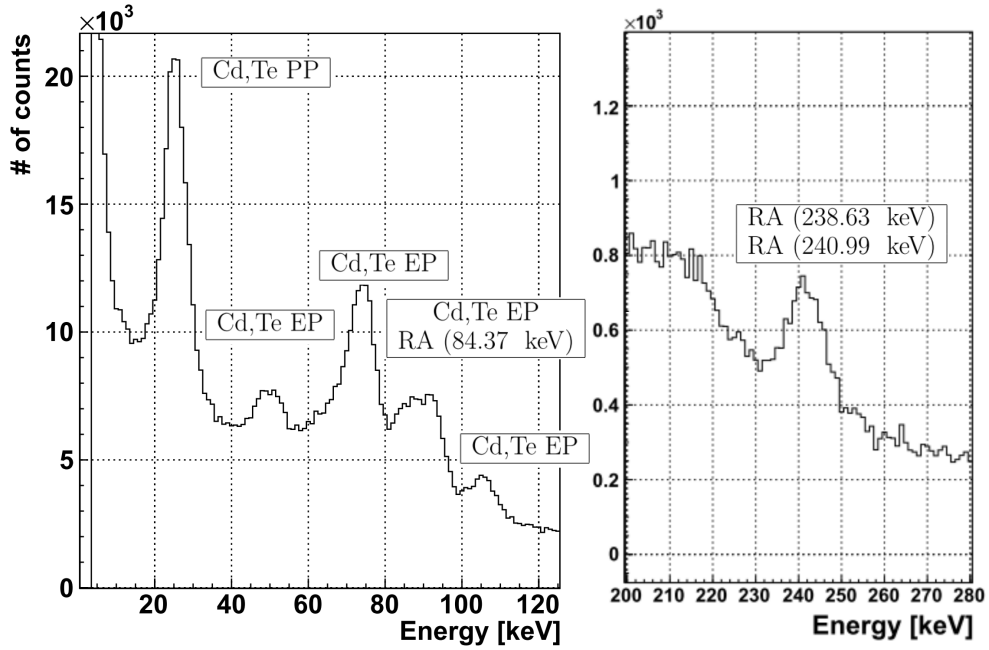

Figure A.14: ^{232}Th - low energy, single-clustering

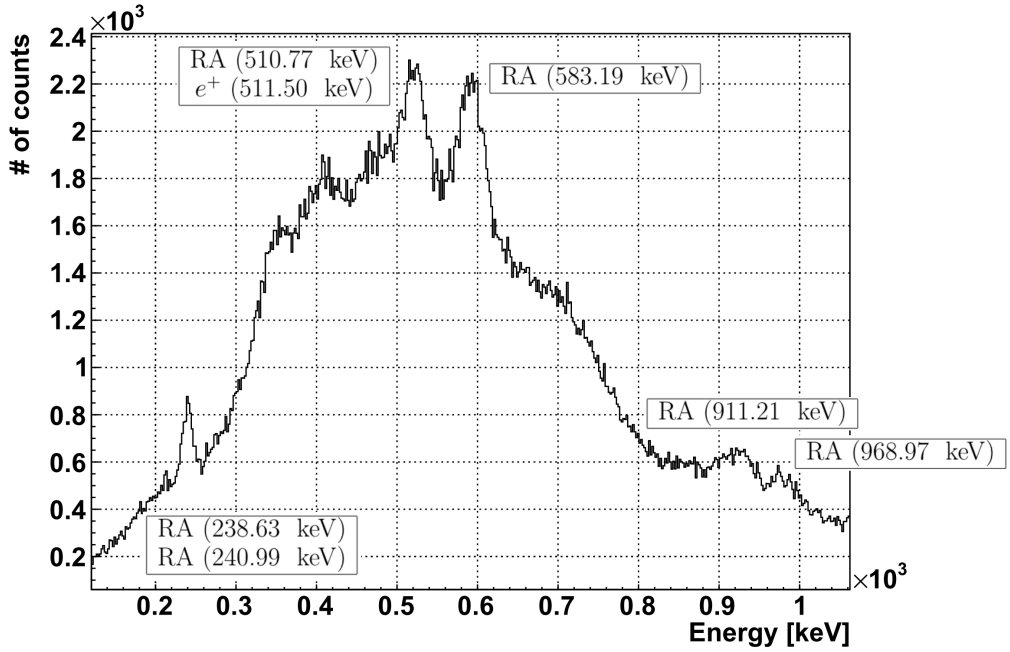

Figure A.15: ^{232}Th - low energy, electron clustering

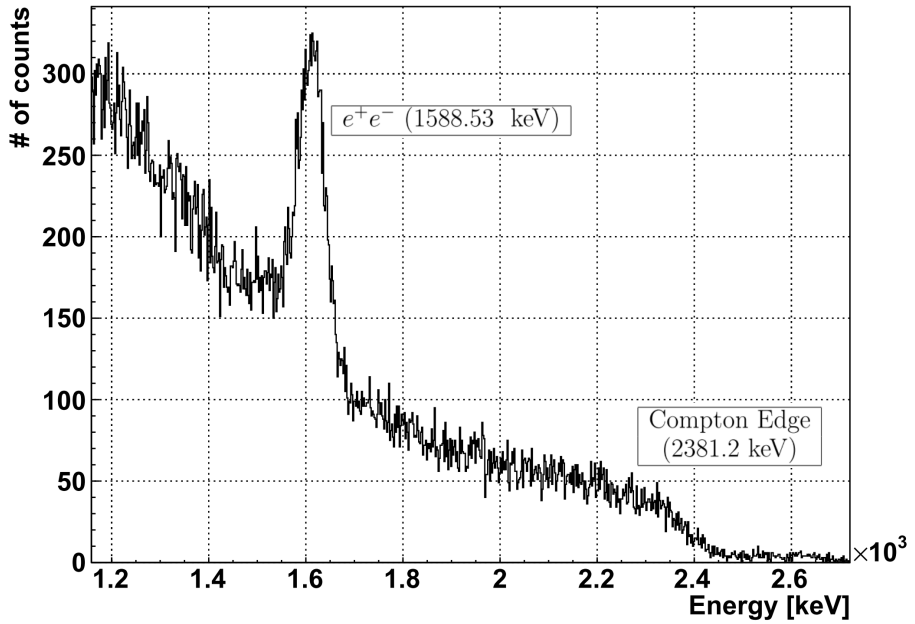

Figure A.16: ^{232}Th - high energy, electron clustering

Material	**Lines**	E_{ROSI} [keV]	Br. Rat. [%]	Eff. [%]	Res. [%]
CuFL	K_α,K_β	7.54	56.69	> 99	20.8
MoFL	K_α,K_β	17.03	76.47	> 99	18.0
AgFL	K_α,K_β	21.55	82.28	> 99	12.8
SnFL	K_α,K_β	24.72	85.73	> 99	11.0
BaFL	K_α,K_β	31.28	95.32	> 99	11.6
GdFL	L_α,L_β	6.43	11.52	> 99	19.1
	K_α,K_β	41.88	91.31	> 99	7.2
WFL	L_α,L_β	7.77	20.69	> 99	29.2
	K_α,K_β	57.99	93.63	> 99	5.2
PbFL	L_α,L_β	9.96	22.74	> 99	30.7
	K_α,K_β	73.03	94.09	87.8	4.6
^{241}Am	RA - 59.54 keV	58.75	35.9	> 99	4.9
^{57}Co	RA - 14.41 keV	13.83	9.16	> 99	18.0
	RA - 122.06 keV	120.84	85.6	38.5	2.5
	RA - 136.47 keV	134.92	10.68	29.9	2.4
^{133}Ba	RA - 80.99 keV[1]	80.09	36.64	80.3	3.5
	RA - 160.613 keV	158.01	0.645	20.0	7.0
	RA - 276.398 keV	274.22	7.164	4.6	2.4
	RA - 302.853 keV	300.04	18.33	3.6	1.9
	RA - 356.017 keV	351.37	62.05	2.2	1.7
^{137}Cs	BS - 182.38 keV[2]	8.01	94	14.2	9.3
	RA - 661.5 keV	8.01	94	0.4	1.9
^{232}Th	RA - 238.63 keV[3]	236.17 keV	47.6	6.7	3.3
	PP - 510.77 keV[4]	510.77	9.7	11.9	7.8
	RA - 583.19 keV	583.19	30.6	9.4	6.0
	RA - 911.21 keV	911.21	26.6	3.5	6.0
	RA - 968.97 keV	968.97	16.2	3.1	6.0
	PP - 1558.53 keV	968.97	35.8	4.6	1.6
	RA - 2614 keV	968.97	35.8	0.5	(0.8)

Table A.1: The energy, branching ratio, detection efficiency and energy resolution for the peaks in the spectra measured for this thesis.

B Software and Code

In this Appendix, we would like to give a short assistance on the software tools (single_cluster, fit_spectra, fit_pw, calib_pw, clustering, α-identification and muon identification) that we developed for the data analysis. All tools use libraries of the ROOT package and therefore this has to installed to guarantee a proper functioning.

single_cluster This tool is used to perform the single clustering for TOT data and create the global spectrum and the spectrum for each pixel. This is the necessary first step before TOT spectra can be fitted and a calibration be performed. It uses ROOT trees produced by the MedipixROOTconverter. Parameters:

- help, h - produces the help message.
- treename, f - the name of the root tree containing the matrix data. The filename has to be the tree name + ".root".
- pixelpitch, p - the pixel pitch of the detector. 1 is 55 μm, 2 is 110 μm, 4 is 220 μm and so on.
- min_t - the lowest TOT value in the histogram [Default is 0.5].
- max_t - the highest TOT value in the histogram [Default is 5000.5]. The number of bins is the difference between min_t and max_t.
- showentries, s - show the number of entries for the TOT histogram of each pixel.

The resulting file is the tree name + "_SC.root". It contains the single clustering TOT histogram for each pixel, named "histtot" + pixelnumber, and the histogram for the whole matrix, named TOT-Hist.

fit_spectra This tool is used to fit a sum of Gaussians to particular spectrum automatically and write out the results into an ASCII file for further investigations. The automatized recognition of the numbers of peaks in the spectrum and the fit quality can be controlled by parameters. Parameters:

- help, h - produces the help message.
- treename, f - the name of the root tree containing the matrix data. The filename has to be the tree name + ".root".

- histname, n - the name of the histogram containing the TOT spectrum.
- energyfile, e - the name of the file containing the information about the radioactive sources used for the calibration. It is an ASCII file where every entry has the following form: The first column is the source identification name, the second is the energy in keV, the third is the type of radiation (-XT- is fluorescence induced by X-ray radiation, -RA- is radioactive and -SF- are lines caused by secondary effects like escape peaks for instance), the fourth the number of peaks which can be fitted in the spectrum and in the fifth column parameters for the fit_pw routine can be specified.
- resultsfile, r - the name of the file where the fit results should be saved. If the file does not exist, it is created. If the file already exists, the results are added to the file. An additional file which contains the results of actual fit run is always created. It has the ending ".fit". Typically a results file has the structure as following: The first column is the source identification specified in the parameter material. The second column is the energy in keV found for the source identification name in the "energy file". If the source identification name was not found, this column is filled with 0.000. The third and fourth columns are mean of the TOT fit result and the fit error. The fifth and sixth columns are the σ of the TOT fit results and the fit error.
- material, m - the source identification name which the fit result should be sticked to. If this parameter is left blank, the third word[1] will be used as the source identification name. If this parameter is set to "a", the results for all peaks will be written out into the actual fit results file.
- peaknr, p - the number of the peak which should be written out. If this parameter is set to 0 the last peak will be used [default is 0].
- check_max, c - show the peaks that were found by the automatic routine [default is false].
- fit_res - show the results file after the fit procedure was performed .
- rms - the initial σ value of the Gaussians [default is 10].
- fitrange - defines the fit range in the following way: The actual fit range interval is [position of the lowest peak - fitrange; position of the highest peak + fitrange]. If fitrange is blank the complete histogram range is used.
- THL - defines the threshold for the automatic peak search routine to avoid artificial peaks in areas of low statistics. It the THL is between 0 and 1, the THL parameter is taken as a relative value to the highest peak. If the THL is bigger than 1, it is used as an absolute value [default is 0.25].

1 Word means, a set of characters separated by an "_".

- rebin - defines the rebinning of the TOT histogram for the automatic peak search routine. If the rebinning is to low, too many artificial peaks are found. If the rebinning is too high, peaks can be lost. It has to be adjusted properly to the particular spectrum [default is 2].
- dis - defines the distance for the automatic peak search routine in which the maximum property for every bin should be checked [default is 2]. Distance means the number of neighbours to the left and to the right of a bin.

In fact this routine can be used not only for TOT spectra but for every spectrum which is a sum of Gaussians. The images of the fit results are saved as .root, .pdf and .eps files.

fit_pw This tool is used to fit a Gaussian to a particular peak in a given spectrum for every pixel and save the results in a ROOT Tree for further investigation. It needs files (or at least the file content structure) produced by the single_cluster tool. To ensure a good fit quality, particular initial parameters for each radiation source have to be determined beforehand and saved in the energy file file. Parameters:

- help, h - produces the help message.
- treename, f - the name of the root tree containing the matrix data. The file name has to be the tree name + ".root".
- pixelrange, p - the range of pixels to be fitted. The syntax is "startpixel,stoppixel". The fit is performed from startpixel to stoppixel [default is 0,65536].
- energyfile, e - the name of the energy file. Full description see above. The fit parameter in the fifth column are cutvalue, direction, distance, rms. The cutvalue is the starting value to cut away the rest of the histogram. Direction specifies the direction (0 to the right, 1 to the left from the cutvalue). Distance defines the distance (to the left and to the right) around the maximum bin (after precutting) in which the histogram will not be cut away and fitted. rms is the initial value for σ. The quality of the automatic is highly sensitive on this parameters, so check them for a small set of pixels before running the routine for the whole matrix.
- material, m - the source identification name. Full description see above.
- showfit, f - show the fit results for every pixel [default is false].
- histname, n - the name prefix of the histograms containing the TOT spectra for every pixel [default is histtot].
- badpar, b - the threshold value of the badness parameter as defined in chapter III. Fits which have a badness parameter higher than badpar will be listed in a "..._badpixels.pdf" file [default is 0].
- printall - print the images of all fit results in a .pdf file [default is false].

As fits are often sensible on the statistics the routine uses the Fumili fit algorithm first, but switches to the log likelihood fit routine, if the fit fails too badly.

calib_pw This tool is used to fit a calibration curve for every pixel according to a given set of fitting points. It needs files (or at least the file content structure) produces by fit_pw. Parameters:

- help, h - produces the help message.
- treenames, t - the names of the root trees containing the fit data (produced by the fit_pw routine). The filename has to be the treename + ".root". The treenames have to be separated by a ",".
- materials, m - the source identification names. Full description see above. The source identification names have to be separated by a "," in the same order as the treenames.
- energyfile, e - the name of the energy file. Full description see above.
- format, f - specifies which of the materials should be used for fitting the calibration curve. f means fit, n means no fit. The letters have to in the same order as the treenames. If, for instance, the format is "ffnf", the first, second and fourth point will be used for fitting but not the third. On default all points will be used for fitting.
- showfit, s - show the fit results for every pixel [default is false].
- warnings, w - turn warnings on and off [default is false].
- badpar, b - the threshold value of the badness parameter. Full description see above.
- pixelrange - the range of pixels to be fitted. Full description see above.
- error - selects which quantity is to be used for the error bars. 1 is the fit error of the mean value, 2 is the fit value for σ [default is 1].

The routine automatically performs the corrections described in the calibration section (correction of total off points and flipping of c if it is negative).

Clustering The recursive clustering algorithm. It uses the vector class of C++.

```
1
2  /* Parameters:
3    matrix is an array where the measurement values of a frame are
       saved.
4    clusters is an array of vectors. Every cluster will be saved as
       new vector.
5    pitch is a number defining the pitch of the detector. 1 for 55
       mu, 2 for 110 mu, 4 for 220 mu and so on.
6  */
7
8  #include <vector>
9
10 void cluster(short* matrix, vector<int>*clusters, short pitch)
11 {
12   // Save the positions of the non-zero hits into a new vector.
13
14   vector <int> hitpos;
15   int matsize = 256*256;   // Usual matrix size for Timepix
       detectors. Can be adjusted to other detector types.
16
17   for(int i = 0; i < matsize;i++)
18   {
19     if(matrix[i]==0)  {   continue; }   // Skip empty matrix
         entries.
20     hitpos.push_back(i);          // Save non-zero entries into
         the vector.
21   }
22
23   int hits = hitpos.size(); // Determine the vector size.
24
25   // The recursive clustering loop
26
27   for(int i = 0; i < hits;i++)
28   {
29     if(hitpos.size() == 0)  // Stop, if the hitpos vector is
         empty.
30     {
31       break;
32     }
33
34     clusters[i].push_back(hitpos.at(0));  // Create a cluster and
         add the first entry of hitpos to it.
35     hitpos.erase(hitpos.begin());   // Remove this entry from the
         hitpos vector as it is already in use.
36
```

```
37      // Check if any entries of the cluster have neighbours which
           have to be added to the cluster.
38      for(int j = 0; j < clusters[i].size();j++)
39      {
40        // The loop to go from the left upper corner to right lower
             corner.
41        int pxnr = clusters[i].at(j);
42        for(int y = (pxnr - 256*pitch); y <= (pxnr+256*pitch); y =
             y + 256*pitch)
43        {
44          for(int x = (y - 1*pitch); x <= (y+1*pitch); x = x +
               pitch)
45          {
46            for(int k = 0; k<hitpos.size();k++) // Check if pixel x
                 is in the hitpos vector.
47            {
48              if(hitpos.at(k) == x) // If this is the case, add it
                   to the cluster and remove it from the hitpos
                   vector.
49              {
50                clusters[i].push_back(x);
51                hitpos.erase(hitpos.begin()+k);
52                break;
53              }
54            }
55          }
56        }
57      }
58    }
59
60    return;
61  }
```

α-identification The algorithm to recognize α-particles. The variables v_hits, v_hitrad and v_crossdis have to be adjusted to the actual pixel size. For the 110 μm pixel pitch detectors that we used in this work proper values for these variables were v_hits = 20, v_hitrad = 2 and v_crossdis = 2.

```
1
2  /* Parameters:
3    matrix is an array where the measurement values of a frame are
        saved.
4    clusters is an array of vectors. Every cluster will be saved as
        new vector.
5    pitch is a number defining the pitch of the detector. 1 for 55
        mu, 2 for 110 mu, 4 for 220 mu and so on.
6    cluster_nr is the cluster number which has to be tested.
7  */
8
9  #include <vector>
10
11 bool check_alpha(short* matrix, vector<int>*clusters, short
       cluster_nr, short pitch)
12 {
13   bool alpha_crit1 = false;
14   bool alpha_crit2 = false;
15   v_hits = 20;
16   v_hitrad = 2;
17   v_crossdis = 2;
18
19   for(int i = 0; i < clusters[cluster_nr].size(); i++)
20   {
21     if((clusters[cluster_nr].at(i) - 256*v_crossdis*pitch <= 0)||
          (clusters[cluster_nr].at(i) + 256*v_crossdis*pitch >=
          65536)) // Security check to avoid errors at the matrix
          edges
22     {
23       continue;
24     }
25
26     // Testing if there is any pixel with eight 1-neighbours.
27
28     if((matrix[clusters[cluster_nr].at(i)+v_crossdis*pitch]>0)&&(
          matrix[clusters[cluster_nr].at(i)-v_crossdis*pitch]>0)&&(
          matrix[clusters[cluster_nr].at(i)+256*v_crossdis*pitch]>0)
          &&(matrix[clusters[cluster_nr].at(i)+256*v_crossdis*pitch-
          v_crossdis*pitch]>0)&&(matrix[clusters[cluster_nr].at(i)+
          256*v_crossdis*pitch+v_crossdis*pitch]>0)&&(matrix[
          clusters[cluster_nr].at(i)-256*v_crossdis*pitch]>0)&&(
          matrix[clusters[cluster_nr].at(i)-256*v_crossdis*pitch+
```

```
        v_crossdis*pitch]>0)&&(matrix[clusters[cluster_nr].at(i)-
        256*v_crossdis*pitch-v_crossdis*pitch]>0))
29    {
30      alpha_crit1 = true;
31    }
32  }
33
34  // If the first criterium is fulfilled perform the second check
35
36  if(alpha_crit1)
37  {
38
39    short neighbour_counter = 0;
40    short position_maximum = 0;
41
42     // Locating the pixel with the maximum energy deposition
43    for(int i = 0; i < clusters[cluster_nr].size(); i++)
44    {
45      if(matrix[clusters[cluster_nr].at(i)] > matrix[
          position_maximum])
46      {
47        position_maximum = clusters[cluster_nr].at(i);
48      }
49    }
50
51    // The loop to go from the left upper corner to right lower
        corner and testing how much 1- or 2- neighbours there are.
52    for(int y = (position_maximum - 256*pitch*v_hitrad); y <= (
        position_maximum+256*pitch*v_hitrad); y = y + 256*pitch)
53    {
54      for(int x = (y - 1*pitch*v_hitrad); x <= (y+1*pitch*
          v_hitrad); x = x + pitch)
55      {
56        if((x < 0)||(x > 65536)) // Security check to avoid
            errors at the matrix edges
57        {
58          continue;
59        }
60
61        if(matrix[x] > 0)
62        {
63          neighbour_counter++;
64        }
65      }
66    }
67
```

```
68    // If the neighbour counter is above a particular value, the
          criterium is fulfilled.
69    // This value should be adjusted to the actual detector type in
          use.
70
71      if(al_counter > v_hits)
72      {
73        alpha_crit2 = true;
74      }
75    }
76
77    return alpha_crit2;
78  }
```

Muon-identification The algorithm to distinguish between electrons and muons according the reduced Hough-Transformation.

```
1
2  /* Parameters:
3    matrix is an array where the measurement values of a frame are
         saved.
4    clusters is an array of vectors. Every cluster will be saved as
         new vector.
5    pitch is a number defining the pitch of the detector. 1 for 55
         mu, 2 for 110 mu, 4 for 220 mu and so on.
6    cluster_nr is the cluster number which has to be tested.
7  */
8
9  #include "TH1I.h"    // A ROOT library
10 #include <vector>
11
12 bool check_muon(short* matrix, vector<int>*clusters, short
       cluster_nr, short pitch)
13 {
14   bool muon_crit = false;
15   TH1I* histhough = new TH1I("histhough","histhough",720,0.5,180.
       5);  // Create a histogram to fill with the angles.
16
17   for(int i = 0; i < clusters[cluster_nr].size();i++) //
       Calculate the angle phi for every two points of the cluster.
18   {
19     for(int j = i+1; j < clusters[cluster_nr].size();j++)
20     {
21       double phi = angle(clusters[cluster_nr].at(i),clusters[
           cluster_nr].at(j)); // The function "angle" is described
            below.
22       histhough->Fill(phi);
23     }
24   }
25
26   histhough->Rebin(8);  // Rebin the histogram
27
28   // Check how much data is within the 15 range around the
       maximum.
29
30   if(double(histhough->Integral(histhough->GetMaximumBin()-10,
       histhough->GetMaximumBin()+10))/double(histhough->GetEntries
       ())>0.8)
31   {
32     muon_crit = true;
33   }
```

```
34
35    return muon_crit;
36 }
37
38 Double_t angle(int p1, int p2)
39 {
40    Double_t x1 = p1%256; // Double_t variable type is defined
          within the framework of the ROOT library.
41    Double_t y1 = (p1-p1%256)/256;
42    Double_t x2 = p2%256;
43    Double_t y2 = (p2-p2%256)/256;
44
45    double angle = (TMath::ATan((abs(double(x1-x2)))/(abs(double(y1
          -y2)))))*360/(2*M_PI);
46
47    if(y2-y1==0)
48    { return 90;  }
49    else
50    { return angle; }
51 }
```

List of Figures

II.1 The energy scheme (a) and the Feynmann-diagram (b) for the regular beta decay. . . . 4
II.2 The Feynman diagram for the double beta decay - $2\nu\beta\beta$ (a) and the neutrinoless double beta decay - $0\nu\beta\beta$ (b). . . . 5
II.3 The energy scheme for isotopes capable of the double beta decay. . . . 7
II.4 The possible mass hierarchies for neutrinos: (A) normal hierarchy, (B) inverted hierarchy and (C) quasi-degenerate hierarchy. . . . 10
II.5 A scheme of the sum energy distribution for the two electrons in the double beta decay. The blue area corresponds to the $2\nu\beta\beta$ and the red peak is the $0\nu\beta\beta$. . . . 12
II.6 On the left hand side: The scheme of a typical track for a muon (a) and an electron (c) through the sensor layer. On the right hand side: The same sort of track detected with a Timepix detector. The color of the pixels indicates the energy deposition in keV. . . . 15
II.7 The response of a Timepix detector to an α-particle (a) and a simulated $0\nu\beta\beta$ event (b). The color of the pixels indicates the energy deposition in keV. . . . 16
II.8 (a) The Timepix detector E04W0083 with a USB-readout. (b) The structure scheme of a Timepix detector: A - the sensor layer; B - the ASIC with bump-bonds; C - the chipboard with electronics; D - the USB-readout. . 19
II.9 The detection process in a Timepix detector. . . . 20
II.10 The voltage pulse (red) after integration. The blue line is the threshold level. 21
II.11 The dependence of the pulse shape on the DAC-values "PreAmp" and "IKrum". . . . 22
II.12 The charge cloud at t_0 is drifted towards the pixelated side of the sensor. At the arrival time t_d it is broadened and a part of the charge (red) is collected in the wrong pixel. . . . 23

III.1 The basic necessary equipment used for measurements with the Timepix detector: (A) the Timepix with USB-readout, (B) bias voltage supply, (C) computer and (D) cables. . . . 26
III.2 The reason for the threshold equalization: The threshold energy vary among all pixels (a). After the threshold equalization, the threshold energy is at the same level for every pixel (b). . . . 27
III.3 Spacing 2: Only pixels 1, 3, 5, 13, 15, 17, 25, 27 and 29 are adjusted at the same time. . . . 28

III.4 The schematic setup for the THL calibration and a photography for the real setup. The distance d was 1 cm in the real setup. 29
III.5 The hits per frame distribution for a 110 μm pixel pitch Timepix. On (a) a good distribution is shown whereas on (b) the distribution is too far right and several pixels are saturated. 30
III.6 The illumination of a Timepix sensor layer. On (a) a good, centered positioning is shown whereas on (b) the positioning has to be readjusted. 31
III.7 The THL calibration window of PixelMan. 32
III.8 The measured (a) and differentiated (b) THL scan spectrum of ^{241}Am. The green curve is the fit with a Gaussian. 33
III.9 The THL calibration line for the whole matrix of the 110 μm pixel pitch Timepix E04W0083 performed with ^{241}Am. The fit function is f(x) = a·x + b, with a = 7.835 ± 0.532 $\frac{1}{keV}$ and b = 115.09 ± 23.98. 35
III.10 The experimental setup for calibration measurements with fluorescence radiation sources; the bold line is the way of the ray propagation. (a) sketch; (b) photography of the real setup. 38
III.11 The TOT spectra of (a) ^{241}Am and (b) ^{57}Co without single clustering. . . 41
III.12 During the single clustering procedure only events as shown on picture (b) are considered and such events as shown on picture (a) are sorted out. . . 42
III.13 The TOT spectrum of ^{57}Co (a) before and (b) after single clustering: (A) statistical artifact; (1) 14.41 keV peak of ^{57}Co; (2) Cd and Te photo peaks; (3) Cd and Te escape peaks; (4) 122.06 keV and 136.47 keV peaks of ^{57}Co. 43
III.14 The single clustering TOT spectrum of ^{57}Co (a) before and (b) after rebinning. 43
III.15 The TOT spectrum of ^{57}Co fitted with a sum of five Gaussians (red) and single Gaussians, each in a particular region (blue). 44
III.16 The single clustering TOT spectrum of (a) Mo and (b) Pb. 45
III.17 The energy deposition spectrum that is measured by a Timepix detector simulated using ROSI. 46
III.18 The global calibration curve. The fit function is $TOT(E) = a \cdot E + b + \frac{c}{E-t}$ with a = $1.70548 \pm 3.820 \cdot 10^{-4}$ $\frac{1}{keV}$, b = $35.0445 \pm 2.1993 \cdot 10^{-2}$ keV, c = 46.0468 ± 0.2911 keV, t = $3.8117 \pm 1.8455 \cdot 10^{-2}$ keV. 47
III.19 The reconstructed energy spectrum of ^{57}Co with the global calibration. The peak at 122.6 keV is shifted by 4.01 keV to the right (compared to the position predicted by ROSI). 48
III.20 The ^{57}Co TOT spectra for pixel number 23453 (red) and 23459 (blue). The distance between the 122.06 keV peaks is about 20 TOT clock ticks. . . . 50
III.21 The 122.06 keV peak in the ^{57}Co TOT spectrum of pixel number23543 (a) before and (b) after the cutting procedure. 50
III.22 The 122.06 keV peak in the ^{57}Co TOT spectrum of pixel number 23543 fitted. The first fit is blue. The second fit, limited to the $[\mu - 1.8 \cdot \sigma; \mu + 1.8 \cdot \sigma]$ interval, is green. 51

III.23 Blue is the distribution h(x) which is to be fitted and red the fit fuction f(x). The light blue marked space between the curves is the descriptive meaning of the L^{2W} error measurement. 52
III.24 The calibration curve for pixel number 6135 (a) before (the point at 59.54 keV is totally off) and (b) after the correction. 54
III.25 The calibration curve with bad fitting at low energies (a) before and (b) after the flipping. The yellow line is an additional fit for the linear part to obtain more reliable values for a and b. 55
III.26 The energy spectrum of ^{57}Co with the pixel-by-pixel calibration. 56
III.27 Definition of the quantity ΔS: The difference between the measured and expected position of a peak after calculating the energy spectrum with the calibration curve. 57
III.28 The determined value of $\frac{|\Delta S(E)|}{E}$ for peaks in the energy interval [6 keV; 125 keV]. The $\frac{|\Delta S(E)|}{E}$ value for the peaks at 59 keV is surprisingly high. . . . 58
III.29 The distribution of ΔS across the matrix for the 59.54 keV peak of ^{241}Am. It is relatively homogeneously distributed despite point at which Tellurium inclusions occur (orange blobs). 59
III.30 The distribution of ΔS of the ^{241}Am measurement plotted for all pixels. It is (almost) a Gaussian distribution around -1.88 keV. 59
III.31 ΔS for peaks above the calibration range and the linear correction line. The parameters of the curve c(x) = a·E + b are a = 0.0350 ± 0.0183 and b = -3.761 ± 1.064 keV. 60
III.32 The dependency of the energy resolution $\frac{\sigma}{E}(E)$ on the energy E. The fitted function is $\frac{\sigma}{E}(E) = \alpha + \frac{\beta}{(E-\gamma)^{\delta}}$ with $\alpha = 0.04084 \pm 0.00245$, $\beta = 2.101 \pm 0.245$, $\gamma = 2.2379 \pm 1.6863$ and $\delta = 1$. 62
III.33 The same spectrum of Pb fluorescence lines with a global calibration (a) and a pixel-by-pixel calibration (b). The K_α and K_β lines are distinguishable in the case of the pixel-by-pixel calibration, but not for the global calibration. 64
III.34 The energy resolution for various fluorescence peaks; (blue) with global calibration, (red) with pixel-by-pixel calibration, (brown) ROSI simulation data. 65
III.35 The dependency of the TOT spectrum of ^{57}Co on the IKrum ((a),(c),(e)) and the THL ((b),(d),(f)). 67
III.36 The dependence of the energy resolution on the IKrum (a) and the THL (b) measured with a global calibration. The boxes are ^{241}Am (blue), ^{133}Ba (red), ^{57}Co (brown) and the energy resolution limit (green). The boxes are slightly shifted against each other in the plot for a better visibility but do belong to the values given in the text. 68

III.37 The interdependency between the number of bad pixels on the matrix and the bias voltage. A power law (red) of the form N(V) = $a \cdot (V-b)^2 + c$ and an exponential function (green) of the form N(V)= $a \cdot \exp(-b \cdot V)$ are shown as possible fit functions. The parameters are a = $1.3 \cdot 10^{-3} \pm 2.67 \cdot 10^{-05} \frac{1}{V^2}$, b = 298.4 ± 4.3 V and c = 1.91 ± 0.95 (power law); a = 3.94 ± 0.11 and b = $-5.81705 \cdot 10^{-03} \pm 4.519 \cdot 10^{-05} \frac{1}{V}$ (exponential). 69
III.38 The energy resolution plotted versus the bias voltage in V for (blue) ^{241}Am (at 59.54 keV) and (red) ^{57}Co (at 122.06 keV) with a pixel-by-pixel calibration. 70

IV.1 The pixel matrix of a measured frame. The colour denotes always the energy deposition in keV. There are two α-particle (A), a muon (B) and an electron (C) on the picture. 74
IV.2 The definition of "distance" and "neighbour". The green pixels have distance of 1 to the pixel in the center; the blue pixels a distance of 2. The green pixels are 1-neighbours to the central pixel, the blue pixels 2-neighbours. 75
IV.3 A 5-cluster (a) and a 6-clusters with a 3-cluster (b). 76
IV.4 An example for the functionality of the clustering algorithm. The hachured pixels belong to the cluster after the previous step. 77
IV.5 Some examples for α-particles detected with the Timepix detector. 78
IV.6 The definition of the angle ϕ for the reduced Hough Transformation. . . . 79
IV.7 Four typical muon tracks and their reduced Hough Transformations. . . . 80
IV.8 Four typical electron tracks and their reduced Hough Transformations. . 81
IV.9 Four two electron (a,b,e,f) and four one electron tracks (c,d,g,h). Tracks (a) - (d) were measured whereas (e) - (f) were generated by simulations. Particles on (a) - (d) had an energy of about 2.3 MeV and (e)-(f) are tracks of particles with 2.8 MeV. 83
IV.10 The basic model for a neuron, consisting of the dendrits, the soma and the axons. 84
IV.11 A scheme of the experimental setup for the ^{232}Th measurement. (1) The ^{232}Th source, (2) the sensor layer, (3) the cardboard and (4) the lead wall. The distance between the source and the detector was about 40 cm. . . . 87
IV.12 The low energy, single-clustering spectrum of the ^{232}Th source. The abbreviations are the origin of the peaks: PP - fluorescence peak, EP - escape peak, RA - γ-line of a radioactive emitter. 88
IV.13 The spectrum of photo-, Compton-electrons and positrons produced in the sensor layer by the radiation of ^{232}Th. The measurement time for this spectrum was 34.3 h. The abbreviations are the origin of the peaks: RA - γ-line of a radioactive emitter, e^+ - photons from electron-positron annihilation, e^+e^- - pair production peak. 89
IV.14 The definition of the angle α in the context of the escape of the Compton electrons. 91

IV.15 The Compton electron spectrum; (a) the theoretical shape and (b) the spectrum as detected within the sensor layer of a Timepix detector (simulated using ROSI). The high edge at the end of the spectrum is cut as a lot of electrons escape from the sensor. . . . 92
IV.16 The (a) low energy and (b) the electron spectrum of the background measurement (277 hours of data). . . . 94
IV.17 Criteria 1-6 used for the event identification; (red) for the simulated and (blue) for the experimental data. Details on the criteria can be found in [29]. 95
IV.18 Criteria 7-10 used for the event identification; (red) for the simulated and (blue) for the experimental data. Details on the criteria can be found in [29]. 96
IV.19 Criterium 5 (the number of pixel hit during an event) for the initial simulation (green), the adjusted simulation (red) and the experimental data (blue). The matching improves by the adjustment. . . . 96
IV.20 The electron spectrum in the region of interest (a) before and (b) after event classification by the ANNs. . . . 98
IV.21 The electron spectrum in the region of interest (a) before and (b) after taking into account the classification errors of the ANNs. . . . 100
IV.22 ^{137}Cs - clustering spectrum. The abbreviations are the origin of the peaks: RA - γ-line of a radioactive emitter. . . . 102
IV.23 The shift of the pair production peak due to calibration errors. On (a) only events with a maximum energy deposition in one pixel below 330 keV and on (b) only events with a maximum energy deposition in one pixel above 390 keV are taken into account. . . . 103
IV.24 The energy resolution (a) and the peak position (b) of the pair production peak plot against E_{cut}. You can see clearly the trend: The peak is shifted to the right and broadened. The error bars on plot (a) are huge because the fit is done with poor statistics since many events are left out due to the energy cut. . . . 103
IV.25 The pair production peak (red) before and (blue) after applying the linear correction. By the linear correction the peak is shifted to its right position and the resolution is increased from 2.2 % to 1.6 %. . . . 104

V.1 The idea is to have a lot of sampling points and to fit always between three points to have small intervals in which the linear approximation is fulfilled better. . . . 108
V.2 The experimental setup for the calibration with a LASER (a) and the mask (b); (1) LASER, (2) optics, (3) mask and (4) detector. . . . 109
V.3 The distributions for single (blue) and double (red) electron events. If the set of parameters $\vec{\nu}$ is changed from $\vec{\nu}_1$ to $\vec{\nu}_2$, the shape of the distribution is changed and the area of the overlay between both distributions (purple) can be decreased. The idea is to find an optimal configuration $\vec{\nu}_{opt}$ to minimize the purple area. . . . 110

A.1 Cu - FL . . . 112

A.2 Mo - FL . . . 112
A.3 Ag - FL . . . 113
A.4 Sn - FL . . . 113
A.5 Ba - FL . . . 114
A.6 Gd - FL . . . 114
A.7 W - FL . . . 115
A.8 Pb - FL . . . 115
A.9 ^{241}Am . . . 116
A.10 ^{57}Co . . . 116
A.11 ^{133}Ba - low energies . . . 117
A.12 ^{133}Ba - high energies . . . 117
A.13 ^{137}Cs - clustering spectrum . . . 118
A.14 ^{232}Th - low energy, single-clustering . . . 118
A.15 ^{232}Th - low energy, electron clustering . . . 119
A.16 ^{232}Th - high energy, electron clustering . . . 119

List of Tables

II.1 A list of important isotopes capable of the double beta decay with some of a their properties. Values taken from [9], [10], [11] and [12]. 8
II.2 An overview about some recent $0\nu\beta\beta$ experiments. Information taken from [18]. 14

III.1 The threshold equalization settings and results. 29
III.2 The results of the THL calibration. 34
III.3 The DAC settings used during the measurements. 40
III.4 The fit results for the TOT spectrum of ^{57}Co. 45
III.5 The energy resolution of ^{241}Am,^{133}Ba and ^{57}Co given in % for two different DAC settings measured with a pixel-by-pixel calibration. The relative errors are about 2 %. 66

A.1 The energy, branching ratio, detection efficiency and energy resolution for the peaks in the spectra measured for this thesis. 120

Bibliography

[1] Majorana, Ettore: Symmetrische Theorie von Elektron und Positron. In: *Nuovo Cimento* 14 (1937), S. 171 ff.

[2] Klaus Bethge, Bernhard W. Gertrud Walter W. Gertrud Walter: *Kernphysik*. 3. Auflage. Springer Verlag, 2008. – ISBN 978–3–540–74566–2

[3] Schmitz, Norbert: *Neutrinophysik*. Teubner Studienbücher, 1997. – ISBN 3–519–03236–8

[4] al., Phillip B.: Observation of the two-neutrino double beta decay in Xe-136 with EXO-200. In: *arXiv* (2011), 21 August, Nr. 1108.4193v1

[5] F. Simkovic, A. F. M.I. Krivoruchenko K. M.I. Krivoruchenko: Neutrinoless double-beta decay and double-electron capture. In: *Progress in Particle and Nuclear Physics* 66 (2011), S. 466–451

[6] Alberto Escuderos, Vadim Rodin Fedor S. Amand Faessler F. Amand Faessler: Contributions of different neutron pairs in differnt approaches for neutrinoless double beta decay. In: *arXiv* (2010), 7 June, Nr. 1001.3519v2

[7] Hans Volker Klapdor-Kleingrothaus, Kai Z.: *Teilchenastrophysik*. Teubner Studienbücher, 1997. – ISBN 3–519–03094–2

[8] Klapdor-Kleingrothaus, H.V.: First Evidence for Lepton Number Violation and of the Majorana Character of Neutrinos. In: *Nuclear Physics B - Proceedings Supplements* 145 (2009), August, S. 219–224

[9] Group, Particle D.: *Review of Particle Physics*. Regents of the University of California, 2011

[10] *The COBRA Experiment web-page*. http://www.cobra-experiment.org/, Update 2011

[11] al., Kolo W.: EXO: the Enriched Xenon Observatory for Double Beta Decay. In: *arXiv* (2002), Nr. hep-ph/0210186v1

[12] Vladimir I. Tretyak, Yuri G. Z.: Tables of Double Beta Decay Data - an Update. In: *Atomic Data and Nuclear Data Tables* 80 (2002), S. 83–116

[13] Rabindra N. Mohapatra, Palash B. P.: *Massive Neutrinos in Physics and Astrophysics*. World Scientific Publishing Co. Pte. Ltd., 2003. – ISBN 981–238–070–1

[14] Schechter, J. ; Valle, J.W.F.: Neutrinoless double beta decay in SU(2) x U(1) theories. In: *Physical Review D* (1982)

[15] al., S. S.: The GERmanium Detector Array (GERDA) for the search of the neutrinoless double beta decay of Ge-76 at LNGS. In: *Nucl. Phys. Proc. Suppl.* 145 (2005), S. 242 – 245

[16] al., J.Diaz et: The NEXT experiment. In: *J. Phys.: Conf. Ser.* 179 (2009), Nr. 012005

[17] M. Nomachi, V. Kekelidze et a. M. Greenfield G. M. Greenfield: Nuclear Physics B - Proceedings Supplements. 138 (2005), January, S. 221–223

[18] Giuliani, Andrea: Highlights in Double Beta Decay. In: *International Student Workshop on Neutrinoless Double Beta Decay* University of Insubria, INFN, LNGS, 2010

[19] Sangiorgio, Samuele: Sensitivity of bolometric bb0v experiments. In: *NuMass 2010*, 2010

[20] X. Llopart, M. Campbell L. T. R. Ballabriga B. R. Ballabriga ; Wong, W.: Timepix, a 65k programmable pixel readout chip for arrival time, energy and/or photon counting measurements. In: *Nuclear Instruments and Methods A* 581 (2007), S. 485–494

[21] *PixelMan Software web-page*. http://aladdin.utef.cvut.cz/ofat/Others/Pixelman/Pixelman.html, Update 2011

[22] Durst, Jürgen: *Modellierung und Simulation physikalischer Eigenschaften photonenzählender Röntgenpixeldetektoren für die Bildgebung*, Erlangen Center for Astroparticle Physics (ECAP), University of Erlangen, Diss., 2011

[23] J. Jakubek, T. Holy S. Pospisil J. Uher Z. V. A. Cejnarova C. A. Cejnarova: Pixel Detectors for Imaging with Heavy Charged Particles. In: *Nuclear Instruments and Methods A* 591 (2008), S. 155–158

[24] Böhnel, Michael: *Evaluierung und Entwicklung von Röntgendetektoren für die Dosimetrie*, Erlangen Center for Astroparticle Physics (ECAP), University of Erlangen, Diss., to be published in 2012

[25] Nachtrab, Frank: *Untersuchungen zur Computertomographie und Energiegewichtung in Medipix2-Detektoren.* 2006

[26] Guni, Ewald: *Untersuchung von CdTe als Sensormaterial für die spektroskopische Röntgenbildgebung*, Erlangen Center for Astroparticle Physics (ECAP), University of Erlangen, Diss., 2011

[27] *The ROOT webpage*. http://root.cern.ch, Update 2011

[28] *Department intern software-development by Jürgen Durst.* 2009

[29] Gleixner, Thomas: *Untersuchung des Konzepts eines Experiments zur Suche nach dem neutrinolosen Doppelbetazerfall mit CdTe-Pixeldetektoren*. 2011

[30] al., PD Dr. S. L.: *Physik auf dem Computer I & II*. Uni Stuttgart, 2004

[31] Müller, Katherina: *http://www.ipp.phys.ethz.ch/education/lectures/hs07-empp/contents/km_lec1.pdf*. 2007

[32] Kishan Mehrotra, Chilukuri K. M. ; Ranka, Sanjay: *Elements of Artificial Neural Networks*. 1996. – ISBN 978–0–262–13328–9

[33] *Fast Artificial Neuronal Network Library*. http://leenissen.dk/fann/wp/, Update 2011

[34] Bouguer, Pierre: Essai d'optique, Sur la gradation de la lumière. In: *Claude Jombert* (1729), S. 164 ff.

[35] al., M.J. B.: *NIST XCOM: Photon Cross Sections Database*. http://www.nist.gov/pml/data/xcom/index.cfm, Update November 2010

[36] Klein, O. ; Nishina, Y.: Über die Streuung von Strahlung durch freie Elektronen nach der neuen relativistischen Quantenmechanik nach Dirac. In: *Zeitschrift für Physik* 52 (1929), S. 853–868

[37] *Private note from T.Gleixner*

[38] al., G.E. Schröder-Turk et: Minkowski Tensors of Anisotropic Spatial Structure. In: *arXiv* (2010), Nr. 1009.2340v1

Acknowledgments

I would like to thank the following people and institutions for supporting me and my working concerning this thesis:

- **Jürgen Durst** for bash support, the MediROOTconverter, ROOT introduction, the great hint to avoid char arrays, .. and and and .. without your help, I'd still be running after segmentation faults.
- **Michael Böhnel** and **Ewald Guni** for their help with everything concerning the experiment, listening to my complains about the calibration curve and reminding me of all the stupid mistakes I did with the handling of PixelMan and ROSI.
- **Thomas Gleixner** for a most exciting trip to Italy, being a great collaboration m8 and valuable discussion partner on all COBRA topics.
- **Thomas Weber** and **Florian Bayer** for the companionship in the glorious crusade against X-ray tubes, missing USB-readouts and other epic technical failures.
- **Wilhelm Haas** for his help with all kind of unfeasible coding problems.
- **Jutta Dziwis** for all patience with me messing up all the stuff on the blanks for the business trips; at least 10 times for each blank ..
- **Daniel Gehre**, **Stefan Taut** and **Kai Zuber** from the TUD for giving us the possibility to perform the experiments with Thorium-232. Without your help the results of this work could not be achieved at all.
- The German National Academic Foundation for the financial and mental support throughout my whole time at the university.
- My friends **Simon Mages** and **Alexander Heinz** for great entertainment and motivation during the time in Erlangen. Guys, you do be the best!
- **Sergey Ganichev** for reading all the mess of 140 pages..
- **Gisela Anton** for introducing me to the field of neutrino physics and giving me the opportunity to contribute to it.
- Last, but not at least my supervisor **Thilo Michel** !, who had to mess around with all my questions, ideas and unsatisfying results. I am very thankful for your ideas, advises and the possibilities that you offered me during the time working on my thesis.